

# Finite Element Analysis Workflow for Heat Straightening of Impact-Damaged Steel Bridges

by

Norman Fong

A thesis

presented to the University of Waterloo

in fulfillment of the

thesis requirement for the degree of

Master of Applied Science

in

Civil Engineering

Waterloo, Ontario, Canada, 2015

©Norman Fong 2015

## **AUTHOR'S DECLARATION**

I hereby declare that I am the sole author of this thesis. This is a true copy of the thesis, including any required final revisions, as accepted by my examiners.

I understand that my thesis may be made electronically available to the public.

## **Abstract**

Impacts between over-height vehicles and steel bridges are common throughout North America and the resulting bridge damage is unpredictable and sudden. Heat straightening is an alternative to replacing steel members and mechanical straightening for repairs. In many cases, bridges remediated using heat straightening require fewer disruptions to traffic and lower repair costs compared to repairs replacing steel members. Heat straightening limitations and practices have been developed with American steel grades and climates in mind. Often heat straightening is described as an art as much as a science; this repair method has relied on experienced practitioners using heat straightening patterns designed to cause rotations or shortening in members.

Heat straightening of impact-damaged steel bridges can be modelled with finite element analysis (FEA). Heat straightening is a thermo-mechanical process. Existing studies modelling heat straightening with FEA do not fully explain the modelling techniques and material parameters used. A workflow defining steps and material parameters can be used to facilitate modelling of impact and heat straightening on bridges.

This study proposes a workflow using FEA to model the heat straightening of impact-damaged steel bridges. The proposed workflow will be used to study heat straightening of CSA 350W steel – a commonly used Canadian steel grade. The workflow is developed by investigating modelling techniques for impact and heat straightening separately. The developed finite element models include material parameters accounting for work hardening, thermal effects and strain-rate sensitivity of steel.

The presented research demonstrates that the proposed workflow is viable for modelling impact and heat straightening of steel bridges. Although this study involved the application of the developed modelling techniques for a hypothetical bridge, the exercise has provided valuable insight into methods of expediting heat straightening repair and the modelling process. For instance, it has provided insight into the following: the introduction of jacking forces without causing mechanical straightening, the removal of plastically deformed stiffeners to reduce deformations, and the treatment of residual stresses from heat straightening.

## **Acknowledgements**

I would like to thank my supervisors, Dr. Robert Gracie and Dr. Scott Walbridge, for the opportunity to pursue my studies at the University of Waterloo. Their constant support and encouragement have been invaluable over the last few years.

I would also like to thank the Ministry of Transportation of Ontario for sponsoring this research into heat straightening.

## Table of Contents

AUTHOR'S DECLARATION .....	ii
Abstract.....	iii
Acknowledgements .....	iv
Table of Contents.....	v
List of Figures.....	viii
List of Tables .....	xi
List of Symbols.....	xii
1      Introduction .....	1
1.1     Background .....	1
1.2     Thesis Objectives .....	3
1.3     Thesis Outline .....	3
2      Background and Literature Review .....	5
2.1     Literature Review on Impact Damage .....	5
2.2     Heat Straightening.....	9
2.3     Case Studies of Heat Straightening.....	14
2.3.1     Brockhampton Bridge .....	15
2.3.2     Lees Avenue Overpass .....	17
2.3.3     I-10 Bridge East of Lake Charles .....	18
2.4     Existing Finite Element Models of Impact and Heat Straightening .....	21
2.5     Indicial and Tensor Notation.....	23
2.6     Continuum Mechanics of Deformable Bodies.....	24
2.6.1     Kinematics of Deformable Bodies .....	25
2.6.2     Strain .....	28
2.6.3     Stress .....	29

2.6.4	Constitutive Equations for Stress-Strain .....	32
2.6.5	Governing Equations for Mechanical Deformation .....	34
2.6.6	Constitutive Equations for Heat Transfer.....	35
2.6.7	Governing Equations for Heat Transfer .....	36
2.6.8	Temperature-Effects on Mechanical Deformation.....	36
3	Two-Dimensional Impact Modelling.....	38
3.1	Tee and Wide Flange Models .....	38
3.2	Results .....	41
3.2.1	Mesh Convergence Study.....	42
3.2.2	Plate Girder Results.....	44
3.2.3	Tee Section Results .....	49
3.3	Modelling Impact Summary .....	52
4	Modelling Vee Heat Straightening of Plates.....	53
4.1	Modelling Techniques for Heat Straightening.....	53
4.2	Material Properties for Thermal and Mechanical Analysis .....	55
4.2.1	Thermal Material Parameters .....	55
4.2.2	Mechanical Parameters.....	56
4.3	Simultaneous and Sequential Coupled Thermal-Stress Analysis for Heat Straightening .....	58
4.4	Validation of the Heat Straightening Model .....	59
4.5	Heat Straightening Model with Different Boundary Conditions .....	63
4.6	Multiple Cycles of Heat Straightening for Cantilever Plates.....	65
4.7	Modelling Heat Straightening Summary .....	67
5	Application of Models to a Full-Scale Bridge .....	69
5.1	Finite Element Analysis Workflow from Impact to Heat Straightening .....	69

5.1.1	Impact Modelling .....	70
5.1.2	Heat Straightening Modelling .....	71
5.2	Impact and Heat Straightening of bridge .....	72
5.2.1	Bridge Model.....	72
5.2.2	Impact and Heat Straightening Results .....	75
5.3	Impact and Heat Straightening Bridge Modelling Discussion.....	79
6	Conclusions .....	81
6.1	Impact Modelling .....	81
6.2	Heat Straightening Modelling .....	82
6.3	Implementing Impact and Heat Straightening Methods into Full-Scale Models.....	83
7	Recommendations .....	84
7.1	Recommendations for Future Research .....	84
7.2	Recommendations for Industry .....	84
	References .....	86
	Appendix A: News search from July 2014 to March 2015 .....	89

## List of Figures

Figure 1-1: Lee's Avenue Overpass heat straightening repairs [Ministry of Transportation of Ontario, 2012].....	2
Figure 2-1: Offset measurements to calculate degree of damage [Mukai & Avent, 1998].....	6
Figure 2-2: Plastic shortening of bar from heating [Mukai & Avent, 1998].....	10
Figure 2-3: Stages of movement from vee heating [Mukai & Avent, 1998].....	11
Figure 2-4: Time-dependent deflections of typical vee heated specimens [Roeder, 1986].....	12
Figure 2-5: Impact damage on Beam 1 (a) and Beam 5 (b) [Clubley, et al., 2006] .....	16
Figure 2-6: Photos of the damaged, then repaired girder on the Lees Avenue Overpass in Ottawa [Ministry of Transportation of Ontario, 2012]. .....	18
Figure 2-7: Fascia girder dimensions and strain ratios [Avent & Mukai, 2001].....	20
Figure 2-8: Sequence of heating cycles to straighten fascia girder [Avent & Mukai, 2001]. ...	21
Figure 2-9: Deformation of a continuous body [Belytschko, et al., 2000].....	25
Figure 2-10: Elastic and plastic decomposition of the deformation gradient on an element. ...	26
Figure 2-11: Nine components of stress at a point in a continuous body.....	30
Figure 2-12: Stress vector acting on an arbitrary plane.....	30
Figure 2-13: Stress-strain curve for a typical metal with effective stress and strain.....	32
Figure 2-14: Sources of heat transfer for a deformable body.....	35
Figure 3-1: Boundary conditions and dimensions for plate girder and tee sections.....	39
Figure 3-2: Flow stress versus effective plastic true strain of CSA 350w [Arasaratnam, et al., 2011].....	40
Figure 3-3: Paths for results after impact for plate girder and tee section.....	42
Figure 3-4: Residual bending stress distributions along Path 2 discretized with different numbers of elements for a plate girder.....	43

Figure 3-5: Residual bending stress distributions along Path 2 discretized with different numbers of elements for a tee section .....	44
Figure 3-6: Final displacement along Path 1 for quasi-static and dynamic load cases. ....	45
Figure 3-7: Vertical plastic strain along Path 1 for 15mm, 20g-25, and 40g-17 experiments. .	46
Figure 3-8: Vertical plastic strain along Path 2 for 15mm, 20g-25, and 40g-17.....	47
Figure 3-9: Residual bending stress along Path 1 for 15mm, 20g-25, and 40g-17 experiments. ....	48
Figure 3-10: Residual bending stress along Path 2 for 15mm, 20g-25, and 40g-17. ....	48
Figure 3-11: Displacement along Path 1 for quasi-static and dynamic simulations for tee. ....	49
Figure 3-12: Vertical plastic strain along Path 1 on a tee for 30mm, 40g-17, and 20g-25. ....	50
Figure 3-13: Residual bending stress along Path 1 on a tee for 30mm, 40g-17, and 20g-25....	51
Figure 3-14: Residual bending stress along Path 2 on a tee for 30mm, 40g-17, and 20g-25....	51
Figure 4-1: Comparing heat sequence from a meandering torch with the simplified heating sequence of the divided vee patterns. ....	54
Figure 4-2: Flow stress and modulus of elasticity reduction factors relative to temperature [European Committee for Standardisation, 2005]. ....	57
Figure 4-3: Flow stress versus effective plastic true strain of CSA 350w [Arasaratnam, et al., 2011] and ASTM A36 steel [Brokenbrough & Johnson, 1994].....	57
Figure 4-4: Von Mises stress distribution after simultaneous and sequential thermal-stress analysis. ....	59
Figure 4-5: Tested support conditions for 6x100mm wide plates during heat straightening [Avent, et al., 2000]. ....	60
Figure 4-6: Maximum heating temperature, residual Von Mises stresses, and maximum principal plastic strains for 3 and 9 heated regions.....	62
Figure 4-7: Plastic rotation versus maximum heating temperature for simply-supported plate. ....	63

Figure 4-8: Jacking load, P, locations for simply supported and fixed 6 x 100 x 610 mm long plates.....	64
Figure 4-9: Displacements versus time for fixed-ends and simply-supported plates with different jacking forces.....	65
Figure 4-10: Cantilever plate subjected to seven overlapping vee heats and 5 kN force.....	65
Figure 4-11: Displacements after each heat cycle for a cantilevered A36 plate. ....	66
Figure 4-12: Von Mises residual stress (MPa) and maximum principal plastic strain after heat cambering of cantilever plate. ....	67
Figure 5-1: Workflow for finite element modelling of impact and heat straightening for a structure. ....	70
Figure 5-2: Cross-section of bridge. ....	73
Figure 5-3: Bridge elevation (dimensions in millimetres).....	73
Figure 5-4: Deformations on plate girder and longitudinal plastic strains and longitudinal stress on the bottom flange after impact.....	74
Figure 5-5: Deformations after removal of selected stiffeners and lateral bracing members. ..	76
Figure 5-6: Lateral displacement after each vee heating and cooling cycles. ....	77
Figure 5-7: Longitudinal plastic strains and residual longitudinal stress distributions on bottom flange of heat straightened girder. ....	78
Figure 5-8: Longitudinal plastic strains and longitudinal stress on bottom flange during heat straightening measured in the middle vee pattern. ....	79

## List of Tables

Table 2-1: Heat straightening and beam replacement estimated cost comparison for various bridges [Ministry of Transportation of Ontario, 2012; Clubley, et al., 2006; Avent & Mukai, 2001].....	14
Table 2-2: Examples of tensor operations written with indicial and tensor notation. ....	24
Table 3-1: General material properties of steel. .....	40
Table 4-1: Functions for thermal material properties [European Committee for Standardisation, 2005].....	55
Table 4-2: Convection coefficients and heating times for each region. ....	61
Table 5-1: Forced convection coefficients for bottom flange Vee heat pattern. ....	75

## List of Symbols

$C^a$	Specific heat of material
$\mathbf{C}^e$	Elastic stiffness tensor
$\mathbf{C}^{ep}$	Elasto-plastic tangent modulus tensor
$\mathbf{D}$	Rate of deformation tensor
$\mathbf{e}$	Unit vectors in a coordinate system
$E$	Modulus of elasticity
$\mathbf{E}$	Green-Lagrange strain tensor
$\bar{\mathbf{E}}$	Effective strain
$\dot{\bar{\mathbf{E}}}$	Effective strain rate
$\mathbf{f}$	Body force
$\mathbf{F}$	Deformation gradient tensor
$F_y$	Yield strength
$h$	Convection coefficient
$k$	Thermal conductivity
$\mathbf{I}$	Identity tensor
$\mathbf{L}$	Velocity gradient tensor
$l$	Length
$L_n$	Distance between offset measurements
$M_j$	Jacking moment
$M_P$	Plastic moment
$\mathbf{n}$	Normal vector
$\mathbf{P}$	Nominal stress tensor

$q^c$	Heat flux density from convection
$q^d$	Heat flux density from conduction
$q^r$	Heat flux density from radiation
$q, r$	Cowper-Symonds parameters
$R$	Radius of curvature
$S$	2 <sup>nd</sup> Piola-Kirchhoff stress tensor
$t$	Stress vector
$t$	Time
$T$	Material temperature
$T^A$	Ambient air temperature
$T^E$	Environmental temperature
$T^S$	Surface temperature
$u$	Displacement of material point
$v$	Velocity of material point
$w$	Material spin tensor
$x$	Position vector of a material point in an deformed continuous body
$X$	Position vector of a material point in an undeformed continuous body
$y_{max}$	Distance from centroid to extreme fiber of steel element
$Y_n$	Offset measurement from reference line
$\alpha$	Coefficient of linear thermal expansion
$\delta$	Kronecker delta
$\epsilon$	Emissivity of steel
$\epsilon$	Infinitesimal strain tensor

$\epsilon_y$	Yield strain
$\lambda, \mu$	Lamé constants
$\mu$	Yield strain ratio
$\phi_d$	Degree of damage
$\rho$	Material Density
$\sigma$	Cauchy stress tensor
$\sigma^{VJ}$	Jaumann objective rate of Cauchy stress
$\bar{\sigma}$	Effective stress
$\sigma$	Stefan-Boltzmann constant
$\tau$	1 <sup>st</sup> Piola-Kirchhoff stress
$\Omega$	Domain in a continuous body

# **1 Introduction**

## **1.1 Background**

Impacts between over-height vehicles and bridges can cause local plastic deformation. Heat straightening is a method of inducing plastic deformations to undo deformations caused by impact. The basic principle is to strategically heat areas of steel to induce compressive stresses and soften it enough to cause plastic shortening after the steel returns to ambient temperature. Deformations from the original impact loading can be substantially reduced using multiple sequences of heating. These cambering techniques require applications of heating cycles in conjunction with external restraining forces resulting in gradual changes in geometry.

Heat straightening originated from techniques used by steel workers to camber steel beams [Roeder, 1986], and has been used to repair steel bridge members subjected to impacts. Heat straightening compared to other methods of repairing impact damaged structures often requires lower repair costs, which result in reduced disruption to traffic [Transportation Research Board, 1984]. The application of heat straightening on bridges is limited by the knowledge and experience of the technicians and engineers involved.

Impact damage from over-height vehicles and construction equipment represents a common problem that requires immediate assessment and remediation by engineers responsible for the maintenance of steel highway bridges. For instance, between August and December 2014 there were 41 reported worldwide incidents of over-height vehicle impacts to the undersides of bridges (see Appendix A). Unlike corrosion and fatigue, which occur gradually and can be monitored and addressed with scheduled interventions, impact damage occurs suddenly and unpredictably. In cases with significant deformations, member strengthening or replacement is commonly used to remediate bridges.

Alternatively, bridge members can be straightened using a process commonly referred to as heat straightening. Recently, the Ministry of Transportation of Ontario (MTO) has performed the first heat straightening repair in Ontario on Lee's Avenue Overpass [Ministry of Transportation of Ontario, 2012] as shown in Figure 1-1.



**Figure 1-1: Lee's Avenue Overpass heat straightening repairs  
[Ministry of Transportation of Ontario, 2012].**

Figure 1-1 shows the deformed girder and cracked bottom flange from impact and the heating process used for straightening. A detailed summary of the damage and repair process for Lee's Avenue Overpass is presented in Section 2.3.2. During the Lee's Avenue Overpass repairs, issues concerning heat straightening during winter conditions caused delays [Ministry of Transportation of Ontario, 2012].

Many of the limitations and recommendations for heat straightening reported in the literature are applicable to warmer climates. The literature does not address heat straightening in colder climates such as those found in Canadian winters in Ontario. Finite element analysis (FEA) can be used to model the structural response of bridges subjected to impact and heat straightening repair for different steel grades [Kowalkowski, 2005]. These simulations require material parameters covering strain-rate and thermal effects associated with impact and heat straightening, respectively.

In the current study, small-scale FEA simulations are used to study the limitations and validity of the impact and heat straightening modelling process separately. These modelling techniques are applied on a steel bridge to model impact and heat straightening.

The following two sections in this introduction summarize the objectives of thesis and provide a brief description of the contents of each chapter.

## **1.2 Thesis Objectives**

The goal of this research is to develop a clear workflow to identify material parameters for FEA and expedite the modelling of steel bridge impact and heat straightening. Specifically, this thesis aims to accomplish the following objectives:

- to compare different methods of modelling impact in FEA,
- to compare and validate different methods for modelling heat straightening in FEA by comparing analysis results with experimental results from the literature,
- to develop a workflow for finite element modelling of impact and heat straightening, and
- to apply the workflow to a full-scale steel highway bridge.

## **1.3 Thesis Outline**

This thesis is composed of seven chapters: Introduction (the current chapter), Background and Literature Review, Two-Dimensional Impact Modelling, Plate Vee Heat Straightening, Heat straightening Impact-Damaged Bridges, Conclusion, and Recommendations.

The literature review section discusses impact damage, heat straightening, and the governing equations used to model impact and heat straightening in FEA. This section begins with an overview of how impact damage is evaluated prior to heat straightening and the limitations for heat straightening based on damage. The heat straightening sub-section contains a brief history of heat straightening, changes in material properties after heat straightening, and limitations of heat straightening. A case study section is used to provide examples of where heat straightening is used as an alternative to member replacement. In addition, limitations to existing finite element models of impact and heat straightening are also discussed in this section. Moreover, a brief section on indicial and tensor notation is included to review concepts used to describe continuum mechanics. The literature review concludes with a brief discussion of the governing principles of continuum mechanics for deformable bodies and heat transfer approximated by FEA.

Differences between quasi-static and dynamic methods of modelling of impact are investigated in Chapter 3. These differences are evaluated for two-dimensional finite element models with similar deformed shapes by assessing residual stress and plastic strain distributions.

Chapter 3 concludes with a summary comparing quasi-static and dynamic methods of modelling impact.

Chapter 4 describes the techniques used for modelling heat straightening in comparisons to existing experimental data from the literature. This chapter also includes thermal material properties and assumed parameters used to model heat transfer associated with heat straightening. The first section includes a discussion of two modelling methods: sequential and simultaneous thermo-mechanical modelling. This chapter discusses the employed finite element model that uses a simplified method for modelling the heating process associated with heat straightening with oxyacetylene torches. This simplified method is validated using existing experimental data for plates bent by vee heating. The validation is followed by a study demonstrating the effects of jacking forces and boundary conditions on the effectiveness of heat straightening.

In the fifth chapter, modelling techniques developed in Chapters 3 and 4 are used to model a full-scale bridge subjected to impact followed by heat straightening repairs. This chapter begins with a detailed description of the workflow used to model the impact and heat straightening. The workflow description is followed by a description of the bridge model, including simplifications and assumptions used to expedite the modelling process. Following the bridge description, residual stress, strain, and the number of heat cycles are presented. This chapter concludes with a discussion of the results.

The final two chapters summarize the important outcomes of this research and present recommendations for future research and suggested changes to current industry practice.

## **2 Background and Literature Review**

The background and literature review presented in this chapter will summarize research on impact damage and heat straightening for steel bridges. In particular, this section presents:

- a review of impacts on bridges introducing a method of assessing impact damage on steel bridges,
- an overview of heat straightening including a brief history and detailed review of current research associated with heat straightening,
- a summary of case studies of heat straightening on bridges highlighting the costs and procedures associated with heat straightening,
- a summary of existing finite element analysis (FEA) models for heat straightening identifying limitations in the existing modelling process,
- an introduction to indicial notation clarifying the notation used in the discussion of continuum mechanics and governing equations, and
- a review of continuum mechanics and the constitutive equations governing the physics approximated in FEA.

The detailed review of previous research associated with heat straightening includes heat straightening effects on the material properties of American and European steel grades. This research is also evaluated to highlight recommendations and conclusions important for colder Canadian climates during winters.

### **2.1 Literature Review on Impact Damage**

Collisions between bridges and over-height vehicles are surprisingly common [Transportation Research Board, 1984]. At the minimum, road closures are often required as engineers assess the damage from impact. In more severe cases, bridge damage can lead to considerable costs to owners and users of the transportation network, if road closures and significant emergency repairs are required. If it is made of steel, the structure must be inspected for tearing or cracking caused by the impact. Changes in geometry are noted and calculations

are performed to determine the degree of damage and evaluate potential fatigue problems that may occur due to resulting stress concentrations.

Prior to heat straightening, impact damage must be documented by classifying the type of damage and magnitude. Damage that can be heat straightened is classified under four categories of deformation [Mukai & Avent, 1998]: strong axis, weak axis, local, and twisting. These damage categories are used to determine the heat straightening repair techniques required. Strong axis damage refers to deformations along the axes, where the section modulus is highest. Weak axis damage refers to deformations along the axes perpendicular to the strong axis. Whereas local damage refers to bulges in the web or the flange spanning short distances. Twisting damage refers to the torsional rotation of a steel section. Damage that cannot be repaired by heat straightening includes: indentations, dents, holes, and cracks. The magnitude of damage is quantified in terms of the degree of damage ( $\phi_d$ ) or strain ratio ( $\mu$ ). Figure 2-1 shows the offset measurements required to determine the degree of damage on a bent plate.

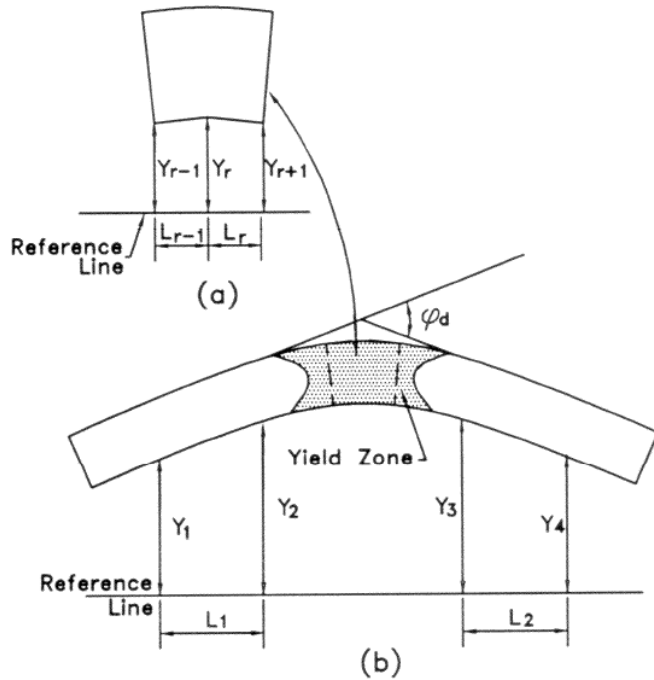


**Figure 2-1: Offset measurements to calculate degree of damage [Mukai & Avent, 1998].**

The degree of damage is the change in angle in a bent steel member. The measurements shown in Figure 2-1 are used to calculate the degree of damage from the impact, as follows:

$$\phi_d = \tan^{-1} \left( \frac{Y_2 - Y_1}{L_1} \right) + \tan^{-1} \left( \frac{Y_3 - Y_4}{L_2} \right) \quad (1)$$

where  $Y_n$  is the measured distance from the reference line to the face of the damaged steel member,  $L_n$  is the distance between two  $Y_n$  measurements, and subscript  $n$  refers to the number of measurements ( $n = 1,2,3,4$ ). The degree of damage is related to the radius of curvature,  $R$ :

$$\sin \left( \frac{\phi_d}{2} \right) = \frac{L}{R} \quad (2)$$

The radius of curvature is approximated to the centroid of the steel element and is used to estimate the strain ratio.

The strain ratio is defined as the measured strain of the steel at the extreme fibre as a multiple of the yield strain ( $\epsilon_y$ ) of the damaged steel member. The strain ratio is calculated as:

$$\mu = \frac{E y_{max}}{R F_y} \quad (3)$$

where  $E$  is the modulus of elasticity,  $y_{max}$  is the distance from the centroid to the extreme fibre of the steel element,  $R$  is the radius of curvature determined using Equation (2), and  $F_y$  is the engineering yield strength of steel. The strain ratio is used to determine if the damaged steel members are candidates for retrofitting by heat straightening. The strain ratios have been correlated with material tests for yield strength and fracture resistance.

The recommended strain ratio limit of 100 times the yield strain ( $100 \cdot \epsilon_y$ ) is suggested in [Mukai & Avent, 1998]. Heat straightening repairs occurring below this strain ratio had material properties that are not significantly affected by strain hardening from impact. Strain ratios from impact damage above  $100 \cdot \epsilon_y$  were not investigated in 1998, suggesting that recommended strain ratio limit greater than  $100 \cdot \epsilon_y$  is possible. More recent research suggests that the strain ratio limits can be higher. Strain ratio limitations required that heat straightening repairs should not cause stresses exceeding 50% of the yield strength of steel.

At the elevated temperatures associated with heat straightening, the yield strength of steel can be reduced by 50% relative to the yield strength at room temperature. Stresses exceeding 50% of the yield strength of steel could cause mechanical straightening. The main sources of stress during heat straightening are stresses from thermal expansion, residual stresses from

impact damage, and stresses from jacking forces which restrain movement. Jacking forces are used to restrain thermal expansion by rotation or elongation. Jacking forces are used to expedite the heat straightening repair process.

Recent research by [Sharma, 2005] and [Liu, 2006] investigated higher strain ratio limits with stresses at 50% and exceeding 50% yield strength. The Charpy V-notch tests indicated that the ductile-brittle transition temperature of A36 steel is significantly affected by higher strain ratios and jacking forces. Their research suggested that damage along the weak axis for A36 steel plates should not exceed a  $200 \cdot \epsilon_y$  strain ratio limit at higher service temperatures and a  $65 \cdot \epsilon_y$  strain ratio limit at lower service temperatures. A36 steel plates with strong-axis damage should not exceed the  $100 \cdot \epsilon_y$  strain ratio limit. Steel plates exceeding these strain ratios had reduced fracture resistances at low service temperatures. Damaged steels exceeding strain ratio of  $65 \cdot \epsilon_y$  had ductile-brittle transition temperatures higher than  $-18^\circ\text{C}$  for steel samples. Also, damaged steel plates repaired using jacking forces causing stresses exceeding 50% yield strength had significantly higher ductile-brittle transition temperatures.

A report on the effects of heat straightening was prepared by R.J. Connor, M.J. Urban, and E.J. Kaufmann for the National Cooperative Highway Research Program [Connor, et al., 2008]. This report focused on the effects of impact damage and heat straightening on the fracture and fatigue behaviour of steel bridge girders. The summarized research consists primarily of laboratory investigations of impact damaged and heat straightened specimens, although the finite element method (FEM) is used to investigate the elastic stress concentrations due to the sudden change in geometry in the vicinity of the impact damage. The key findings of this research can be summarized as follows:

- No fatigue problems are encountered in impact damaged/heat straightened welds if post-weld treatments (such as grinding) are applied after heat straightening.
- Grinding impact damaged and heat straightened plate surfaces is also recommended to remove the brittle cold worked surface layer and any micro-cracking occurring in this region.
- Due to the local stress concentration (SCF), stresses from the external (jacking) restraints can be as much as 50% higher than the corresponding nominal stresses. It is recommended

that restraint forces be reduced to compensate for this to prevent cracking during heat straightening.

- A method for predicting the SCF due to any residual deformation remaining after the heat straightening process is proposed, to ensure that fatigue is not a concern.
- It is recommended to limit impact/repair cycles to two if successive impacts occur within 300 mm of each other, in order to ensure that the material properties of the steel remain satisfactory.
- It is recommended that the strain limit in [Mukai & Avent, 1998] be increased to 150 times yield strain, based on more recent research including data for up to 230 times the yield strain.
- It is recommended that further work be performed to improve the fatigue assessment procedures for damaged or partially straightened impact regions.

The strain ratio limit suggested in this report is significantly higher than the limits suggested in [Sharma, 2005] and [Liu, 2006]. The simulated impact damage in [Sharma, 2005; Liu, 2006] is imposed statically, in contrast to [Connor, et al., 2008], wherein a custom “drop tower” is used to damage the specimens dynamically.

Steel is a strain-rate sensitive material; the yield strength of steel increases in relation to the strain-rate, as described by Cooper-Symonds relationship [Fire and Blast Information Group, 2001]. The speed at which the impact load is applied is not considered in these experiments. However, this is an important factor in determining how the steel responds to impact. As a result, the difference in the strain limits recommended in [Liu, 2006] is significantly lower than the strain limits recommended in [Connor, et al., 2008].

## 2.2 Heat Straightening

Heat straightening originated from techniques used by steel workers to camber steel beams. The use of heat straightening had been limited to experienced practitioners. The earliest academic record of heat straightening is provided in 1938 by Joseph Holt [Avent, et al., 2000]. A number of issues with heat straightening and changes in material properties remain unaddressed, as evidenced by a number of research projects carried out on the subject in the last

two decades, in particular in the United States [Mukai & Avent, 1998]. This lack of knowledge is the reason why heat straightening was not an accepted repair method throughout most of the states until the late 1990s. A comprehensive guide for heat straightening was written for the US Federal Highway Administration (FHWA) in 1998 [Mukai & Avent, 1998]. This guide to heat straightening outlined effects, limitations and methods of heat straightening on damaged bridge steel allowing many states to add heat straightening as a valid method of repair.

Heat straightening requires heating steel in specific patterns in conjunction with external restraining forces. Oxyacetylene torches are used to heat patterns in the steel. The elevated temperatures are sufficient to reduce the yield strength and create thermal expansion in the steel. Temperatures must not exceed the temperature required to cause molecular transformations. 650°C and 590°C are the maximum recommended heating temperatures for A36 steel and quenched/tempered steels, respectively [Mukai & Avent, 1998].

Heat straightening is caused by a sequence of heating which causes local deformation by plastic shortening. Consider a steel bar restrained from longitudinal thermal expansion as shown in Figure 2-2.

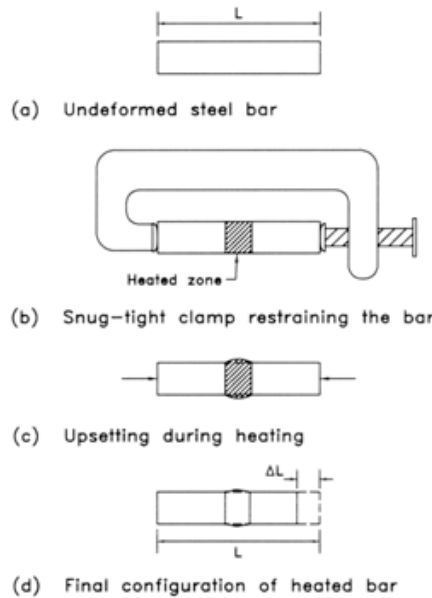


**Figure 2-2: Plastic shortening of bar from heating [Mukai & Avent, 1998].**

At elevated temperatures, the combination of the reduced yield strength and confined thermal expansion causes the steel to expand in unconstrained directions, shown in Figure 2-2(c). The

deformed volume of heated steel contracts from cooling causing plastic shortening, shown in Figure 2-2(d).

Vee heat straightening can be considered as heat shortening a set of bars or strips with increasing length [Nicholls & Weerth, 1972]. Plastic shortening increases proportionally with the length of the heated steel. Figure 2-3 shows the plate movement on a deformed plate from vee heating. The triangular or vee pattern is typically heated from the tip to the base in a meandering motion, shown in Figure 2-3. Heating the pattern from the tip in this meandering motion is the most efficient method of heating the entire area [Mukai & Avent, 1998] and increasing plastic rotation [Transportation Research Board, 1984]. The heated apex of the vee begins to cool before the base is completely heated causing additional compressive restraining forces at the base and deflection, shown in Figure 2-3(b). The additional compressive restraining forces increase plastic shortening at the base causing plastic rotation that decreases deflection, shown in Figure 2-3(c).

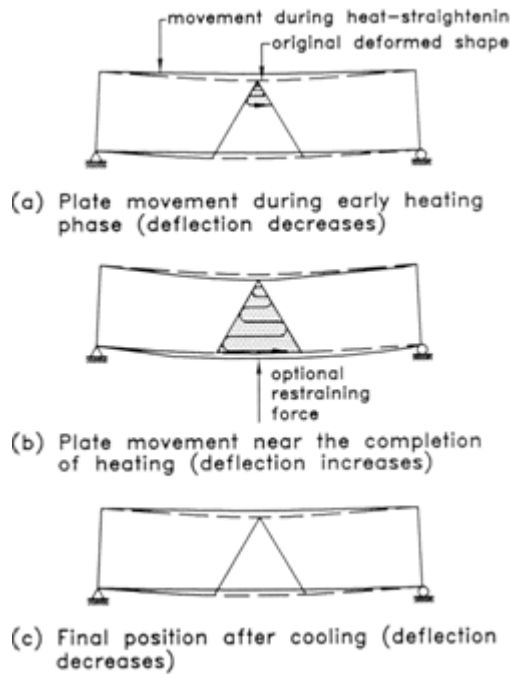


**Figure 2-3: Stages of movement from vee heating [Mukai & Avent, 1998].**

The expected plastic rotation from a vee heated plate is around 0.5 to 13 milliradians depending on vee angle, depth, restraining forces, and heating temperature [Avent, et al., 2000]. Changes from vee heating are usually measured in terms of milliradians, rather than

displacement, to eliminate length as a parameter. Often multiple cycles of heating is required to substantially reduce deformations. Figure 2-4 shows the deflections of a typical wide flange specimen as it is vee heated and cooled. The shape of time-dependent deflections, shown in Figure 2-4, is similar to the deflections of a vee heated plate.

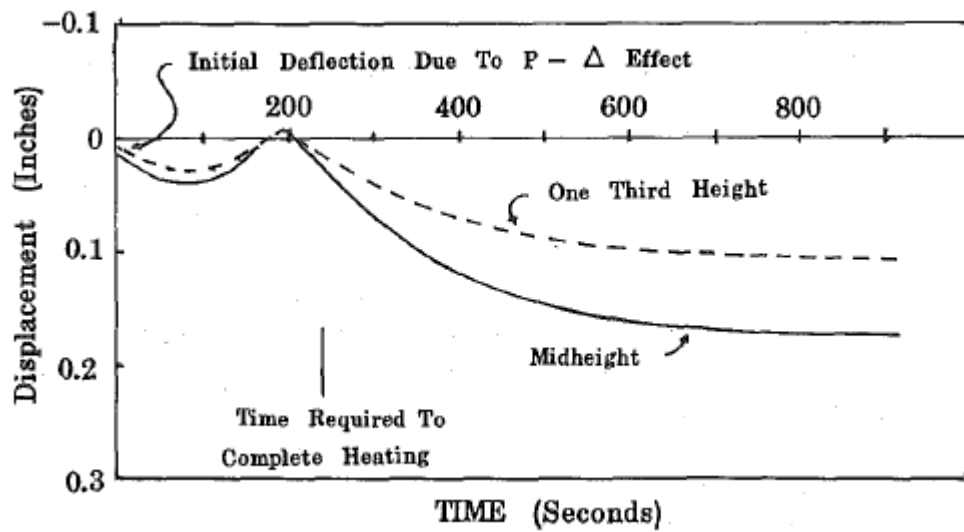


**Figure 2-4: Time-dependent deflections of typical vee heated specimens [Roeder, 1986].**

During heating, the desired displacement decreases then the largest beneficial changes in displacement occur after heating is completed. The measured longitudinal strain from a typical heat cambered wide flange specimen was upto 0.01 [Roeder, 1986]. Stress distributions from heat cambering/straightening was studied by Nicholls & Weerth.

Stress distributions from vee heat straightening is studied in [Nicholls & Weerth, 1972]. This research focussed on studying the residual stress and cambers created by different depth and angle vee heats. 152 mm (6") wide and 9.5 mm (3/8") thick A36 plates were heated to 650 °C and subjected to 2.2 kN (490 lbs) of preloading 1016 mm (40") from the heated section. Theoretical analysis was performed assuming that the steel was perfectly elasto-plastic and lateral strains were insignificant. The theoretical camber from analysis was reasonably close to experimental results. Untreated and heated A36 plates are divided into eight strips of specimens, where the residual stresses were measured. Plates subjected to heat cambering had residual compressive stress at the tips of the vee heats. The procedure of dividing the plates into strips was the basis for the concept of modelling the heat transfer from the motion of torches as sequential heating of strips.

Mukai and Avent [1998] suggest that the combination of external jacking forces, residual stresses, and thermal stresses should not exceed 50% of the steel's yield strength at room temperature [Mukai & Avent, 1998]. The external jacking forces relative to the yield strength of steel is referred to as the 'jacking ratio'. The yield strength of steel is reduced up to 50% during heating. Research with heat straightened steel subjected to jacking ratios exceeding 50% shows that the steel notch toughness is significantly reduced [Sharma, 2005; Liu, 2006].

In general due to work hardening, the tensile and yield strength of steel improved and the ductility of steel is reduced. The effects of heat straightening on the material properties of steel were discussed in [Mukai & Avent, 1998] and further studied in [Sharma, 2005; Liu, 2006; Kowalkowski, 2005; Lacalle, et al., 2013]. For undamaged plates subjected to a single heat straightening cycle, significant reductions in ductility (10-25%) are noted. Damaged plates subjected to multiple heat straightening cycles have significant increases in yield stress as high as 20%. The resulting ductility of the heat straightened steel was reduced approximately 30% compared to undamaged steel. However, heat straightening may cause reductions in yield strength, as shown in [Lacalle, et al., 2013] for European steel grades.

The material properties of European steel grades S235 JR, S460 ML, and S690 QL subjected to heat straightening are investigated in [Lacalle, et al., 2013]. The S460 ML and S690 QL are thermo-mechanical rolled and quenched steel, respectively. Both S460 ML and S690 ML steel grades have a minimum impact energy of 27 J at -50 °C whereas S235 JR had a minimum impact energy of 27 J at -20 °C. After heat straightening, the ductile-brittle transition temperature of S235 JR increases whereas for S460 ML and S690 QL the ductile-brittle transition temperature decreases. The performance of steel grades designed to withstand brittle failure at lower temperatures did not significantly worsen. Careful consideration for cooling rates in combination with the nature of steel grades must be made to prevent adverse changes in material properties. The effects of heat straightening had different results depending on the steel grades. Similar to American steel grades, the yield strength of the European steel grades after heating is not significantly reduced (up to 15%). Multiple damage-repair cycles did not have a significant effect on the yield strength of the American steel grades.

The effects of multiple impact damage and heat straightening cycles are investigated for A7, A373, A588, A36, and A572 Gr.-50 steel in [Kowalkowski, 2005]. The number of damage-

repair cycles did not significantly or predictably reduce the yield or ultimate strength of the tested steel grades. The A7 steel yield strength varied between 85-120%, for example. However, the number of damage-repair cycles significantly decreased the fracture toughness of the steel specimens. This research concluded that heat straightening should be limited to three to five damage-repair cycles depending on the steel grade.

Often the techniques and recommendations summarized in [Mukai & Avent, 1998] are used outside of the United States as a guideline for heat straightening. This guide to heat straightening was used in the United Kingdom and in Canada for [Clubley, et al., 2006] and [Ministry of Transportation of Ontario, 2012], respectively. These case studies present examples of where heat straightening was used to minimize traffic disruptions and as a cost-effective alternative to beam replacement.

### **2.3 Case Studies of Heat Straightening**

Heat straightening is a cost-effective alternative to bridge repairs using beam replacement [Transportation Research Board, 1984]. Heat straightening repairs may cost between 5% and 65% as much as a full or partial member replacement [Transportation Research Board, 1984]. Lee's Avenue Overpass, Brockhampton Bridge, and I-10 East of Lake Charles Bridge are modern case studies where heat straightening saved money compared to full or partial girder replacement. Table 2-1 shows the estimated cost of repairs for heat straightening and beam replacement for the case studies discussed above.

**Table 2-1: Heat straightening and beam replacement estimated cost comparison for various bridges [Ministry of Transportation of Ontario, 2012; Clubley, et al., 2006; Avent & Mukai, 2001].**

	<b>Estimated Cost of Repairs</b>		<b>Compared Costs</b>	<b>Heat Straightening Repair Time</b>
	<b>Heat Straightening</b>	<b>Beam Replacement</b>		
<b>Lee's Avenue Overpass</b>	\$850,000	\$2,500,000	34%	20 Nights
<b>Brockhampton Bridge</b>	£90,000	£360,000	25%	10 Days
<b>I-10 Bridge East of Lake Charles</b>	\$49,000	\$100,000	49%	14 Days

Heat straightening repair costs are as low as 25% as shown on the repair of Brockhampton bridge and as high as 49% as much as the costs of beam replacement with the repair of the bridge on I-10 east of Lake Charles. In all three case studies, heat straightening repair is chosen over girder replacement due to reductions in project costs and traffic disruption.

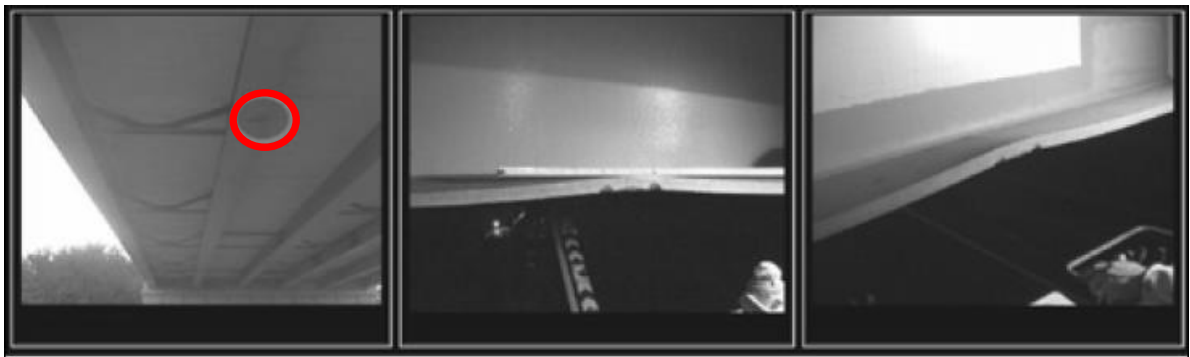
The following subsections summarize the impact damage and the repair procedure for the three case studies discussed above. These case studies present situations where heat straightening has been used in three different countries with different magnitudes of impact damage. The detailed repair procedures summarized are unique to each case study and demonstrated solutions to a range of unique problems associated with heat straightening.

### **2.3.1 Brockhampton Bridge**

The Brockhampton bridge, located in Hampshire, UK, was constructed in 2001 [Clubley, et al., 2006]. The three-span composite steel plate girder bridge was supported by six S355 steel plate girders and a 210 mm thick reinforced concrete slab. The Brockhampton Bridge was subjected to an impact from a low-bed truck. The impact was located within the 34.6 m span and 8 m from the north pier. Significant impact damage was located on the first and fifth beams and the two lateral bracing members closest to the point of impact. Figure 2-5 shows the deformed beam geometry on Beam 1 and 5 from impact.



Beam 1 (a)



Beam 5 (b)

**Figure 2-5: Impact damage on Beam 1 (a) and Beam 5 (b) [Clubley, et al., 2006].**

Beam 1 had bottom flanges bent upwards by 70 mm over 800 mm along the beam length and laterally deformed 50 mm over approximately 16 m. A large crack was discovered in the web just above the bottom flange weld. Beam 5 had bottom flanges bent upwards by 20 mm over 800 mm along the beam. The web and bottom flanges of beam 5 had no visible lateral deformations.

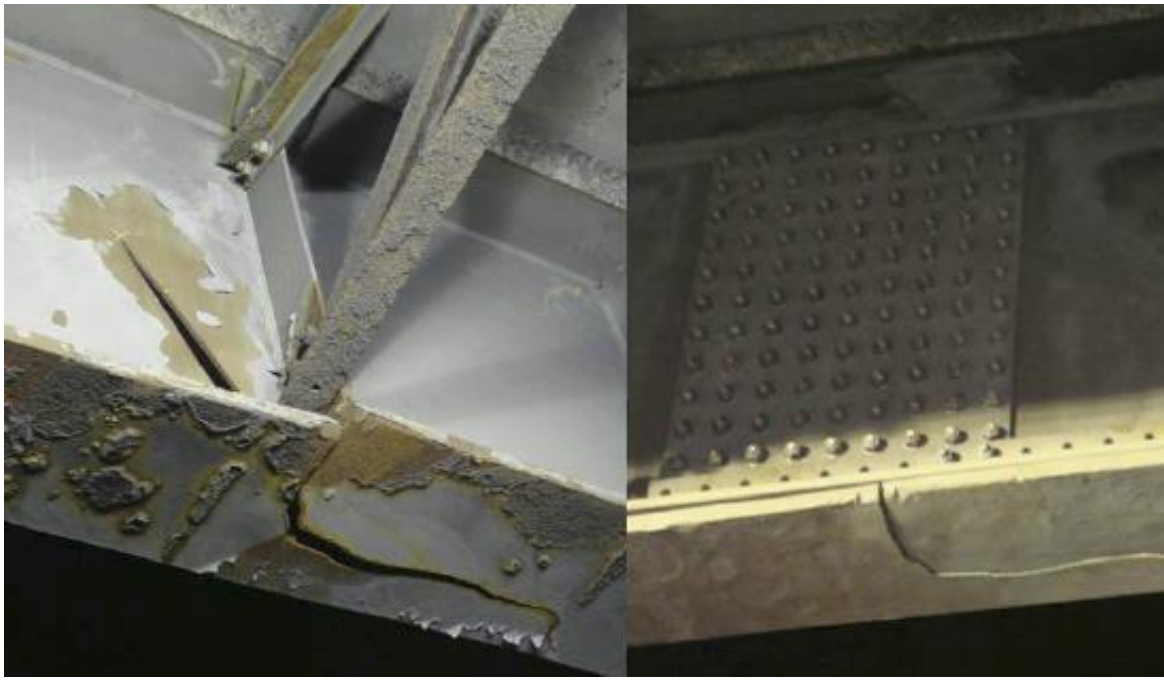
Bridge repairs required a combination of heat straightening and member replacement. Beam 1 required five heat cycles to reduce the global lateral displacement from 52 mm to 21 mm, which was within the defined repair tolerances. Local bottom flange damage was repaired to tolerance using nine heat cycles of vee and line heats. The cracked section of the web was repaired by replacing a 500x500 mm section of the web. In addition to the new web, a new vertical web stiffener was installed. Replacement lateral bracing members were attached to Beam 1 using bolts. Deformations in Beam 5 were straightened from 22 mm to 8 mm using four heating cycles with line heats.

During heat straightening repair, the bridge was restrained using hydraulic jacks to accelerate the repair process. These restraining loads did not exceed 33 kN and 67 kN for the first two heating cycles and subsequent heating cycles, respectively. The bridge steel was heated to a range of 550°C to 620°C. The steel temperature was checked with infrared digital pyrometers after the steel was heated based on observed colour changes of surrounding steel.

Material testing based on Vickers hardness tests, at the maximum heated regions, indicated that there were no significant changes in ultimate tensile strength after one heat cycle. After multiple heat cycles, the Vickers hardness results reduced from 165 to 125 HV and the ultimate tensile strength was reduced from 550 to 400 MPa. The ultimate tensile strength requirement for S355 steel for these steel beams is 490 MPa. The reduced tensile strength was located near the point of counter-flexure, where the bending moments are low, so higher tensile strength is not required.

### **2.3.2 Lees Avenue Overpass**

Lees Avenue Overpass is located over Highway 417 in Ottawa, Canada and was constructed in 1966 [Ministry of Transportation of Ontario, 2012]. The 87.9 m three-span plate-girder bridge was impacted by an over-height truck. The impact caused a 600 mm upward crack from a transverse stiffener joined a bottom flange crack almost through the flange width, as shown in Figure 2-6(a). The lateral displacement of the bottom flange was 50 mm measured on either side of the crack. Heat straightening was chosen over partial girder replacement due to the complexity, cost, and traffic disruptions associated with installing a new curved girder section. Four line and vee heating patterns were placed approximately 450 mm apart. The line heats extended 400 mm from the bottom of the web towards the top flange and 150 mm wide full-depth vee heats were used in the bottom flange. Heat straightening was used to close the cracks prior to replacing diaphragms and stiffeners, as shown in Figure 2-6(b). The repair process starting in December 2010 was delayed until April 2011 due to extremely cold weather. Cover plates were installed to reinforce the cracked web and bottom flange.



Damaged Girder (a)

Repaired Girder (b)

**Figure 2-6: Photos of the damaged, then repaired girder on the Lees Avenue Overpass in Ottawa [Ministry of Transportation of Ontario, 2012].**

### 2.3.3 I-10 Bridge East of Lake Charles

The overpass was constructed around 1965 and is located on I-10 East of Lake Charles [Avent & Mukai, 2001]. This 22.9 m (75 ft) long four span bridge with five simply-supported girders. The bridge was damaged by over-height equipment on a flatbed trailer.

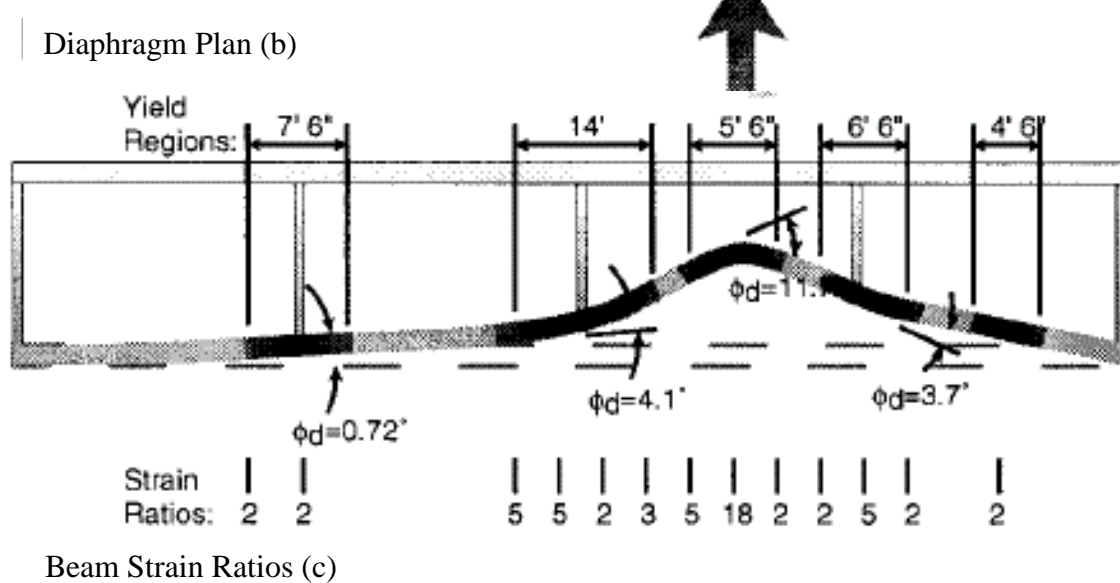
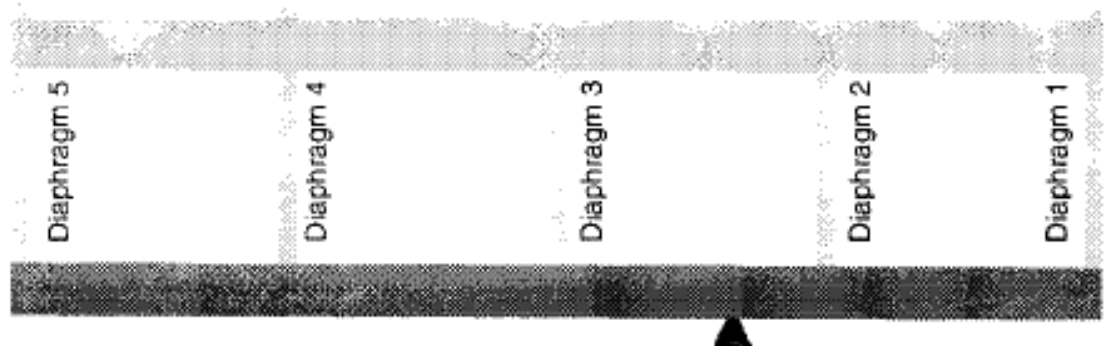
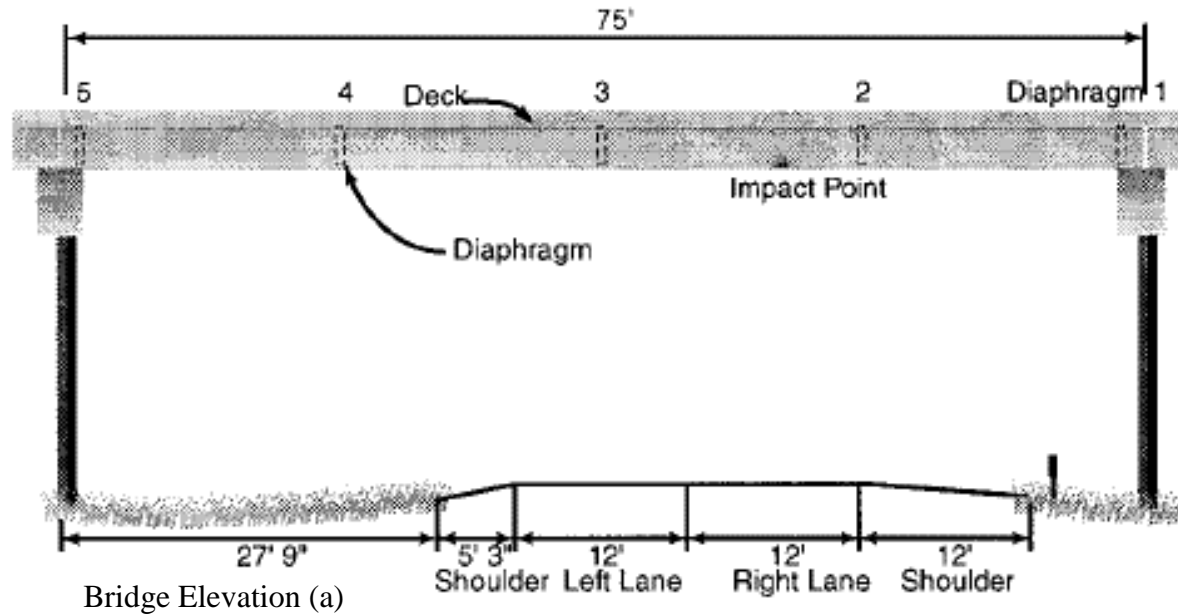
The majority of the damage was localized to the bottom flange of the fascia girder as shown in Figure 2-7. Deflections shown in Figure 2-7 were exaggerated. Five yielded regions over a range of 4.5 feet to 14 feet long with degrees of damage up to  $11.7^\circ$ . The damage from the bottom flange extended to connecting diaphragm members and sections of the web. Heat straightening focused on correcting flexural yielding of the bottom flange and web.

Due to the complex deformed shape of the bottom flange, as shown in Figure 2-7, the girders were straightened in sections. The damaged diaphragm members were removed and heat straightening operations started from locations with the highest degree of damage. 100 mm wide full-depth vee heating patterns were used for bottom flange heat straightening. Hydraulic jacks

were placed at the point of impact and at the diaphragm locations to provide restraining forces for heat straightening. In this case study, the measurements from jacking forces were compared to theoretical deformations using the moment of inertia of the girder. The girders required 1.15 times the theoretical jacking force to achieve the desired deformations. The maximum jacking forces were 181 kN, 162 kN, and 135 kN at diaphragm 2, the point of impact, and diaphragm 3, respectively.

Initial heat cycles used relatively low jacking forces; the initial jacking ratios were 11% and increased to 22% for subsequent heat cycles. After diaphragm 4 was removed the jacking ratio was increased to 44%. During heat straightening at diaphragm 3, the jacking ratio was limited to 30% from the 40 kN maximum jacking force.

Heat straightening temperatures were monitored using thermal crayons. The heating pattern temperatures were not explicitly specified in this paper. Avent and Mukai had estimated that the entire heat straightening would require 108 vee heats or 22 heat cycles assuming five simultaneous vee heats.



Beam Strain Ratios (c)

Figure 2-7: Fascia girder dimensions and strain ratios [Avent & Mukai, 2001].

The bridge required 22 heat cycles to correct the flexural yielding at the bottom flange and web. Four simultaneously heated vee patterns and two line heats were used at each cycle on the impact point, shown in Figure 2-8(a). Seven heating cycles were required at the impact point at the beginning and end of the flexural heat straightening portion of the repair, shown in Figure 2-8(b) and Figure 2-8(c). At diaphragm 3, five vee heating patterns were used at each cycle; the impact damage was located in the bottom flange only. At diaphragm 2, the same heating patterns were used with the addition of line heats to correct the web, shown in Figure 2-8(d). Additional heat straightening operations for web bulges used 3 or 4 heat cycles of line heats.

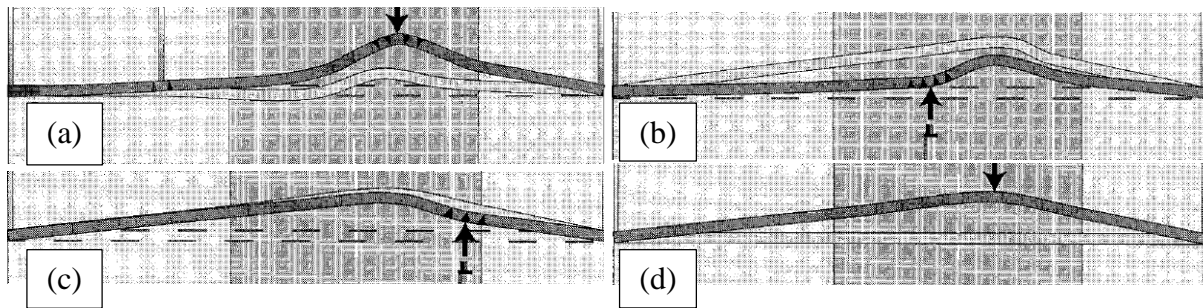


**Figure 2-8: Sequence of heating cycles to straighten fascia girder [Avent & Mukai, 2001].**

## 2.4 Existing Finite Element Models of Impact and Heat Straightening

The response of structures subjected to impact loads have been extensively modelled over the last 20 years in the automotive and defense industries with FEA [Belytschko, et al., 2000]. Similarly, it is now standard practice to use simulations to optimize metal forming operations, which are governed by the same physics as heat straightening [Kobayashi, et al., 1989]. In particular, metal forming techniques found in research on forming ship hulls with flame heating [Moshaiov & Latorre, 1985; Moshalov & Voros, 1987] can be used to model heat straightening. Heat straightening of steel girder composite bridges and steel plates have been modelled by Kowalkowski [2005]. Other notable research focused on modelling the effects of impact on steel girders with respect to potential problems in fracture [Sharma, 2005; Connor, et al., 2008].

In Moshaiov and Latorre [Moshaiov & Latorre, 1985], the temperature distribution in steel during flame cambering is studied based on various speeds of flame movement. The point source of heat flux from a torch was modelled as Gaussian distribution. The transient temperature of

steel was measured as the flame moved. These results were used to quantify the effect of torch movement on temperature distribution. This research concluded that modelling flame cambering with a moving Gaussian distribution is effective. However, the model presented in this research also required controlling the temperature distribution at each node along the path of the flame. The heat transfer parameters are established for specific lab conditions, where the environment and application of heat is consistent and therefore are not directly applicable to heat straightening in field conditions. The modelling concepts in this research are used to model flame cambering in nautical construction applications (Moshaiov & Latorre, 1985). These concepts used for flame cambering can also be used to model heat straightening.

In [Kowalkowski, 2005], vee heat straightening and strip heat shortening are studied to remediate curved girders and elongated column specimens. The finite element models developed used spring elements to model the varying force from hydraulic jacks and four node shell elements to model the steel components. Kowalkowski [2005] uses a sequential coupled thermal-stress analysis requiring a thermal analysis followed by a FEA of the mechanical aspects of heat straightening. The heat transfer associated with heat straightening was modelled using a finite difference model (FDM). The FDM was used to generate temperature-time curves of each node to emulate the meandering motions of the torch associated with heat straightening. The integration of this finite difference model requires experimental temperature data to produce results in FEA. Thermal properties of steel were incorporated using normalized material data from [Roeder, 1986] for the changes of yield stress, modulus of elasticity, and the coefficient of thermal expansion as temperatures increase. Damage in the specimens and finite element models were created using quasi-static loading. Kowalkowski conducted preliminary research comparing the results of a dynamic impact compared to a quasi-static impact using FEA. However, it is unclear if strain-rate effects of steel were included in these preliminary results.

In [Sharma, 2005] and [Connor, et al., 2008] studied heat straightening repair of plates and flanges bent along their weak axis. Deformations were created by gradually loading simply-supported plates in [Sharma, 2005] whereas a drop tower was used in [Connor, et al., 2008]. The FEA model in [Sharma, 2005] is used to optimize the line heating pattern used to repair weak axis damage; the damage in the model was created using a static point load. The model in [Connor, et al., 2008] was used to measure the residual stresses caused by impact; the impact

damage was created by modelling the displacement from experimental results. The results of these studies improved the understanding of how stress is affected by the damage geometry. However, these studies do not use FEA to model the heat straightening process or the dynamic effects associated with impact.

## 2.5 Indicial and Tensor Notation

The equations describing the concepts in Section 2.6 are written in terms of indicial and tensor notation. This section is a brief introduction to indicial and tensor notation. Indicial notation is a compact method of writing tensor operations.

A tensor is a mathematical term used to describe physical properties. The tensor is described by  $3^n$  components, where  $n$  is the order of the tensor. Scalars are zero-order tensors used to describe physical properties without direction such as temperature and time. Vectors are first-order ( $n=1$ ) tensors with 3 components used to describe position and velocity relative to a coordinate system. Examples of second-order tensors are stress and strain described with 9 components. The vector and tensors are denoted by bold font. The derivative of variables with respect to time are shown with a dot above. For example, the derivative of position with respect to time is

$$\dot{\mathbf{x}} = \frac{\partial \mathbf{x}}{\partial t} \quad (4)$$

Indicial notation is an efficient method of expressing mathematical operations on components of tensors. Components of vectors and tensors have subscripts, referred to as indices, denoted by lowercase Roman letters. For example,  $v_i$  is the  $i^{\text{th}}$  component of vector  $\mathbf{v}$ . Within this document the indices range from 1 to 3. Consider the Cauchy stress tensor:

$$\boldsymbol{\sigma} \equiv \sigma_{ij} \mathbf{e}_i \mathbf{e}_j = \begin{bmatrix} \sigma_{11} & \sigma_{12} & \sigma_{13} \\ \sigma_{21} & \sigma_{22} & \sigma_{23} \\ \sigma_{31} & \sigma_{32} & \sigma_{33} \end{bmatrix} \quad (5)$$

where  $\sigma_{ij}$  are the Cauchy stress components,  $\mathbf{e}_i$  and  $\mathbf{e}_j$  are unit vectors of a coordinate system. The components of this stress tensor can be written with indicial notation as  $\sigma_{ij}$ , where  $i$  and  $j$  are indices ranging from 1 to 3. As mentioned earlier, vectors are first-order tensors with 3

components so the components of vectors for position  $\mathbf{u}$  and velocity  $\mathbf{v}$  are written with a single index as  $x_i$  and  $v_i$ , respectively. Consider the sum:

$$S = \sum_{i=1}^3 a_i x_i = a_1 x_1 + a_2 x_2 + a_3 x_3 \quad (6)$$

where  $a_i$  and  $x_i$  are the components of vector  $\mathbf{a}$  and  $\mathbf{x}$ . The summation  $S$  can be written as  $a_i x_i$  using indicial notation, where repeat indices imply summations. This summation convention can be used to express different tensor operations (dot product, transpose, and trace) as shown in Table 2-2, where  $\mathbf{A}$ ,  $\mathbf{B}$ , and  $\mathbf{C}$  are second-order tensors.

**Table 2-2: Examples of tensor operations written with indicial and tensor notation.**

	Tensor Notation	Indicial Notation	Definition
<b>Dot Product:</b>	$\mathbf{C} = \mathbf{A} \cdot \mathbf{B}$	$C_{ik} = A_{ij}B_{jk}$	$C_{ik} = \sum_{j=1}^3 A_{ij}B_{jk}$
<b>Dot Product and Tranpose:</b>	$\mathbf{C} = \mathbf{A}^T \cdot \mathbf{B}$	$C_{ik} = A_{ji}B_{jk}$	$C_{ik} = \sum_{j=1}^3 A_{ji}B_{jk}$
<b>Trace:</b>	$tr(\mathbf{A})$	$A_{kk}$	$\sum_{k=1}^3 A_{kk} = A_{11} + A_{22} + A_{33}$

Kronecker delta is a commonly used tensor used in continuum mechanics. Kronecker delta,  $\delta_{ij}$ , is defined as:

$$\delta_{ij} = \begin{cases} 1 & \text{if } i = j \\ 0 & \text{if } i \neq j \end{cases} \quad (7)$$

The identity tensor is defined as:

$$\mathbf{I} = \delta_{ij} \mathbf{e}_i \mathbf{e}_j = \begin{bmatrix} 1 & 0 & 0 \\ 0 & 1 & 0 \\ 0 & 0 & 1 \end{bmatrix} \quad (8)$$

## 2.6 Continuum Mechanics of Deformable Bodies

This chapter is a brief introduction of continuum mechanics and how it is used to describe equilibrium of a deformable solid, and heat transfer [Belytschko, et al., 2000; Dassault Systèmes,

2011]. All of which are important for describing the physics and governing equations to be approximated by FEA. Continuum mechanics is the study of motion and behaviour of materials modelled as a continuous body.

### 2.6.1 Kinematics of Deformable Bodies

Consider a deformable continuous body, where the undeformed position of the material point  $P$  in the undeformed body is  $\mathbf{X}$ . The deformed position of the material point  $P$  is  $\mathbf{x}$ . Figure 2-9 shows the continuous body undergoing deformation to time  $t$  and the notation describing the motion of the body.

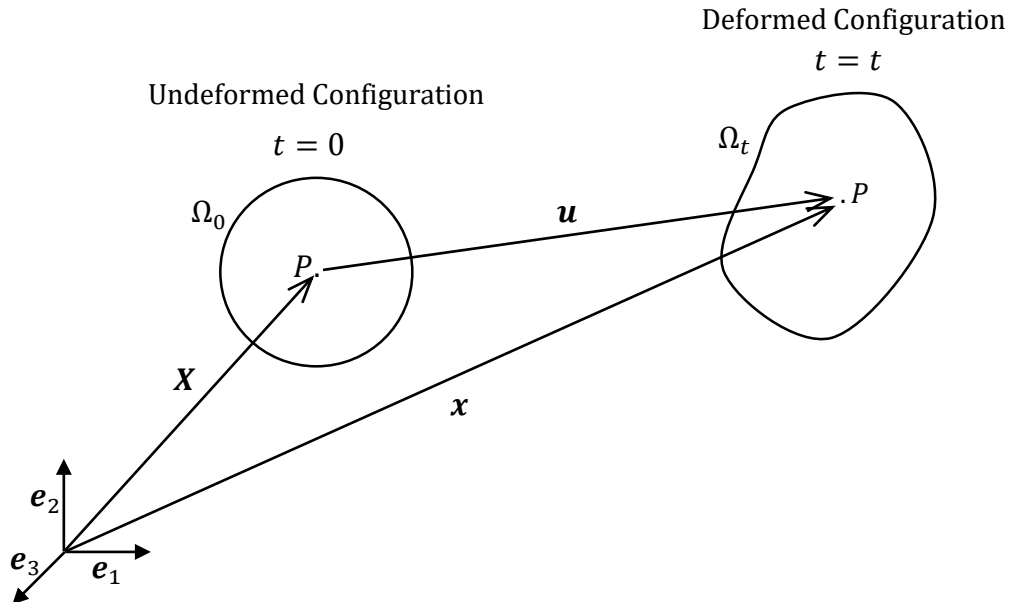


**Figure 2-9: Deformation of a continuous body [Belytschko, et al., 2000].**

The domain of the continuous body in the undeformed and deformed configuration are denoted by  $\Omega_0$  and  $\Omega_t$ , respectively. The displacement of material point  $P$  is denoted as  $\mathbf{u}$  and is given by:

$$\mathbf{u} = \mathbf{x} - \mathbf{X} \quad (9)$$

The deformation gradient tensor is an important quantity used to calculate strains. Consider an infinitesimal line segment  $d\mathbf{X}$  in the undeformed configuration.  $d\mathbf{X}$  is transformed

to  $d\mathbf{x}$  in the deformed configuration. The deformation tensor  $\mathbf{F}$  relates  $d\mathbf{X}$  and  $d\mathbf{x}$  and defines the changes of the line segment from the undeformed to the deformed configuration:

$$d\mathbf{x} = \mathbf{F} \cdot d\mathbf{X} \quad (10)$$

The components of the deformation gradient tensor  $\mathbf{F}$  are:

$$F_{ij} = \frac{\partial x_i}{\partial X_j} \quad (11)$$

and using (9) can be written:

$$F_{ij} = \frac{\partial u_i}{\partial X_j} + \delta_{ij} \quad (12)$$

The components of deformation gradient can be divided into elastic and plastic parts using a multiplicative decomposition:

$$F_{ik} = F_{ij}^e F_{jk}^{pl} \quad (13)$$

where  $F_{ij}^e$  and  $F_{jk}^{pl}$  are the plastic and elastic components of the deformation gradient, respectively. The relationship described in the multiplicative decomposition is shown on an arbitrary element in Figure 2-5. Figure 2-5 describes how the total deformation  $\mathbf{F}$  can be decomposed into first an elastic deformation phase followed by a plastic deformation phase.

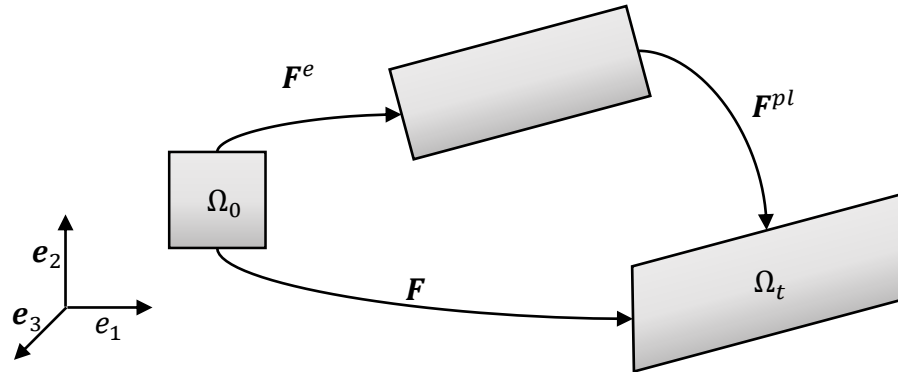


**Figure 2-10: Elastic and plastic decomposition of the deformation gradient of an element.**

The elastic deformation gradient elastically stretches and rotates the element. The plastic deformation causes non-reversible deformation to the element. The components of the plastic deformation gradient are defined by rewriting (13) as

$$F_{ik}^{pl} = F_{ij}^{-1} F_{jk}^e \quad (14)$$

The plastic and elastic parts of the deformation gradient are used to calculate the plastic and elastic strains, respectively.

The plastic strains are calculated using the rate of deformation tensor  $\mathbf{D}$ . The rate of deformation is calculated using the velocity gradient tensor  $\mathbf{L}$ .  $\mathbf{L}$  relates the velocities of two neighbouring material points with respect to the deformed configuration. The velocity is defined as the derivative of displacement with respect to time:

$$v_i = \frac{du_i}{dt} \quad (15)$$

The components of the velocity gradient  $\mathbf{L}$  are written in terms of velocity and the deformation gradient:

$$L_{ij} = \frac{\partial v_i}{\partial x_j} = \frac{d}{dt} \left( \frac{\partial u_i}{\partial X_k} \right) \left( \frac{\partial X_k}{\partial x_j} \right) = \dot{F}_{ik} F_{kj}^{-1} \quad (16)$$

The velocity gradient can be separated into symmetric and skew-symmetric parts:

$$L_{ij} = D_{ij} + W_{ij} \quad (17)$$

The rate of deformation  $\mathbf{D}$  and the material spin  $\mathbf{W}$  are the symmetric and skew-symmetric parts of the velocity gradient, respectively. In subsequent sections,  $\mathbf{D}$  and  $\mathbf{W}$  are used to define plastic strains and objective rates of stress.

Defining plastic strains requires the plastic rate of deformation  $\mathbf{D}^{pl}$ . The components of  $\mathbf{D}^{pl}$  can be separated from the components of the total rate of deformation  $\mathbf{D}$  and elastic rate of deformation  $\mathbf{D}^e$  with additive decomposition:

$$D_{ij} = D_{ij}^e + D_{ij}^{pl} \quad (18)$$

The additive decomposition of  $\mathbf{D}$  is derived from the multiplicative decomposition  $\mathbf{F}$ . Note that (18) is not a true separation of elastic and plastic deformation.  $\mathbf{D}^{pl}$  contains contributions from  $\mathbf{F}^e$  and so  $\mathbf{D}^{pl}$  is not independent of the elastic deformation in the way  $\mathbf{F}^{pl}$  is, see [Dassault Systèmes, 2011].

## 2.6.2 Strain

The Green-Lagrange strain and Infinitesimal strain are commonly used to describe deformation in continuum mechanics. Both strain measures are commonly used in FEA. The deformation gradient is used to derive the Green-Lagrange and Infinitesimal strain measures.

The Green-Lagrange strain measure is convenient to use for large deformations with large rotations. The components of the Green-Lagrange strain tensor are

$$E_{ij} = \frac{1}{2} (F_{ik}^T F_{kj} - \delta_{ij}) = \frac{1}{2} \left( \frac{\partial u_i}{\partial X_j} + \frac{\partial u_j}{\partial X_i} + \frac{\partial u_k}{\partial X_i} \frac{\partial u_k}{\partial X_j} \right) \quad (19)$$

where the  $(\partial u_k / \partial X_i)(\partial u_k / \partial X_j)$  term describes non-linear strains and rigid body rotations that occur during large deformations. Consider the Green-Lagrange strain in one dimension for an elastic bar uniformly strained:

$$E_{11} = \frac{1}{2} \left( 2 \frac{\partial u_1}{\partial X_1} + \left( \frac{\partial u_1}{\partial X_1} \right)^2 \right) \approx \frac{\Delta l}{l_0} + \frac{1}{2} \left( \frac{\Delta l}{l_0} \right)^2 \quad (20)$$

where  $\partial u_1 / \partial X_1 = \Delta l / l_0$ ,  $\Delta l$  is the change in the bar length and  $l_0$  is the original length of the bar. When deformations are small, the squared term in (20) is effectively zero and the engineering strain approximates the Green-Lagrange strain. The Green-Lagrange strain rate is related to rate of deformation

$$\dot{\mathbf{E}} = \mathbf{F}^T \cdot \mathbf{D} \cdot \mathbf{F} \quad (21)$$

This relationship between the Green-Lagrange strain rate and the rate of deformation is often used in constitutive modelling of materials [Belytschko, et al., 2000].

The infinitesimal strain measure is appropriate for small deformations and strains. Components of the infinitesimal strain tensor are

$$\epsilon_{ij} = \frac{1}{2} \left( \frac{\partial u_i}{\partial X_j} + \frac{\partial u_j}{\partial X_i} \right) \quad (22)$$

The infinitesimal strain in one dimension is

$$\epsilon_{11} = \frac{\partial u_1}{\partial X_1} \approx \frac{\Delta l}{l_0} \quad (23)$$

where  $\Delta l$  are length changes in the bar and  $l_0$  is the original length of the bar. Equation (23) shows that the infinitesimal strain tensor in one dimension is the engineering strain.

In reality, strain is three-dimensional. Strains measured in uniaxial tension testing are given as effective strains. The effective strain describes the magnitude of the total strain.

The effective strain is calculated by:

$$\bar{E} = \sqrt{\frac{2}{3} E_{ij} E_{ij}} \quad (24)$$

where  $\bar{E}$  is the effective strain and  $E_{ij}$  are components of the Green-Lagrange strain. The plastic part of effective strain is often used to define relations between material strain and flow stress. The effective plastic strain is

$$\bar{E}^{pl} = \int_0^t \sqrt{\frac{2}{3} D_{ij}^{pl} D_{ij}^{pl}} dt \quad (25)$$

where  $D^{pl}$  is the plastic rate of deformation calculated using the multiplicative decomposition of the deformation gradient (13). Effective plastic strain rate is

$$\dot{\bar{E}}^{pl} = \sqrt{\frac{2}{3} D_{ij}^{pl} D_{ij}^{pl}} \quad (26)$$

Effective plastic strain rate is used to define material strain-rate sensitivity in constitutive laws. Material data for flow stress is defined with respect to effective plastic strain and effective plastic strain rate in FEA software, which will be discussed below.

### 2.6.3 Stress

Cauchy stresses are calculated using forces and areas in the deformed configuration. Cauchy stress ( $\sigma$ ) is a symmetric tensor defined by using nine components, six components which are unique. Consider a point in a body as an infinitesimal cube, as shown in Figure 2-11.

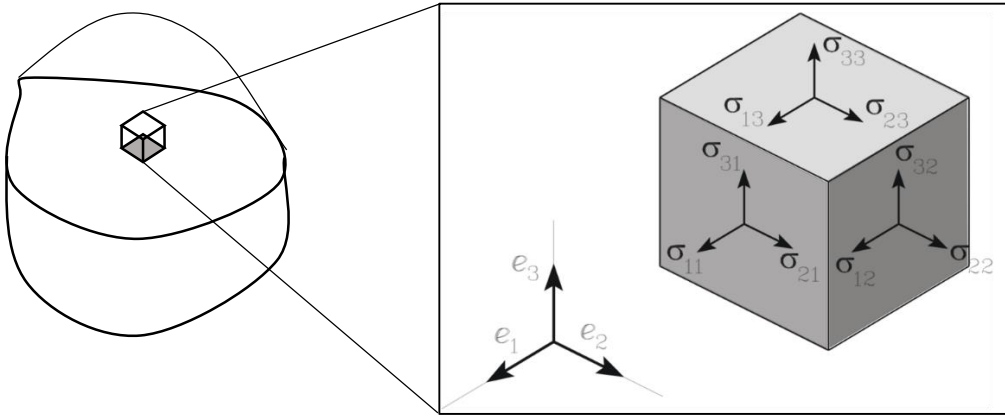


**Figure 2-11: Nine components of stress at a point in a continuous body.**

Figure 2-11 shows the nine components of stress defined as a force per unit area.  $\sigma$  can also be written as an array with six components using Voigt notation because the tensor is symmetric. The first and second indices indicate the direction of force and normal direction of the face, respectively.

According to Cauchy's stress theorem, any surface traction can be expressed in terms of the Cauchy stress. Consider a plane in the deformed configuration with normal  $\mathbf{n}$  is subjected to stress vector (traction)  $\mathbf{t}$ , as shown in the Figure 2-12.

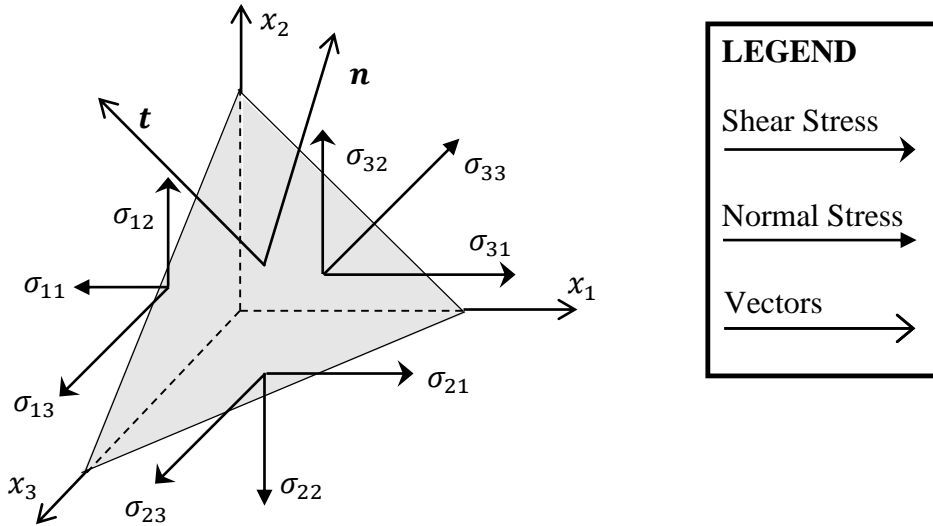


**Figure 2-12: Stress vector acting on an arbitrary plane.**

The components of the traction vector, in the deformed configuration, is defined by the Cauchy stress:

$$t_i = \sigma_{ji} n_j \quad (27)$$

The Cauchy stress is dependent on the orientation of the coordinate system. The three eigenvalues of a Cauchy stress tensor are called principal stresses. Principal stresses are normal stresses that occur in a rotated coordinate system where no shear stresses are present. The principal stresses  $\sigma_1$ ,  $\sigma_2$ , and  $\sigma_3$  are ordered such that  $\sigma_1 \geq \sigma_2 \geq \sigma_3$ .

Effective stress can be calculated from principal stresses of any material point. Effective stress is defined as:

$$\bar{\sigma} = \frac{1}{\sqrt{2}} \sqrt{(\sigma_1 - \sigma_2)^2 + (\sigma_1 - \sigma_3)^2 + (\sigma_2 - \sigma_3)^2} \quad (28)$$

where  $\sigma_1$ ,  $\sigma_2$ ,  $\sigma_3$  are principal stresses. The effective stress is commonly referred to as the Von Mises stress and is used to determine yielding. Flow stresses or yield stresses from uniaxial tension testing is given in relation to effective plastic strain. These material properties are used to define the elasto-plastic behaviour of steel in constitutive equations [Dassault Systèmes, 2011].

The Cauchy stress mentioned at the beginning of this section is one measure of stress. Other notable stress measures includes the 1<sup>st</sup> and 2<sup>nd</sup> Piola-Kirchhoff stress. The 1<sup>st</sup> Piola-Kirchhoff stress tensor, denoted by  $\tau$ , is the transpose of the nominal stress tensor  $\mathbf{P}$ . The 1<sup>st</sup> Piola-Kirchhoff stress is calculated using force components in the undeformed configuration with the areas of the deformed body. Second Piola-Kirchhoff stress, denoted by  $\mathbf{S}$ , is calculated by forces and areas in the undeformed configuration. However, when deformations are small, all stress measures are equivalent. These four stress measures are commonly used to define constitutive equations of stress versus strain.

The constitutive equations for stress-strain used in continuum mechanics are written to be frame indifferent, where the stress and strain do not change with rigid body rotation. Therefore, material properties are independent of the observer. The Jaumann objective rate is used in continuum mechanics to transfer the Cauchy stress to a frame indifferent form. The Jaumann rate for Cauchy stress is defined

$$\boldsymbol{\sigma}^{\nabla J} = \frac{D\boldsymbol{\sigma}}{Dt} - \mathbf{W} \cdot \boldsymbol{\sigma} - \boldsymbol{\sigma} \cdot \mathbf{W}^T \quad (29)$$

where  $\sigma^{\nabla J}$  is the Jaumann rate of Cauchy stress,  $D\sigma/Dt$  is the material time derivative for Cauchy stress and  $\mathbf{W}$  is the material spin described in the Kinematics section. The Jaumann rate of Cauchy stress accounts for changes in stress due to changes in material and rotation, accounted for as the 2<sup>nd</sup> and 3<sup>rd</sup> term of (29) [Belytschko, et al., 2000]. This is used in computations particularly for large deformations associated with impact damage, which is why constitutive laws are often written in terms of  $\sigma^{\nabla J}$  and  $\mathbf{D}$ .

## 2.6.4 Constitutive Equations for Stress-Strain

Constitutive equations are used to relate stress and strain in a material. The material response is separated into elastic and elasto-plastic constitutive equations. The elasto-plastic constitutive equations also incorporates the rate-dependent material response, which is an important parameter in modelling impact. Figure 2-13 shows stress-strain curve for a typical metal measured by effective stress and effective strain.

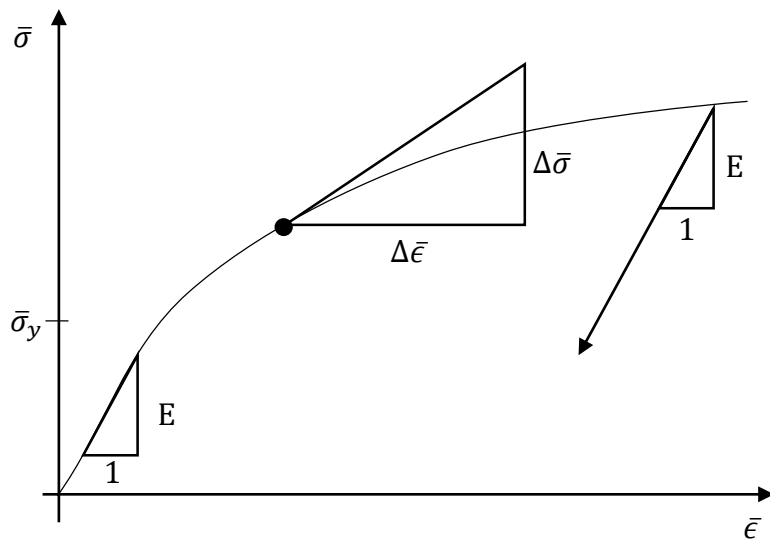


**Figure 2-13: Stress-strain curve for a typical metal with effective stress and strain.**

In Figure 2-13, the yield stress is denoted by  $\bar{\sigma}_y$ , and the modulus of elasticity is denoted by  $E$ . The elastic constitutive equation governs the stress-strain relationship during loading and unloading when  $\sigma < \bar{\sigma}_y$ . During inelastic deformation, the elasto-plastic constitutive equation

governs the changes in stress. After yielding, the elasto-plastic tangent modulus is calculated in stress increments to define the plastic behaviour of the material.

The elastic constitutive model used is known as a Saint-Venant-Kirchhoff model, where the material experiences large rotations and small strains for elasticity. The Saint-Venant-Kirchhoff model is written

$$\mathbf{S} = \mathbf{C}^e : \mathbf{E} \quad C_{ijkl}^e = \lambda \delta_{ij} \delta_{kl} + \mu (\delta_{ik} \delta_{jl} + \delta_{il} \delta_{jk}) \quad (30)$$

where  $\mathbf{S}$  is the 2<sup>nd</sup> Piola-Kirchhoff stresses,  $\mathbf{C}^e$  is the fourth-order elastic stiffness tensor,  $\mathbf{E}$  is the Green-Lagrange strains,  $\mu$  and  $\lambda$  are Lamé constants.

When the effective stress is above the flow stress, the elasto-plastic constitutive equation governs the stress-strain relationship

$$\boldsymbol{\sigma}^{\nabla J} = \mathbf{C}^{ep} : \mathbf{D} \quad (31)$$

where  $\boldsymbol{\sigma}^{\nabla J}$  is the Jaumann Cauchy stress rate,  $\mathbf{C}^{ep}$  is the elasto-plastic tangent modulus tensor, and  $\mathbf{D}$  is the rate of deformation. The elasto-plastic constitutive equations are commonly given in incremental stress form. The elasto-plastic tangent modulus tensor is calculated using the plastic flow stress material properties.

#### 2.6.4.1 Physical Interpretation of $\mathbf{C}^{ep}$

Consider calculating the elasto-plastic tangent modulus in one dimension, assuming the material is undergoing plastic deformation. Since there is no material spin considered in one dimension then the Jaumann objective rate is equal to the stress rate and the elasto-plastic equation is rewritten as

$$\boldsymbol{\sigma}^{\nabla J} = \frac{D\boldsymbol{\sigma}}{Dt} \rightarrow C^{ep} D_{11} = \dot{\sigma}_{11} \quad (32)$$

Using the definitions for effective plastic strain and effective stress, the rate of deformation and stress are rewritten as

$$\dot{\bar{E}}_{11} = \sqrt{\frac{2}{3}} D_{11} \rightarrow D_{11} = \sqrt{\frac{3}{2}} \dot{\bar{E}}_{11} \quad (33)$$

$$\dot{\bar{\sigma}}_{11} = \sqrt{\frac{3}{2}} \dot{\sigma}_{11} \rightarrow \dot{\sigma}_{11} = \sqrt{\frac{3}{2}} \dot{\bar{\sigma}}_{11} \quad (34)$$

Substituting equations (33) and (34) into (32), the elasto-plastic tangent modulus  $C^{ep}$  in one-dimension can be solved.

$$C^{ep} \sqrt{\frac{3}{2}} \dot{\bar{E}}_{11} = \sqrt{\frac{3}{2}} \dot{\bar{\sigma}}_{11} \therefore C^{ep} = \frac{\dot{\bar{\sigma}}_{11}}{\dot{\bar{E}}_{11}} \approx \frac{\Delta \bar{\sigma}}{\Delta \bar{E}} \quad (35)$$

This simplification shows that  $C^{ep}$  is the same as the slope in a stress-strain curve after yielding as shown in Figure 2-13.

## 2.6.5 Governing Equations for Mechanical Deformation

The deformation of a continuous body is governed by the conservation of linear momentum, which in the deformed configuration is:

$$\rho \frac{D\boldsymbol{v}_i}{Dt} = \boldsymbol{f}_i + \frac{\partial \boldsymbol{\sigma}_{ij}}{\partial x_j} \quad (36)$$

where  $\rho$  is the mass density,  $\boldsymbol{v}$  is velocity vector,  $\boldsymbol{f}$  is the body force vector per unit mass, and  $\boldsymbol{\sigma}$  is the Cauchy stress tensor. The rate of change in momentum from inertia effects, on the left hand side of the equation, can be removed to simplify the equation for static problems.

$$0 = \boldsymbol{f}_i + \frac{\partial \boldsymbol{\sigma}_{ij}}{\partial x_j} \quad (37)$$

The body forces  $\boldsymbol{f}$  are exerted over the volume of the body, which includes forces from gravity and electromagnetism. The term with Cauchy stress represents forces from internal stresses.

## 2.6.6 Constitutive Equations for Heat Transfer

Three major sources of heat flux contribute to heat transfer: Conduction, Convection, and Radiation. The constitutive equation relating temperature to heat flux for each source of energy is different. Each equation describes heat transfer relative to a deformed body shown in Figure 2-14.

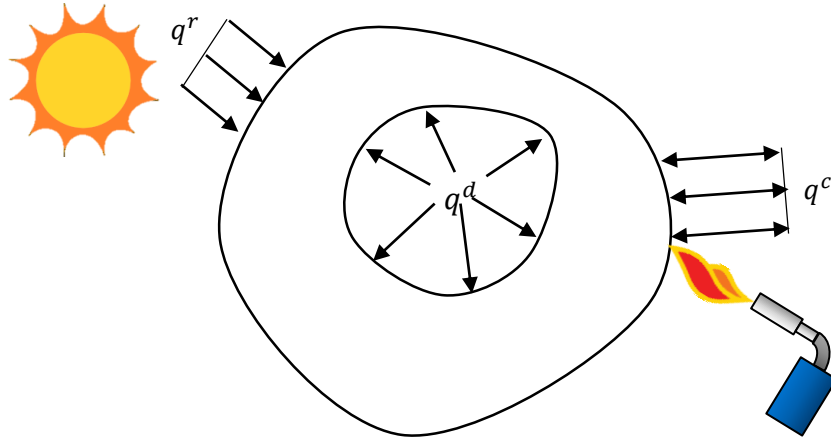


**Figure 2-14: Sources of heat transfer for a deformable body.**

In the model, convection was used as a source of introducing and removing heat, as discussed in Section 4.1. Radiation was also used as a source removing heat, which differs from Figure 2-14. The heat flux from the sun was used to depict a source of radiation.

Conduction is governed by the transfer of energy through contact. The heat is transferred from bodies to cooler bodies, it is the most effective method of heat transfer. Fourier's law describes the components of heat flux density from conduction through a body:

$$q_i^d = -k \frac{\partial T}{\partial x_i} \quad (38)$$

where  $q^d$  is the heat flux density from conduction,  $k$  is the thermal conductivity,  $T$  is temperature of the material.

Through convection energy of a surface is transferred through the interaction of a surface with surrounding fluids. The convection heat flux density is normal to a surface of a body:

$$q^c = h(T^S - T^A) \quad (39)$$

where  $q^c$  is the convective heat flux density,  $h$  is the convection coefficient,  $T^S$  is the surface temperature, and  $T^A$  is the air temperature. The convection coefficient is dependent on properties of the surrounding fluid and the flow rate.

Radiation is governed by the transfer of energy with electromagnetic radiation through a vacuum. The Stefan-Boltzmann radiation heat flux equation is normal to the surface of a body:

$$q^r = \epsilon\sigma((T^S)^4 - (T^E)^4) \quad (40)$$

where  $q^r$  is the heat flux from radiation,  $\epsilon$  is the emissivity of the steel,  $\sigma$  is the Stefan-Boltzmann constant at  $5.670373 \times 10^{-8} \text{ W/m}^2\text{K}^4$  not to be confused with stress. The surface temperature,  $T^S$ , and temperature of radiation source,  $T^E$ , in the radiation heat flux equation are given in Kelvin. Convection and radiation heat flux are significant sources of external heating and cooling steel during heat straightening.

### 2.6.7 Governing Equations for Heat Transfer

The heat transfer is governed by the conservation of energy, which is written in the deformed configuration as:

$$\rho c^a \frac{dT}{dt} = \frac{\partial q_i}{\partial x_i} + S \quad (41)$$

where  $\rho$  is mass density,  $c^a$  is the specific heat,  $dT/dt$  is the change of temperature with respect to time,  $\mathbf{q}$  is internal heat flux due to conduction, and  $S$  is the surface heat from external sources. The left-hand side of the equation represents the change of energy in the body due to heat transfer.

### 2.6.8 Temperature-Effects on Mechanical Deformation

Deformations caused by heat transfer are governed by both conservation of energy and the conservation of linear momentum. Constitutive equations written for stress-strain and heat transfer also apply. In addition to the kinematics of deformable bodies, thermal expansion and contraction from heat transfer contribute to strains. Thermal strains are calculated by:

$$E_{ij}^{th} = (\alpha^0(T - T^0) - \alpha^I(T - T^I))\delta_{ij} \quad (42)$$

The coefficients of thermal expansion at the reference and initial temperatures are denoted with  $\alpha^0$  and  $\alpha^I$ , respectively. The material, reference, and initial temperatures are noted with  $T$ ,  $T^0$ , and  $T^I$ , respectively. Thermal strains are added to existing strains from deformation:

$$E_{ij} = E_{ij}^0 + E_{ij}^{th} \quad (43)$$

where  $E$  is the total strain,  $E^0$  is the strain from deformation, and  $E^{th}$  is the thermal strain. These additional strains are localized to regions where temperatures are elevated. The elevated temperatures also cause reductions in the modulus of elasticity and flow stresses. These changes in material properties are implemented into the static material data using multiplicative composition, as shown in Section 4.2.

### 3 Two-Dimensional Impact Modelling

This chapter introduces concepts used for impact modelling in this research. The concepts were evaluated using two-dimensional plane strain finite element models. Two dimensional models were chosen to minimize the computation time for each analysis. Each model was assessed for impacts causing different magnitudes of damage. The impact damage was created using quasi-static and dynamic loading. Models with similar deflections were compared using measurements of residual stress, plastic strain, and displacement. The finite element analysis (FEA) was performed using ABAQUS [Dassault Systèmes, 2011], a commercial FEA software capable of quasi-static and dynamic analyses.

Research projects studying the material properties after heat straightening are based on remediating damage from quasi-static loading. Creating dynamic loads, similar to those found in impacts between over-height vehicles and bridges, is more difficult but may provide more realistic results. Steel is a strain-rate sensitive material and the apparent yield strength of steel can be up to 50% higher during impact than the quasi-static yield strength. In [Sharma, 2005] and [Liu, 2006] heat straightened specimens damaged using quasi-static loading. In [Connor, et al., 2008], the specimens were damaged using a custom “drop tower”. The recommended limitations of heat straightening from the research using quasi-static loading were lower than limitations from the research using dynamic loading.

In the finite element models, quasi-static loading is controlled by defining the displacement of the impactor. Dynamic loading is controlled by defining the impactor mass and the initial impact velocity. In addition to dynamic loading, the Cowper-Symonds parameters are added to model the steel strain rate sensitivity. Quasi-static load cases are tested in 5 mm increments. Dynamic load cases are evaluated based on a combination of impactor mass and impact velocity. In particular, impact velocities associated with common speed limits, i.e. 60 km/h, 90 km/h, 120 km/h, are evaluated.

#### 3.1 Tee and Wide Flange Models

In this experiment, a rigid 25 mm diameter impactor of varying mass and velocity will strike the steel sections as shown in Figure 3-1. Two different steel sections were modelled: a

plate girder and a tee section. The plate girder and tee sections were modelled to investigate how impact affects single and double curvature deformation similar to cantilever and beam support conditions. The sections were designed such that the residual stresses and significant deformation resided in the web. The plate girder was simplified using symmetrical boundary conditions as shown in Figure 3-1.

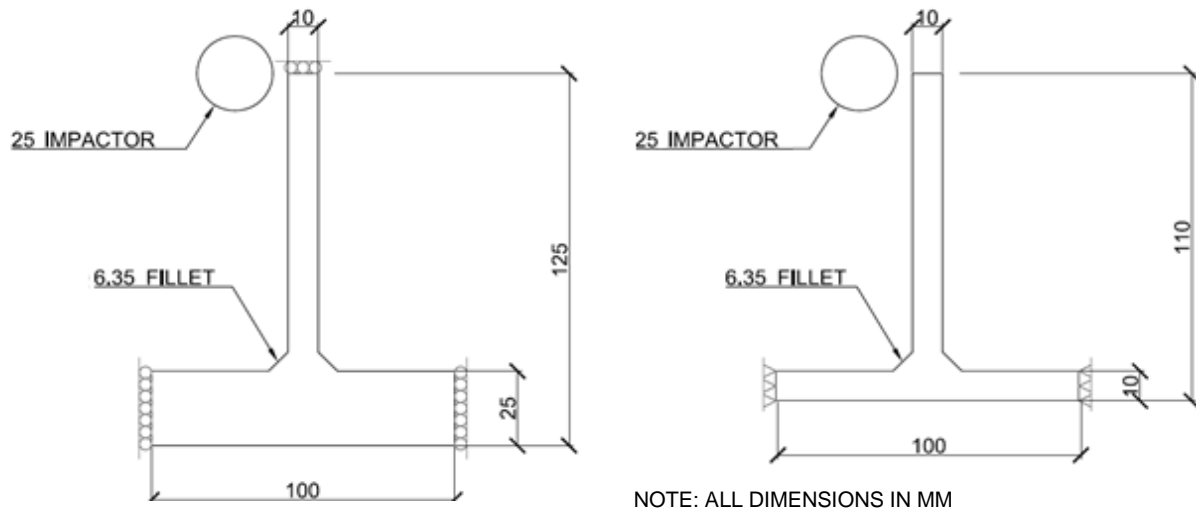


**Figure 3-1: Boundary conditions and dimensions for plate girder and tee sections.**

The ends of the flange are restrained from moving horizontally for the plate girder and the ends of the flange for the tee section are restrained from moving horizontally and vertically. The web thickness of the sections are 10 mm thick and 100 mm long. The flanges are 100 mm wide; whereas the plate girder has a 25 mm thick flange and the tee has a 10 mm thick flange. The flange thickness of the plate girder was increased to reduce the stress applied onto the flanges. 6.35 mm wide fillets are placed on each side of the web at the intersections of the web and flange. The fillets were included in the geometry and modelled using the same material properties as the plate girder and tee sections.

4-node bilinear plane strain elements (CPE4) and rigid 2-node discrete elements (R2D2) were used for the steel sections and impactor surface, respectively. The mass of impactor was specified as a point mass located at the center of the impactor.

The steel sections were subjected to quasi-static and dynamic loading cases. The quasi-static loading was created by controlling the displacement of the impactor. The impactor displaced the section 15 mm with quasi-static loading. Additional Quasi-static loading cases

were created at 5 mm increments until the displacement, measured 100 mm from the base of the web opposite the face of impact, matched the dynamic loading cases which peaked at 40 mm. The dynamic loading was caused by a combination of impactor masses of 20 g, 30 g, 40 g and the impact velocities tested were 17 m/s, 25 m/s, and 34 m/s or approximately 60 km/h, 90 km/h, 120 km/h. The loading cases were assessed for deformations, stresses, and strains after loading was removed.

The material properties of steel is defined as shown in Table 3-1.

**Table 3-1: General material properties of steel.**

Property	Value
Modulus of Elasticity	200 GPa
Poisson's Ratio	0.3
Density	7.85 g/cm <sup>3</sup>

The steel plasticity was modelled using an isotropic rate-dependent model. The flow stress function was defined in ABAQUS with a table of flow stress and equivalent plastic strain. Figure 3-2 is the equivalent flow stress versus effective plastic strain used to define the plastic response of CSA 350w.

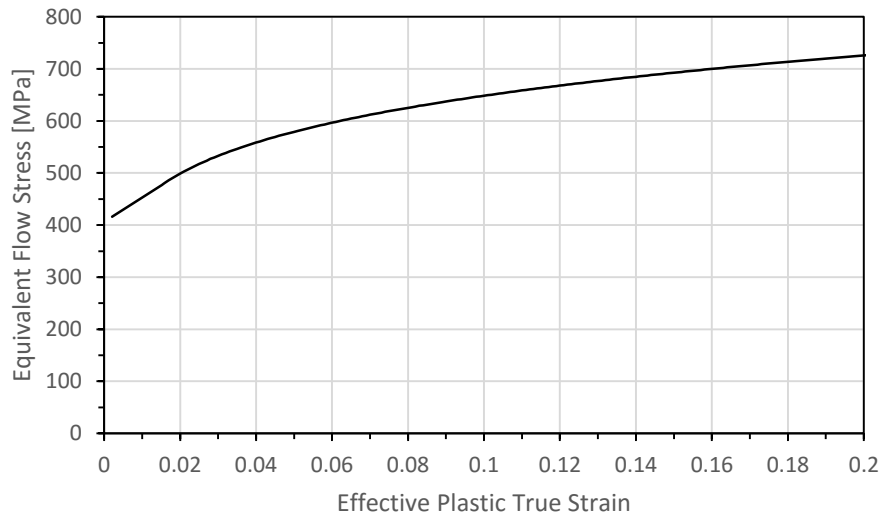


**Figure 3-2: Flow stress versus effective plastic true strain of CSA 350w**  
[Arasaratnam, et al., 2011].

The flow stress versus effective plastic true strain in Figure 3-2 was created from uniaxial tension data for CSA 350W from [Arasaratnam, et al., 2011]. The CSA 350W steel data will also be

important for modelling the impact and heat straightening in Section 5.2.1 for the material properties of a Canadian steel bridge.

The dynamic flow stress associated with strain-rate sensitivity is modelled using the Cowper-Symonds model shown:

$$\bar{\sigma}^d(\bar{\sigma}^s, \dot{\bar{E}}^{pl}) = \left( 1 + \left( \frac{\dot{\bar{E}}^{pl}}{r} \right)^{\frac{1}{q}} \right) \bar{\sigma}^s \quad (44)$$

where  $\bar{\sigma}^d$  is the dynamic equivalent flow stress,  $\bar{\sigma}^s$  is the static equivalent flow stress from Figure 3-2,  $\dot{\bar{E}}^{pl}$  is the effective plastic strain rate described in Section 2.6.2,  $r$  and  $q$  are Cowper-Symonds parameters. The Cowper-Symonds model is widely used to model the strain-rate sensitivity of steel for a given plastic strain rate [Fire and Blast Information Group, 2001]. The Cowper-Symonds parameters  $q$  and  $r$  are  $6844 \text{ s}^{-1}$  and 3.91, respectively, which are appropriate for mild steel behaviour closer to ultimate tensile stress [Fire and Blast Information Group, 2001].

### 3.2 Results

The residual stress, strain, and displacements of the finite element model are calculated in ABAQUS after loads are removed. The values of the results are calculated at nodes. The stresses and strains are calculated by averaging the values of elements in contact with the nodes. Results were limited to loading causing a deformed shape with a displacement of 10 mm or greater because heat straightening repair is applied for deformations greater than 10 mm for the web [Alberta Transportation, 2004]. The results were calculated along two different paths as shown in Figure 3-3. Figure 3-3 shows that Path 1 is along the surface of the web and Path 2 is through the base of the web thickness respectively for both steel sections tested. The residual stresses and strains will be compared among results with similar deformed shapes. Bending stresses in the following figures refer to vertical stresses. Plastic strain in the following figures refers to the vertical plastic strains.

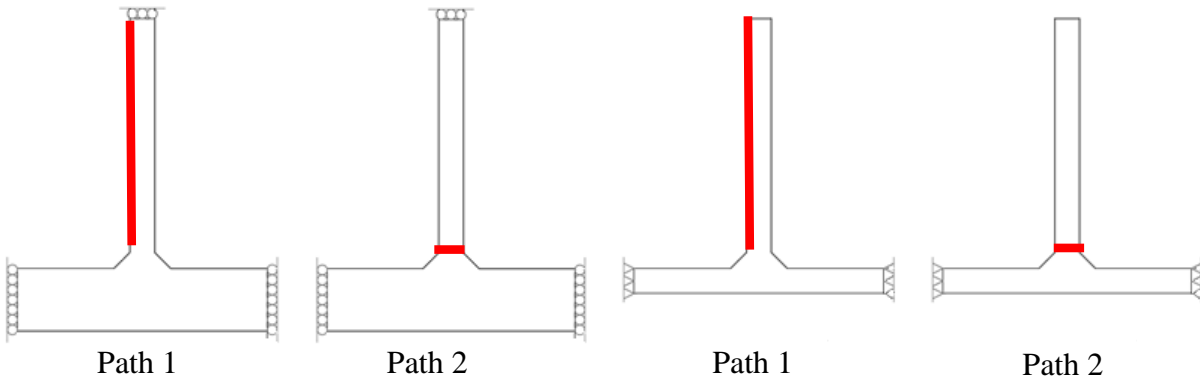


**Figure 3-3: Paths for results after impact for plate girder and tee section.**

### 3.2.1 Mesh Convergence Study

A mesh convergence study is performed to check the accuracy of the FEA as the number of elements increased. In particular, this mesh convergence study focused on changes to the stress distributions along Path 2 as the number of elements are increased. Increasing the number of elements in the model resulted in larger computation times required for each analysis.

Figure 3-4 shows the stress distributions with different number of elements across the web for the quasi-static and dynamic loading. The residual bending stress distributions in Figure 3-4 were results from models where a 20 g impactor impacted a plate girder section at 25 m/s and a 40 mm quasi-static displacement. These load cases caused similar deformed shapes differing less than 1 mm after loading was removed. 25 to 200 elements were used to discretize path 2 where the stresses were measured. For the dynamic loading, the median percent difference between 50 and 100 elements along path 2 was 15% and the median percent difference between 100 to 200 elements was 7%.

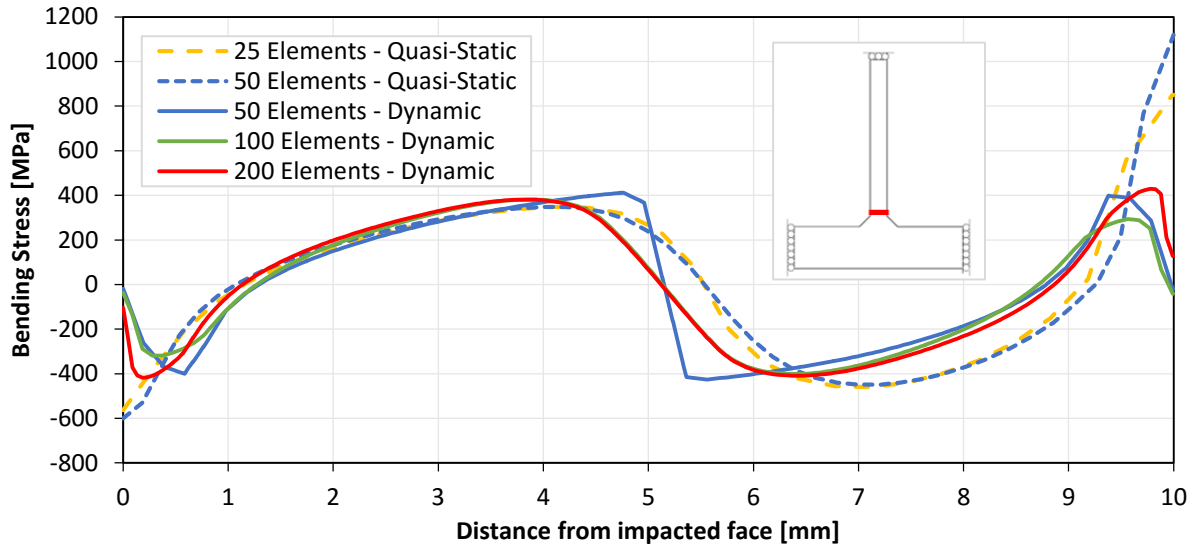
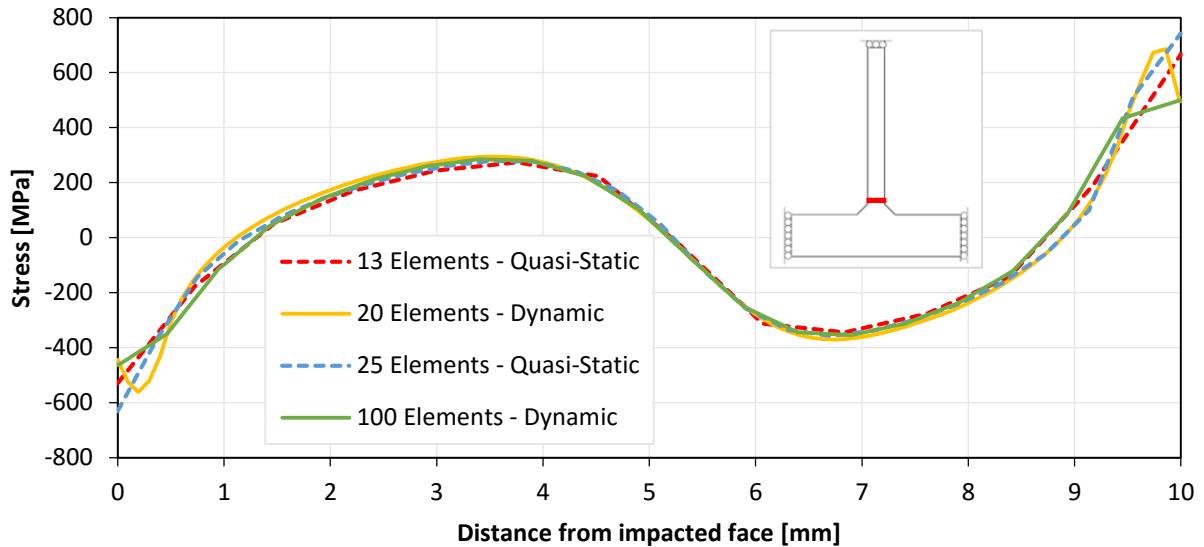


**Figure 3-4: Residual bending stress distributions along Path 2 discretized with different numbers of elements for a plate girder.**

The dynamic loading models with 200 elements along Path 2 required multiple hours to complete and the percent difference in stress along the majority of the web was below 10%. Modelling dynamic loading with 0.1 mm wide elements required significantly shorter computation times and was sufficiently precise for comparisons between loading types.

For the quasi-static models, the median percent difference between 25 and 50 elements across the web was 7% for the plate-girder sections. The analysis time using 50 elements to discretize Path 2 was approximately 10 minutes; Quasi-static loading was sufficiently modelled using 0.2 mm wide elements or 200 elements across Path 2. Additional mesh convergence studies were required to check the accuracy of the tee-section models.

Figure 3-5 shows residual bending stress along Path 2 for a tee section after a 40 mm quasi-static displacement and impact caused by a 30g impactor at 25 m/s using different numbers of elements to discretize Path 2. The median percent difference between the quasi-static loadings from using 13 elements to 25 elements was 6.4%. 25 elements or 0.4 mm wide elements were used in the quasi-static load cases for the tee section. The median percent difference between the dynamic experiments using 20 elements and 100 elements to discretize Path 2 was 5.8%. The dynamic loading model with 100 elements across Path 2 required approximately 10 minutes for computation time.



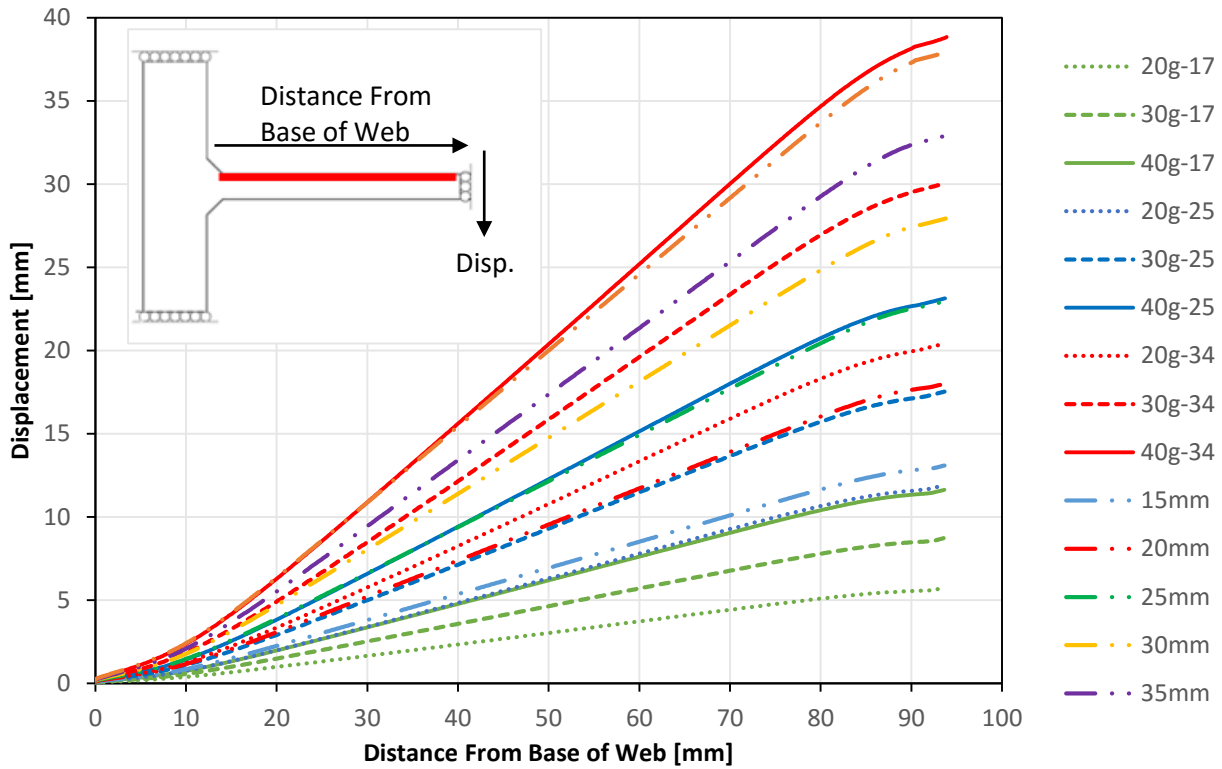
**Figure 3-5: Residual bending stress distributions along Path 2 discretized with different numbers of elements for a tee section.**

Figure 3-5 shows that the majority of the differences in the dynamic models are isolated within the first millimeters of the surface. 20 elements or 0.5 mm wide elements are used for the results of the dynamic experiments with the tee section.

In summary, the plate girder models using 0.1 mm and 0.2 mm wide elements for dynamic and quasi-static experiments, respectively, were sufficiently accurate for the comparison of residual stresses between impacts. The tee section models in the following section used 0.2 mm and 0.4 mm wide elements to discretize the section for dynamic and quasi-static loading, respectively.

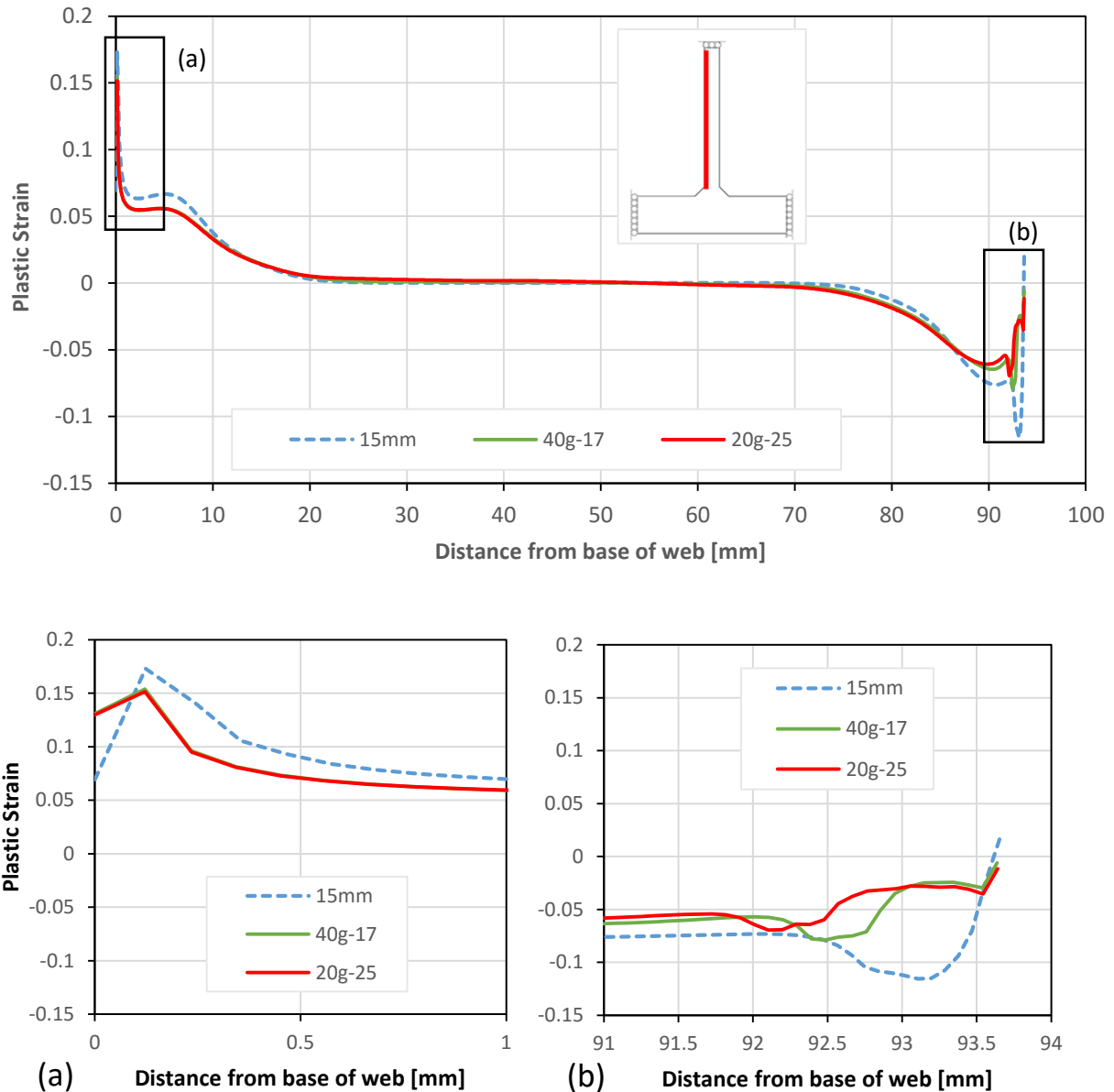
### 3.2.2 Plate Girder Results

In the following figures, **x** mm indicate that the result from an **x** mm displacement controlled impact and the **yy g- zz** refers to result from an impactor mass of **yy** grams/millimetre at an impact velocity in **zz** metres per second. Figure 3-6 shows the final deformed shape of the plate girder along Path 1 for various impacts from quasi-static and dynamic simulations.



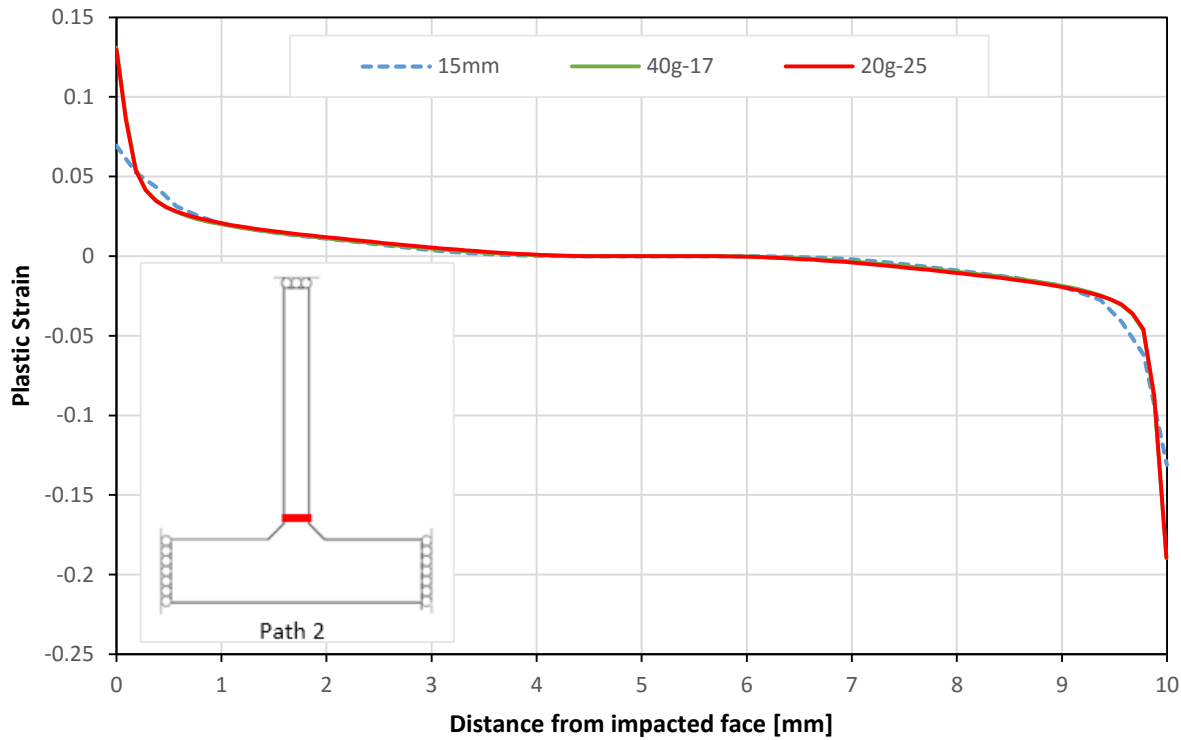
**Figure 3-6: Final displacement along Path 1 for quasi-static and dynamic load cases.**

The 15 mm quasi-static, 20g-25, and 40g-17 dynamic displacements had fairly similar deformations. The 15 mm quasi-static displacement loading caused a 13 mm final displacement measured on the web at the point of impact; impacts from a 20 g and 40 g impactor with a velocity of 25 m/s and 17 m/s respectively caused a 12 mm displacement. Figure 3-7 shows vertical plastic strain along Path 1 for the three experiments with similar deflected shape.



**Figure 3-7: Vertical plastic strain along Path 1 for 15mm, 20g-25, and 40g-17 experiments.**

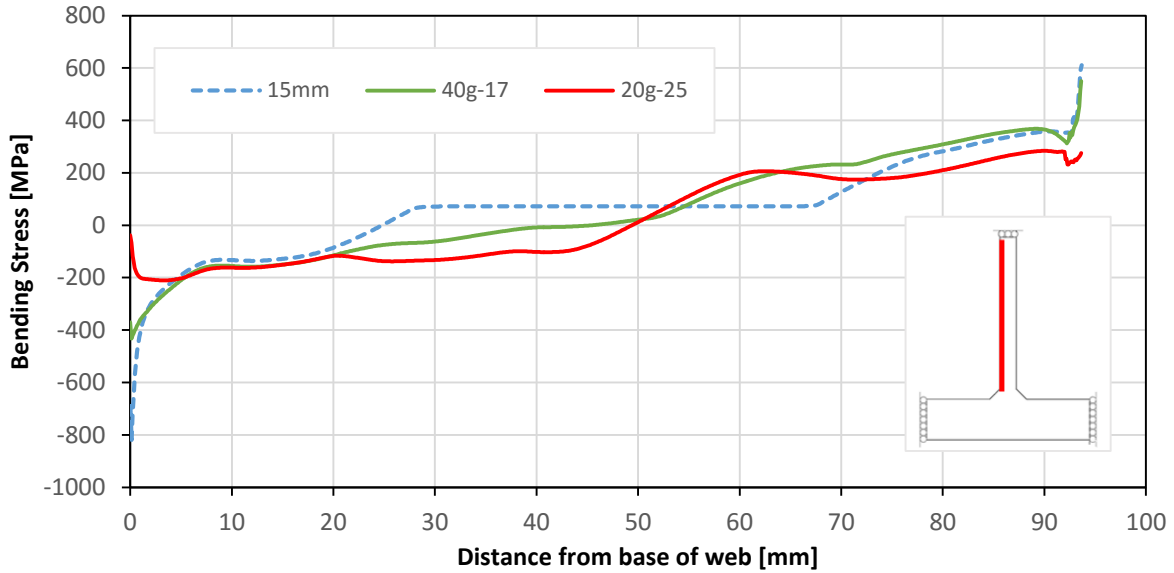
The quasi-static and dynamic impacts had nearly identical plastic strains along the web but plastic strains differ near the point of impact and at the base of the web. The majority of the strains resided within the first 20 millimeters of the base of the web and from the point of impact. The differences in plastic strain are highlighted in Figure 3-7 (a) and (b). Figure 3-8 shows the plastic strain along Path 2 for 15mm, 20g-25, and 40g-17 experiments.



**Figure 3-8: Vertical plastic strain along Path 2 for 15mm, 20g-25, and 40g-17.**

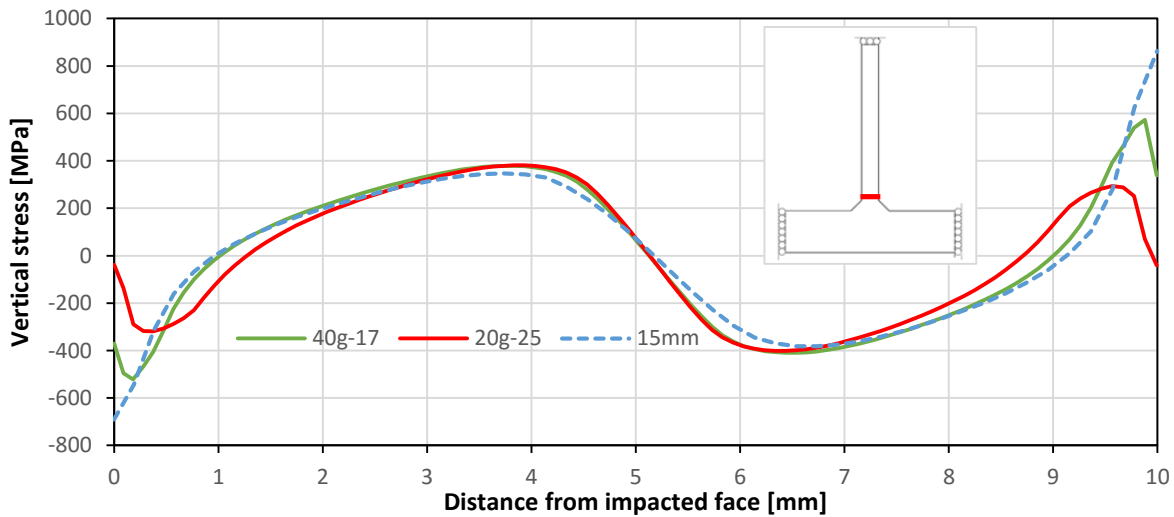
Similar to the plastic strains along Path 1, the plastic strains between loading cases are nearly identical along Path 2. At the surfaces the plastic strains caused by the dynamic experiments were approximately 0.13 and -0.19 as shown in Figure 3-8. These plastic strains were significantly higher than the plastic strains caused by the equivalent quasi-static experiment.

Figure 3-9 shows the bending stress along Path 1 for three experiments with similar deflected shapes. Unlike the vertical plastic strain, the distribution of residual bending stress caused by the quasi-static and dynamic impacts vary significantly along the web. The difference in stress can be attributed to the different strain rates that the three experiments experienced, the high velocity small mass resulted in a lower residual stress than the low velocity large mass dynamic experiment. The quasi-static impact caused -761 MPa of residual stress whereas the dynamic impacts caused -477 MPa and -186 MPa of residual stress for a 17 m/s and 25 m/s impact respectively. The residual stress from the quasi-static impact was higher near the base than the dynamic impacts.



**Figure 3-9: Residual bending stress along Path 1 for 15mm, 20g-25, and 40g-17 experiments.**

Figure 3-10 shows the residual bending stress along Path 2 for 15mm, 20g-25, and 40g-17 impacts. The residual stresses along Path 2 were similar except within 1 to 2 mm from the faces of the section where results diverged. In particular, the dynamic experiments have significantly lower residual stresses than the quasi-static experiment.



**Figure 3-10: Residual bending stress along Path 2 for 15mm, 20g-25, and 40g-17.**

Elastic springback are the cause of this anti-symmetric bending stress distribution, shown in Figure 3-10. Prior to springback, the bending stress distribution resembles classic beam bending

stress distribution. The anti-symmetric bending stress distribution is typical of bending in plates in the weak axis, as shown in [Moshalov & Vorus, 1987] and [Kowalkowski, 2005] for heat cambering and impact damage, respectively. Plastic strains increase towards the outer regions of the web thickness, from 4 to 0 mm and 6 to 10 mm from the impacted face. Proportional magnitudes of springback are associated with the plastic strains.

### 3.2.3 Tee Section Results

Figure 3-11 shows the final displaced shape of the plate girder along Path 1 for various impacts including quasi-static and dynamic experiments. In the following figures, **x** mm indicate that the result from an **x** mm displacement controlled impact and the **yy g- zz** refers to result from an impactor mass of **yy** grams at an impact velocity in **zz** metres per second.

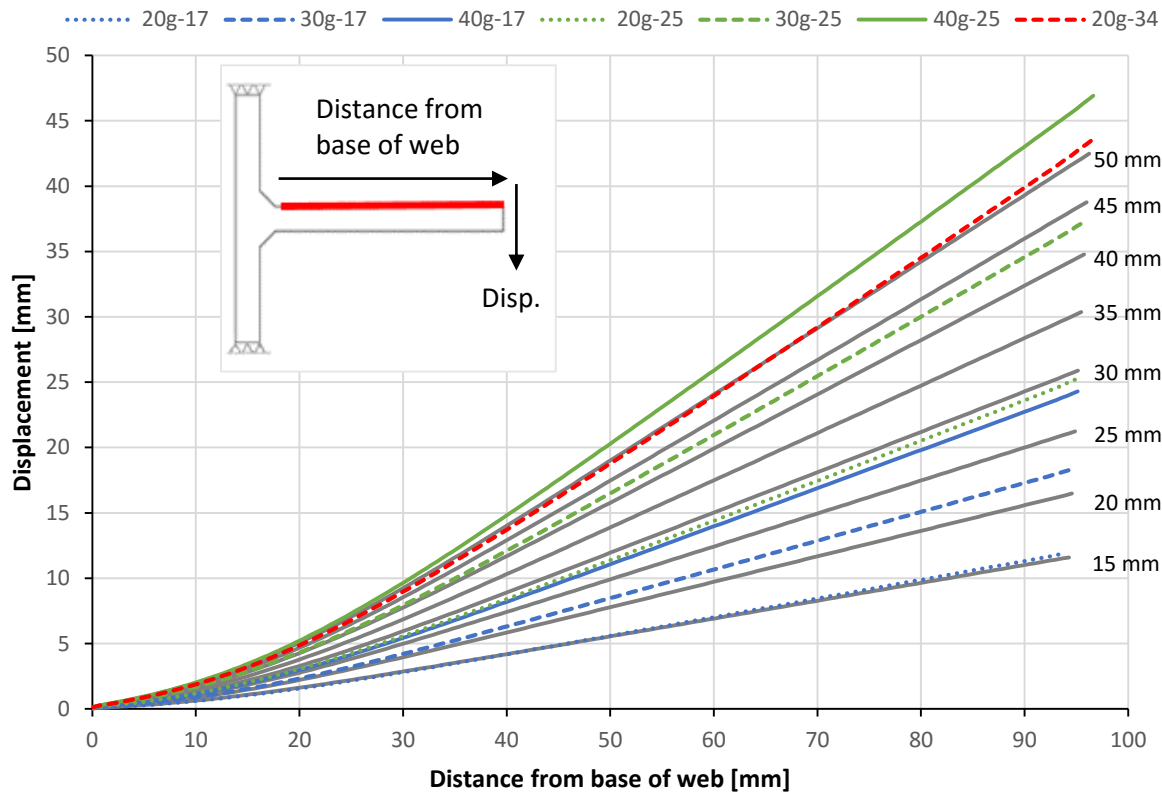


**Figure 3-11: Displacement along Path 1 for quasi-static and dynamic simulations for tee.**

The deflected shape of the 30mm, 20g-25, and 40g-17 experiments have similar shapes with a final displacement within 1 mm of each other at 25.9 mm, 25.3 mm, and 24.3 mm respectively.

Figure 3-12 shows the plastic strain distribution along Path 1 for the three experiments discussed above.

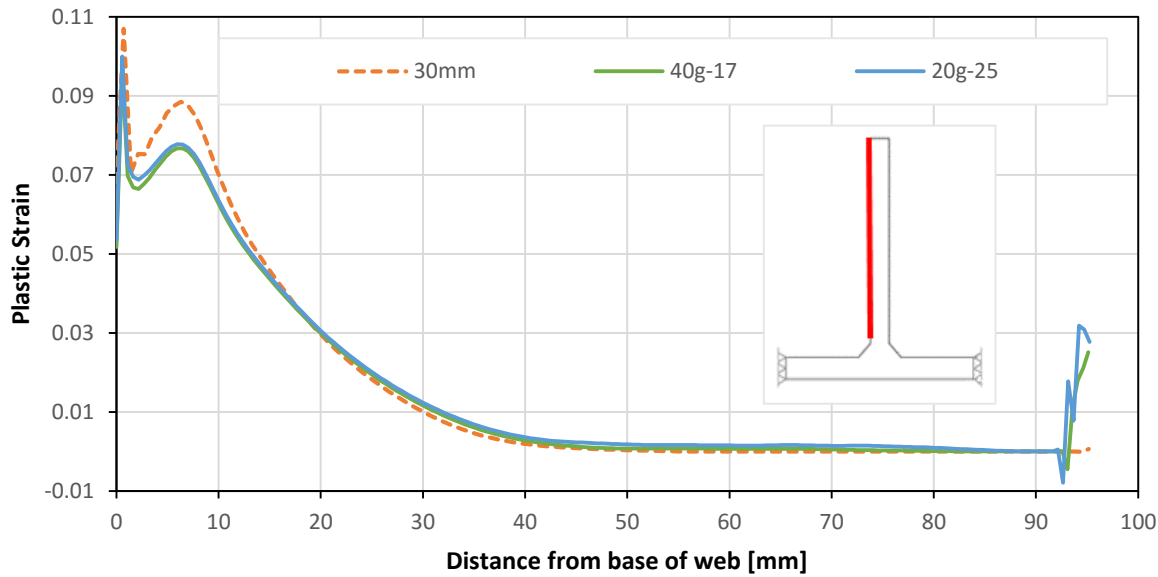
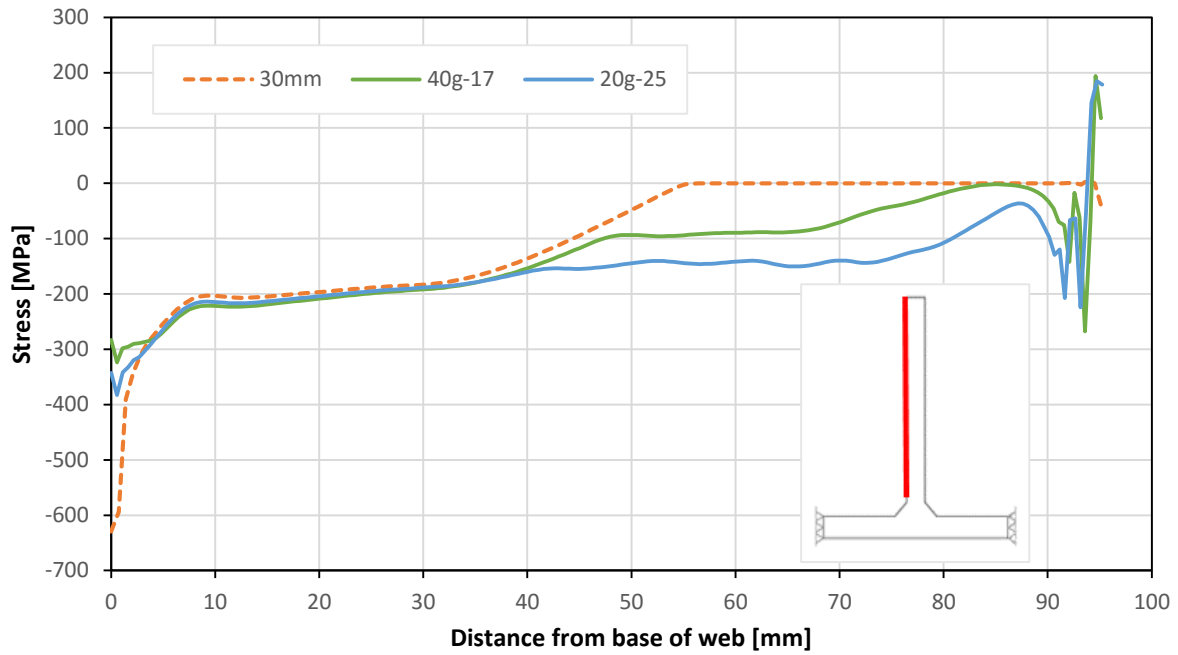


**Figure 3-12: Vertical plastic strain along Path 1 on a tee for 30mm, 40g-17, and 20g-25.**

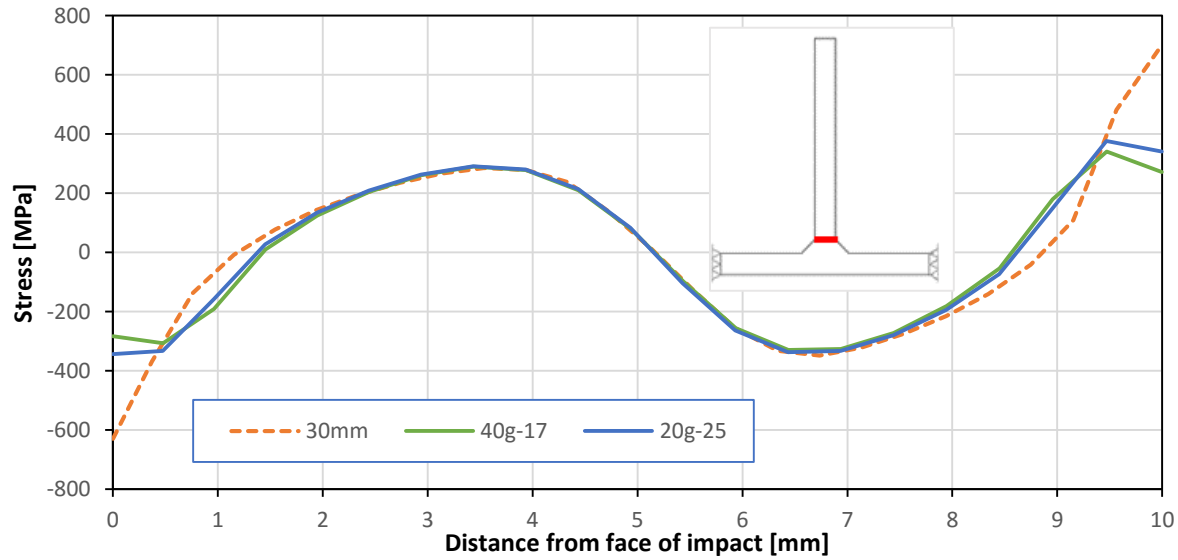
The vertical plastic strain is similar between the quasi-static and dynamic experiments with a similar deflected shape between 20 mm and 90 mm along Path 1 as shown in Figure 3-12. High plastic strains occurred at the point of impact in the dynamic experiments due to local deformations; but the highest strains occurred near the base of the web.

Figure 3-13 shows the residual bending stress along Path 1 for the set of experiments discussed in the previous figure. The plate-girder models show that higher velocity impacts cause lower residual stresses similar to the results with the tee section. The residual stresses shown in Figure 3-13 for 30 mm, 40g-17, and 20g-25 experiments were -629 MPa, -323 MPa, and -283 MPa respectively.

Figure 3-14 shows the residual bending stress distribution for the same models along Path 2. The residual stresses in Figure 3-14 were similar and start diverging within the first two millimeters of each surface.



**Figure 3-13: Residual bending stress along Path 1 on a tee for 30mm, 40g-17, and 20g-25.**



**Figure 3-14: Residual bending stress along Path 2 on a tee for 30mm, 40g-17, and 20g-25.**

### **3.3 Modelling Impact Summary**

Quasi-static loading is commonly used to model the deformed geometry from impact. This method neglects the strain-rate sensitivity and inertial effects from dynamic loading. The quasi-static load cases had higher magnitude residual stresses than the dynamic load cases with similar deformations. The lowest residual stresses occurred in load cases with faster impact velocities. The largest stress concentrations in the sections are located at the faces and approximately 3.5 mm from the faces. The strain distributions were similar regardless of the method of modelling impact. However, significant differences in strain distributions were located at the base of the web and around the point of impact.

The quasi-static and dynamic loading techniques used in this chapter are valid methods of modelling impact. The load cases studied had shown that quasi-static loading resulted in higher residual stresses and strains. Impact damage on bridges is currently evaluated based on the deformed geometry and does not account for the cause of damage. The residual stresses from impact damage near the welds are largely dependent on the strain rates caused by the impact speed. Impacts modelled with quasi-static loading had higher residual stresses near the weld, which can be used for conservative fatigue calculations.

## 4 Modelling Vee Heat Straightening of Plates

In this chapter, modelling techniques for heat straightening are discussed. Heat cambering and heat straightening techniques are similar: both heat straightening and cambering are thermo-mechanical processes that can be modelled using coupled thermo-mechanical models. The thermo-mechanical process can be modelled with sequential and simultaneous thermal-mechanical stress analysis. The advantages and differences between the two methods of analysis are discussed later in this chapter. Heat cambering of undamaged steel plates is modelled and results are validated using existing experimental data. Further studies into the effect of boundary conditions and jacking forces on heat straightening are then conducted using the validated heat cambering model.

### 4.1 Modelling Techniques for Heat Straightening

Modelling heat straightening with FEA requires a temperature-dependent mechanical model with mechanical and heat transfer analysis. Changes in steel temperature causes thermal expansion and changes in material properties. Heat transfer analysis is used to determine the temperature distribution as a function of time from the torch heat flux. Following the heat transfer analysis, the quasi-static stress analysis uses the temperature distribution as a function of time to define the thermal expansion and changes to material properties. Quasi-static stress analysis was used because movements during heat straightening are small and slow. Therefore, inertial effects or strain-rate effects are negligible for heat straightening.

The vee heating process requires an oxyacetylene torch heating steel plates in a meandering motion from the tip to the base of the triangle as shown in Figure 4-1. The heat flux from the moving torch can be modelled as a moving Gaussian distribution of heat flux [Moshaiov & Latorre, 1985]. The estimated parameters used in this method are valid for specific heating conditions (e.g. torch movement speed, the distance from the flame, and ambient temperature). This method was developed for flame cambering in ship construction, where heating occurs in the fabrication shop and environmental conditions can easily be controlled. However during heat straightening, the heating occurs in the field and the heat flux is dependent on the climate and technician experience, in addition to heating conditions in the fabrication

shop. A simplified forced convection model was used to simplify the modelling of heat flux from a moving heat source.

The heat flux for a moving torch was simplified by modelling the heat flux as a source of forced convection sequentially applied to regions of the heated pattern. Figure 4-1 shows the meandering motion of heating a pattern compared to the simplified heating process proposed.

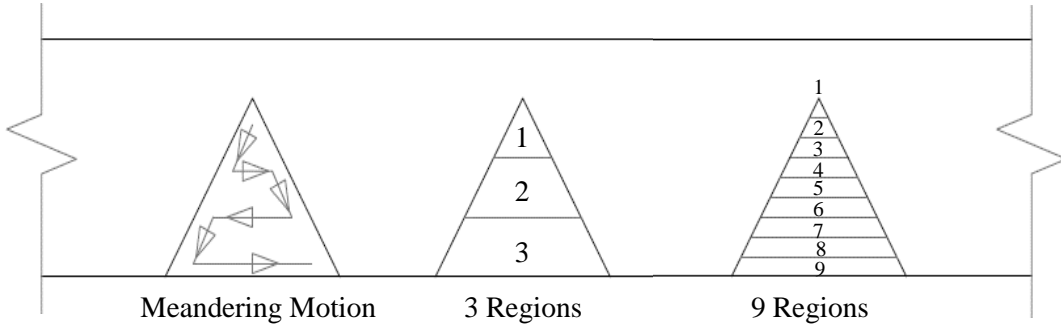


**Figure 4-1: Comparing heat sequence from a meandering torch with the simplified heating sequence of the divided vee patterns.**

The numerated regions shown in Figure 4-1 were sequentially heated using different convection coefficients. The sequential heating of regions was inspired by the strip analogy and residual stress analysis performed in [Nicholls & Weerth, 1972]. While a region was heated, the convection heat transfer coefficient and air temperature at the region were increased to reflect the heat flux and temperature of an oxyacetylene torch, respectively. The heating air temperature was set to 3250 °C, the approximate temperature of an oxyacetylene flame from a torch ranges from 3000 °C to 3500 °C. The heating time for each region was dependent on the desired maximum steel temperature for heat straightening. The forced convection coefficients were estimated by optimization loops in MATLAB based on times required to heat a region to 600 °C. The optimization loops measured the average temperature after the application of heat in each region and changed convection coefficients until the each heated region was subjected to 600 °C. After convection coefficients were established to heat steel to 600 °C, heating times were varied to control the heating temperatures during straightening. The time required to heat steel plates to 600 °C was approximated based on heating times in [Roeder, 1986], [Kowalkowski, 2005], and [Linde Gas, 2014].

Experiments from [Avent, et al., 2000] discussed the effect of heat intensity and time on heat straightening and concluded that there were no significant changes in plastic rotation if the plates were heated at a reasonable rate. A reasonable heating time for a small plate for heat straightening was determined by evaluating small plate heat straightening experiments in [Roeder, 1986; Kowalkowski, 2005; Linde Gas, 2014]. The heating and cooling rates are determined by approximating convection and radiation coefficients for heat transfer, as discussed in Section 4.2.

## 4.2 Material Properties for Thermal and Mechanical Analysis

Modelling heat straightening requires a thermal-stress analysis and a heat transfer analysis. Heat straightening can be modelled as a sequential or simultaneous thermal-stress analysis, discussed in Section 4.3. The heat transfer analysis is dependent on thermal material parameters as discussed in Section 4.2.1. The changes in temperature cause thermal expansion and changes in material properties, as discussed in Section 4.2.2.

### 4.2.1 Thermal Material Parameters

Table 4-1 shows the functions used to determine coefficients for linear thermal expansion, thermal conductivity, and specific heat of steel relative to temperature according to [European Committee for Standardisation, 2005].

**Table 4-1: Functions for thermal material properties [European Committee for Standardisation, 2005].**

Coefficients	Equations
Linear Thermal Expansion	$\alpha[\text{ }] = \begin{cases} 1.2 \times 10^{-5} + 0.8 \times 10^{-8}T, & 20^\circ\text{C} < T < 750^\circ\text{C} \\ 1.8 \times 10^{-5}, & 750^\circ\text{C} < T < 860^\circ\text{C} \end{cases}$ (45)
Thermal Conductivity	$k \left[ \frac{\text{W}}{\text{K}} \right] = 54 - 3.33 \times 10^{-2}T, \quad 20^\circ\text{C} < T < 800^\circ\text{C}$ (46)
Specific Heat of Steel	$c^a \left[ \frac{\text{J}}{\text{kg K}} \right] = \begin{cases} 425 + 7.73 \times 10^{-1}T - 1.67 \times 10^{-3}T^2, & 20^\circ\text{C} \leq T < 600^\circ\text{C} \\ + 2.22 \times 10^{-6}T^3 \\ 666 + \frac{13002}{738 - T}, & 600^\circ\text{C} \leq T < 735^\circ\text{C} \end{cases}$ (47)

$\alpha$ ,  $k$ , and  $C^a$  are the coefficients of linear thermal expansion, thermal conductivity, and specific heat of steel, respectively. Equation (45) shows that the coefficient of linear thermal expansion increases until 750 °C approximately, where molecular phase changes occur. Thermal conductivity decreases linearly as it approaches 800 °C. The specific heat of steel gradually increases until 600°C, where the specific heat significantly increases as it approaches 735 °C. The majority of heat straightening operations for non-tempered and quenched steel occur below 700 °C to avoid molecular phase changes.

The heat transfer from convection and radiation is dependent on the surface condition of the steel and properties of the surrounding air. The equations for heat transfer are described in Section 2.6.7 and the coefficients used are documented below. Natural convection and forced convection of air has a convection heat-transfer coefficient of 5 to 25 W/m<sup>2</sup>K and 10 to 100 W/m<sup>2</sup>K, respectively [Holman, 2002]. Forced air convection coefficients used to model heat flux from the torch were approximated such that the steel plates were heated to temperatures within reasonable times. Reasonable times for heating were based on heating times for experiments noted in literature [Roeder, 1986; Kowalkowski, 2005; Linde Gas, 2014]. The cooling was modelled as natural convection at 7.9 W/m<sup>2</sup>K. The emissivity of mild steel plates range from 0.3 to 0.8 depending on the quality of the steel surface and temperature [Sadiq, et al., 2013]. For the heat straightening model, the emissivity of steel used was 0.3 for the heat straightening model. Radiation heat flux was mainly used as another source of cooling.

#### 4.2.2 Mechanical Parameters

The steel was modelled using an isotropic temperature-dependent constitutive model. The reductions in modulus of elasticity relative to temperature for mild steel were defined in the European standards as shown in Figure 4-2.

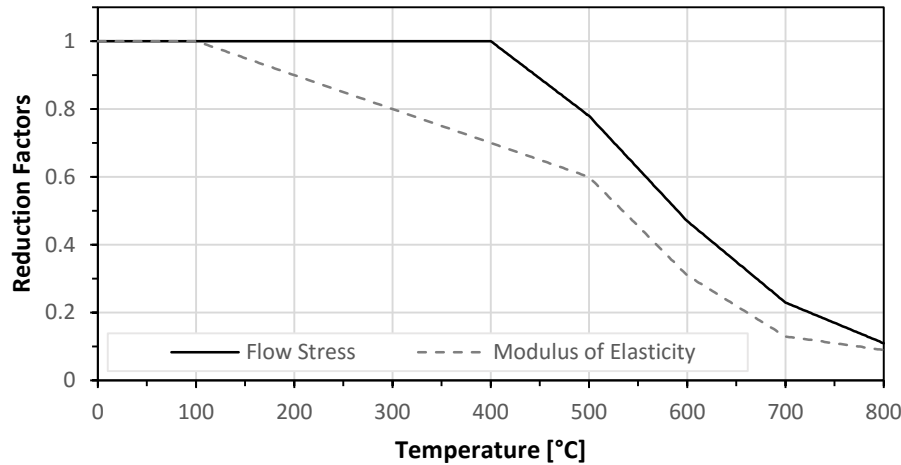


**Figure 4-2: Flow stress and modulus of elasticity reduction factors relative to temperature [European Committee for Standardisation, 2005].**

These parameters are important in the heat straightening mechanism. The modulus of elasticity and flow stress do not significantly change until the metal temperatures exceeds 100 °C and 400 °C, respectively. Heat straightening can be performed with heating temperatures as low as 100 °C, but results become more substantial when heating temperatures exceed 400 °C because the flow stress begins to decrease as well.

The modulus of elasticity, Poisson's ratio, and steel density used in the model are shown in Table 3-1. The flow stress function was defined in ABAQUS with a table of flow stress and equivalent plastic strain. Figure 4-3 is the flow stress versus equivalent plastic strain used to define the plastic response of CSA 350w and ASTM A36 steel.

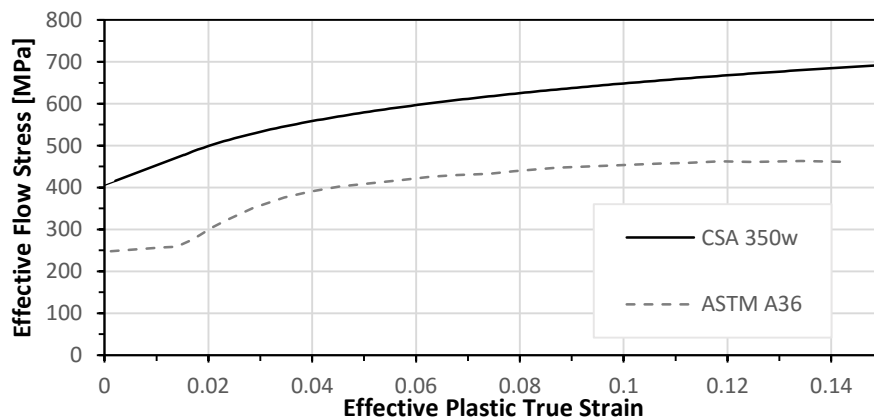


**Figure 4-3: Flow stress versus effective plastic true strain of CSA 350w [Arasaratnam, et al., 2011] and ASTM A36 steel [Brokenbrough & Johnson, 1994].**

The flow stress versus effective plastic true strain in Figure 4-3 was created from uniaxial tension data for CSA 350W and ASTM A36 steel from [Arasaratnam, et al., 2011] and [Brokenbrough & Johnson, 1994], respectively. The ASTM A36 steel data was pertinent to modelling heat straightening for undamaged steel plates. The CSA 350W steel data were also important for modelling the impact and heat straightening for the material properties of a Canadian steel bridge in Section 5.2.1.

### **4.3 Simultaneous and Sequential Coupled Thermal-Stress Analysis for Heat Straightening**

The heat straightening can be modelled using implicit sequential and simultaneous coupled thermal-stress analyses. Simultaneous thermal-stress analysis in FEA uses coupled temperature-displacement elements, where temperature is calculated in addition to displacement at every time increment simultaneously. This analysis is used in cases where stress and temperature distribution are interdependent. Temperature-Displacement Octahedral (C3D8T) elements are used to discretize the plate for simultaneous thermal-stress analysis.

Alternatively, sequential thermal-stress analysis contains a heat transfer analysis followed by a quasi-static stress analyses. The heat transfer analysis is used to calculate the temperature distribution as the torch heats the pattern. The temperature distribution relative to time is imported into the stress analysis; the elevated temperatures change the material properties of steel and create forces via restrained thermal expansion. This analysis is used in cases where temperature is not significantly affected by the stress analysis. Sequential thermal-stress analysis requires that steel members are discretized into three-dimensional heat transfer (DC3D8) and reduced-integration stress elements (C3D8R) for implicit heat-transfer and quasi-static stress analyses, respectively. Due diligence is required to ensure that the time steps in the quasi-static analysis are sufficiently small to capture the nuances in the temperature changes from heat transfer analysis.

Simultaneous and sequential thermal-stress analyses are used to model heat cambering on a 6x100x610 mm plate discretized by 1.5 mm wide elements. The plates are subjected to a  $\frac{3}{4}$  depth 60° vee heats with fixed-ends and a 6.5 kN jacking force at the base of the vee. Compared

to sequential thermal-stress analysis, simultaneous thermal-stress analysis required significantly longer computational times. There were no significant differences in displacement or temperature between the two analyses. Figure 4-4 shows Von Mises stress for plates models heat cambered with simultaneous and sequential thermal-stress analysis.

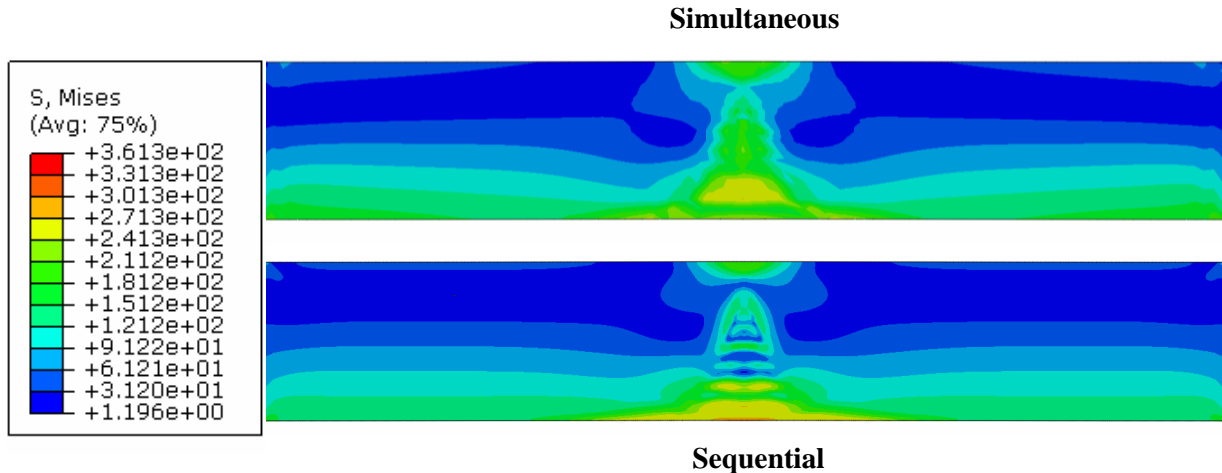


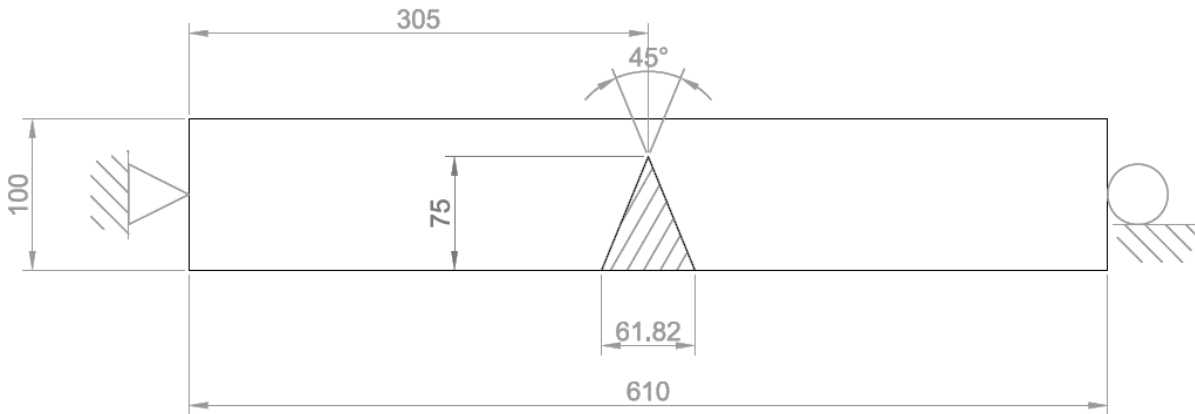
**Figure 4-4: Von Mises stress distribution after simultaneous and sequential thermal-stress analysis.**

Differences between the two thermal-stress analyses are significant within the heated region for residual Von Mises stress. The simultaneous thermal-stress analysis resulted in a stress distribution consistent with [Roeder, 1986], where the highest stress is located in the middle of the plate. The sequential thermal-stress analysis had a stress distribution where residual stresses were unusually lower between heated regions. Sequential thermo-mechanical analysis is a valid method of modelling heat cambering; differences existed in the residual stress distributions. However, the differences in residual stress did not affect the changes in geometry from heat straightening.

#### 4.4 Validation of the Heat Straightening Model

To validate the heat straightening modelling techniques and parameters described above, a model of an undamaged plate subjected to heat cambering is compared with experimental data. The experimental data from [Avent, et al., 2000] contained average plastic rotations caused by heat cambering at a range of temperatures from 400 °C to 788 °C for ¾ depth vee heats at

different vee angles. Heat straightening was modelled using an implicit coupled sequential thermal-stress analysis. Undamaged A36 plates were flame cambered using vee-heat straightening techniques. The undamaged plates were 6x100 mm wide and supported 610 mm apart as shown in Figure 4-5.



NOTE: ALL DIMENSIONS IN MM UNLESS NOTED OTHERWISE.

**Figure 4-5: Tested support conditions for 6x100mm wide plates during heat straightening [Avent, et al., 2000].**

This section will discuss heat straightening results where the plates were subjected to  $\frac{3}{4}$  depth 45° vee heat with jacking forces applied against the base of the heated triangular section. A 6.5 kN jacking force was applied at the plate midspan to create the flexural jacking ratio of 0.16 during heat straightening. The 45° vee heating pattern was located at the midspan of the plate, 305 mm from the ends. The  $\frac{3}{4}$  depth vee pattern was 61.82 mm wide and 75 mm tall. Out-of-plane deformation is restrained at the top and bottom sides of the plate.

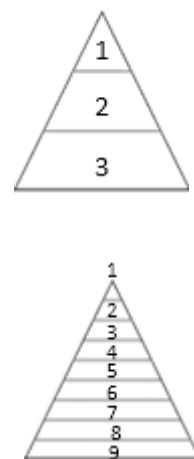
The results were compared with experimental data using vee heat straightening techniques on undamaged simply-supported plates. The meandering torch heat flux was modelled using the simplified sequential heated region method discussed earlier. The vee pattern was divided into 3 and 9 regions. Table 4-2 shows the convection coefficient used in each region and the time required to heat each region to the maximum heating temperature.

The region numbers listed in Table 4-2 match the enumerated regions found in Figure 4-1. These forced convection coefficients were approximated and based on the initial assumption that it required 5 minutes to heat the entire pattern on the plate to 600 °C. The forced convection coefficient is affected by heating area, perimeter of the heating region and the thermal energy

from previously heated sections. After the convection coefficients were established for 600 °C, the heating time at each region was progressively lowered to meet lower maximum heating temperatures. Figure 4-6 shows the maximum heating temperature, residual Von Mises stress and maximum principal plastic strain distributions after vee heat straightening at 600 °C.

**Table 4-2: Convection coefficients and heating times for each region.**

Region Number	Convection Coefficient [mW/mm <sup>2</sup> K]	Region Heating Time [s] for Maximum Heating Temperature				
		600 °C	550 °C	500 °C	450 °C	400 °C
<b>3 Regions</b>						
1	0.439	105.7	69.0	46.0	30.0	20.0
2	0.179	105.7	80.0	60.0	49.0	33.0
3	0.082	105.7	63.0	51.0	41.0	35.0
<b>9 Regions</b>						
1	3.038	3.5	1.9	1.3	0.8	0.5
2	1.259	17.0	12.0	8.0	5.0	3.0
3	0.828	26.0	17.0	12.5	8.5	6.0
4	0.631	30.0	23.0	15.0	10.0	7.5
5	0.515	34.0	27.0	17.0	14.0	10.0
6	0.424	40.0	27.0	26.0	19.0	13.0
7	0.334	35.0	30.0	20.0	16.0	13.0
8	0.242	40.0	19.0	20.0	10.0	15.0
9	0.155	45.5	4.0	6.0	5.0	5.0



The division of heated regions is marked by the lower temperatures in the heat pattern, made especially clear in the temperature distribution for 3 regions. However, this method of sequentially heating regions does not provide a smooth heat progression. Increasing the number of regions improves the heat progression during the heating process. The vee heated with 3 regions was subjected to significantly more heat around the perimeter of the pattern. The Von Mises residual stresses shown in Figure 4-6 are lowest between boundaries of heated regions and the residual stress distribution. The number of heated regions affected the magnitude and distribution of maximum principal plastic strains. The largest residual Von Mises stress and maximum principal plastic strain were approximately 282 MPa and 0.01, respectively, and occurred in the plate with 3 heated regions.

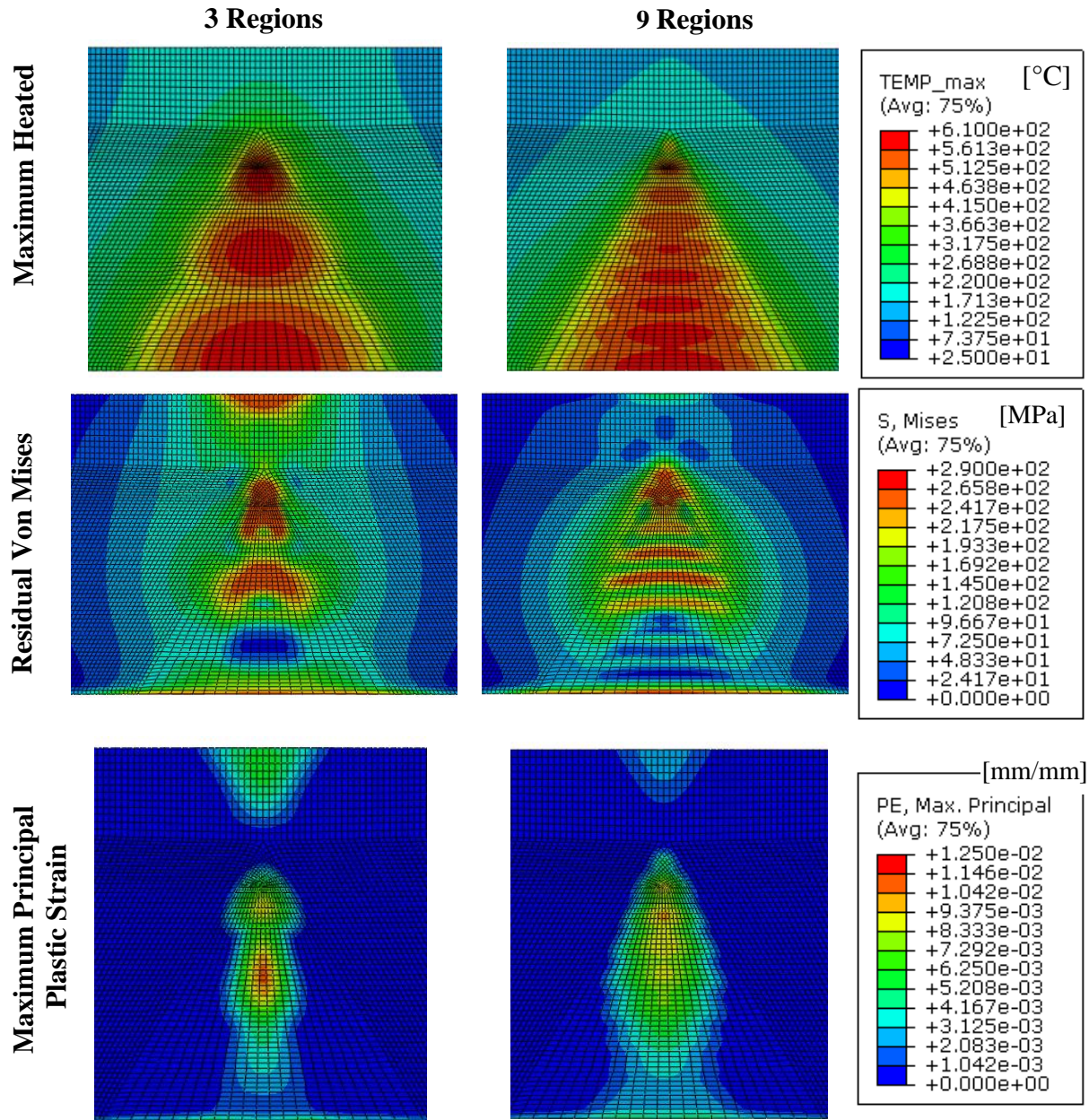


**Figure 4-6: Maximum heating temperature, residual Von Mises stresses, and maximum principal plastic strains for 3 and 9 heated regions.**

The differences in results between 3 and 9 regions occur mainly in the residual stress and strain distributions. However, the displacements of the plates measured as plastic rotations were similar for both 3 and 9 regions. The plastic rotations in FEA was calculated by averaging the displacements for the nodes in the middle of the plate. The finite element heat straightening results were compared to experimental plastic rotations over a range of temperatures. Figure 4-7

shows the plastic rotations caused by the heated regions and experimental data between 399 °C and 621 °C.

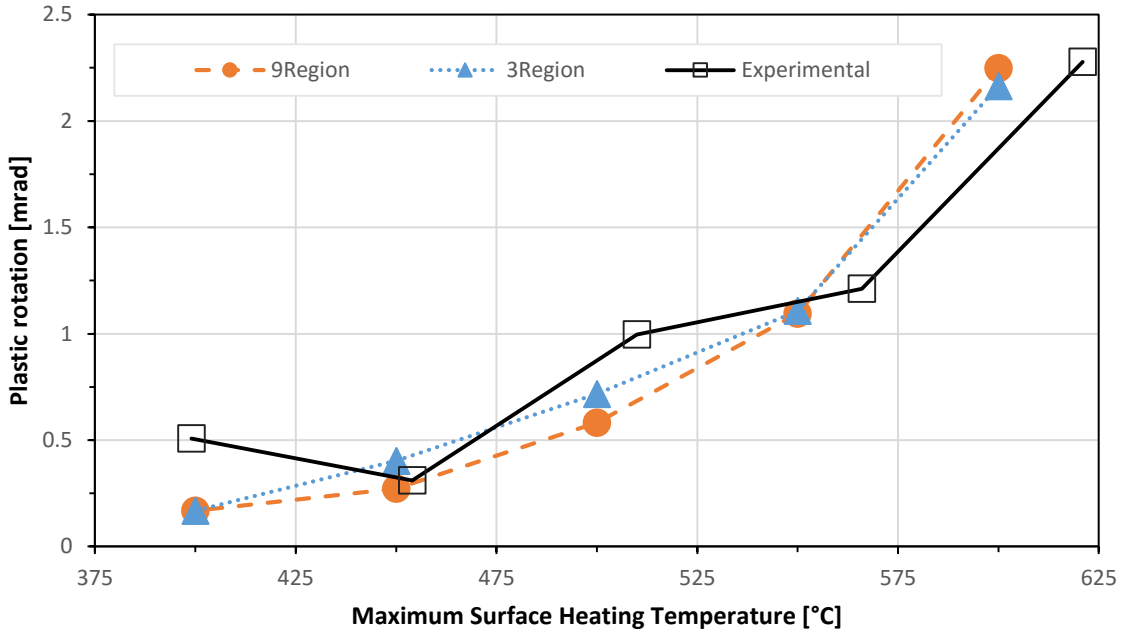


**Figure 4-7: Plastic rotation versus maximum heating temperature for simply-supported plate.**

The heat straightening FEA model results generally had lower plastic rotations compared to the experimental results except over 550 °C, where the plastic rotations were higher than experimental results. The heat straightening FEA model shows a consistent non-linear improvement in plastic rotation as a result of increasing the maximum heating temperature. The experimental data could be subject to a 50 °C error from using technicians' judgement [Mukai & Avent, 1998]; the model of the heated plates cooled over 50 °C within the first few seconds. The existing data in the paper was an average plastic rotation from multiple technicians and heat cycles. The differences between finite element results and experimental data for plastic rotations were consistently lower than a 50 °C error at temperatures larger than 450 °C.

#### 4.5 Heat Straightening Model with Different Boundary Conditions

It is recommended that jacking forces should not create a jacking moment exceeding 50% of the plastic moment as the jacking ratio, as described in [Mukai & Avent, 1998]. This

recommendation is based on the reductions in yield strength as the temperature approaches 650°C; the yield strength of steel at 650°C approaches approximately 50% of its yield strength at room temperature. The jacking moment is affected by the supporting boundary conditions and jacking forces. The plastic moment is a function of plastic modulus and yield strength. The heat straightening model developed for the undamaged plate will be evaluated for different boundary conditions.

Changing boundary conditions significantly affects the plastic rotations or displacements caused by heat straightening. Simply-supported plates and plates with fixed-ends were subjected to multiple cycles of heat straightening with jacking loads as shown in Figure 4-8.

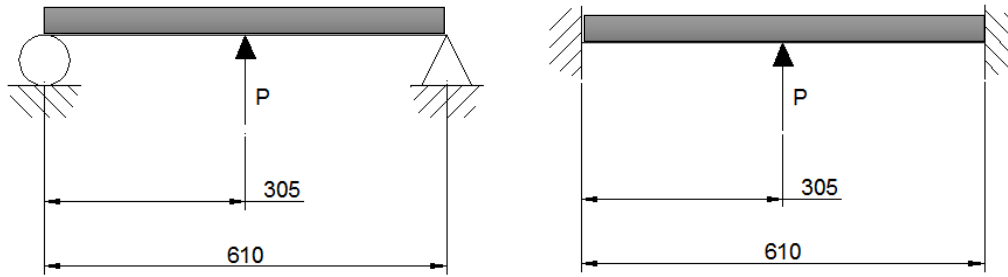


**Figure 4-8: Jacking load,  $P$ , locations for simply supported and fixed 6 x 100 x 610 mm long plates.**

The plates were subjected to seven cycles of 45° vee heat straightening. Plates SS15 and SS30 denoted simply-supported plates with 15 MPa (7.25 kN) and 30 MPa (15.5 kN) jacking loads, respectively. Plates Fixed30 and Fixed60 were fixed at both ends and subjected to 30 MPa (15.5 kN) and 60 MPa (31.0 kN) jacking loads, respectively. Plates SS30 and Fixed60 had analytically identical jacking moments applied. Figure 4-9 shows the displacements versus time for fixed ends and simply supported plates with different jacking forces subjected to multiple cycles of heat straightening. Displacements in Figure 4-9 were measured at the midpoint of the plates, where jacking forces were also applied. Plates SS30 and Fixed60 had similar changes in deformations at each vee heat cycle. Plates with fixed ends that were heat cambered using jacking loads identical to simply-supported plates were significantly less effective. Changes in displacement from heat straightening had diminished after every subsequent heat cycle.

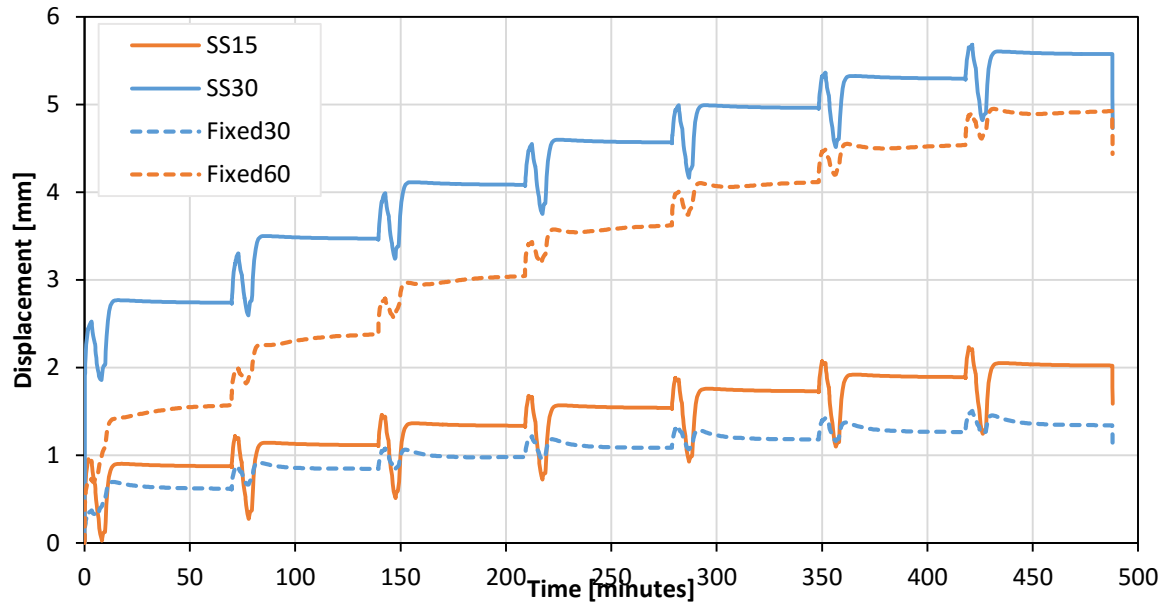


**Figure 4-9: Displacements versus time for fixed-ends and simply-supported plates with different jacking forces.**

#### 4.6 Multiple Cycles of Heat Straightening for Cantilever Plates

Multiple cycles of heat straightening was significantly more effective for cantilever plates. The cantilever plate was 6x100x610 mm long and subjected to a 5 MPa (5 kN) jacking force at the free end, as shown in Figure 4-10.

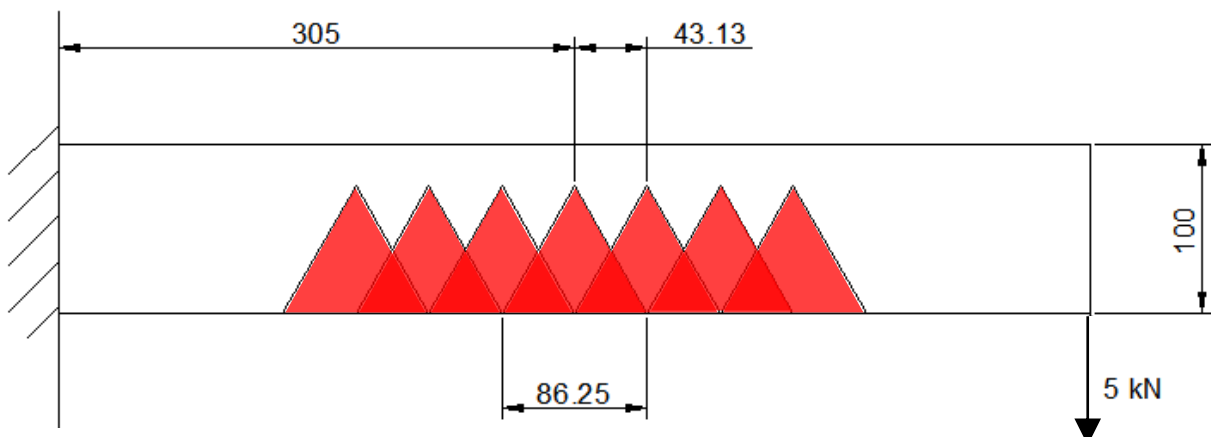


**Figure 4-10: Cantilever plate subjected to seven overlapping vee heats and 5 kN force.**

The plate was cambered using seven different overlapping heat patterns shown in red in Figure 4-10. Figure 4-11 shows free-end cantilever displacement and change in displacement at the end of each heat cycle.

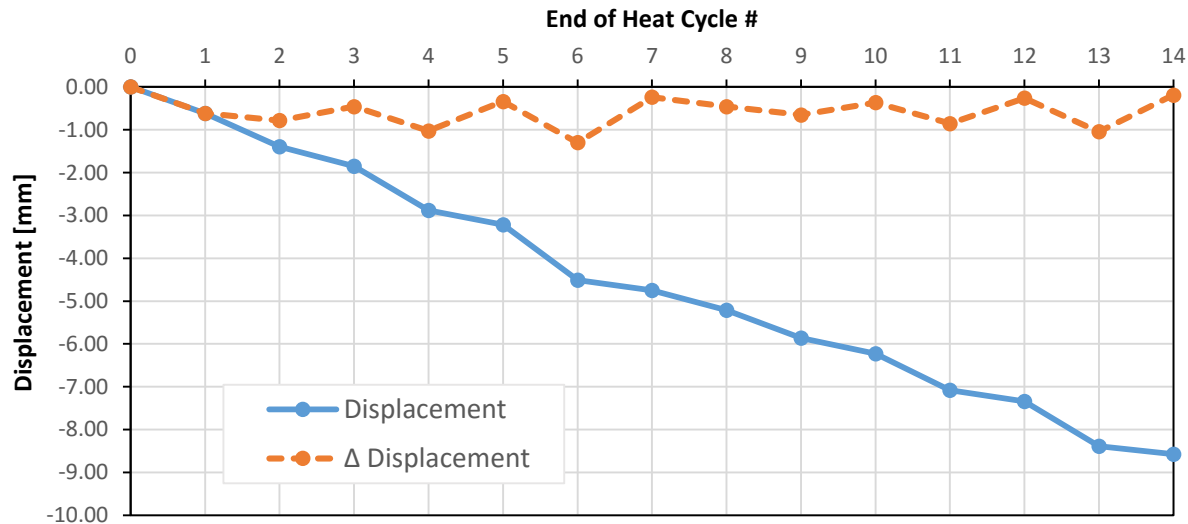


**Figure 4-11: Displacements after each heat cycle for a cantilevered A36 plate.**

The displacement at the cantilever end of the plate after seven and fourteen cycles of heat straightening for A36 steel were 4.75 mm and 8.58 mm, respectively. The increase in displacement from heat straightening was relatively consistent. The displacements are directly related to the bending stresses caused by the jacking forces. Heat cycles 3, 5, 7, 10, 12, and 14 caused lower displacements and the heat patterns were closer to the free end. Heat patterns closer to the free end were subjected to lower bending stresses. The diminishing effectiveness from repetitively heating the same pattern did not change with the cantilevering plate. However, heat cycling seven overlapping patterns instead of repetitively heating a single pattern was more effective. Figure 4-12 shows residual Von Mises stress and maximum principal plastic strains for cantilevering A36 steel plate.

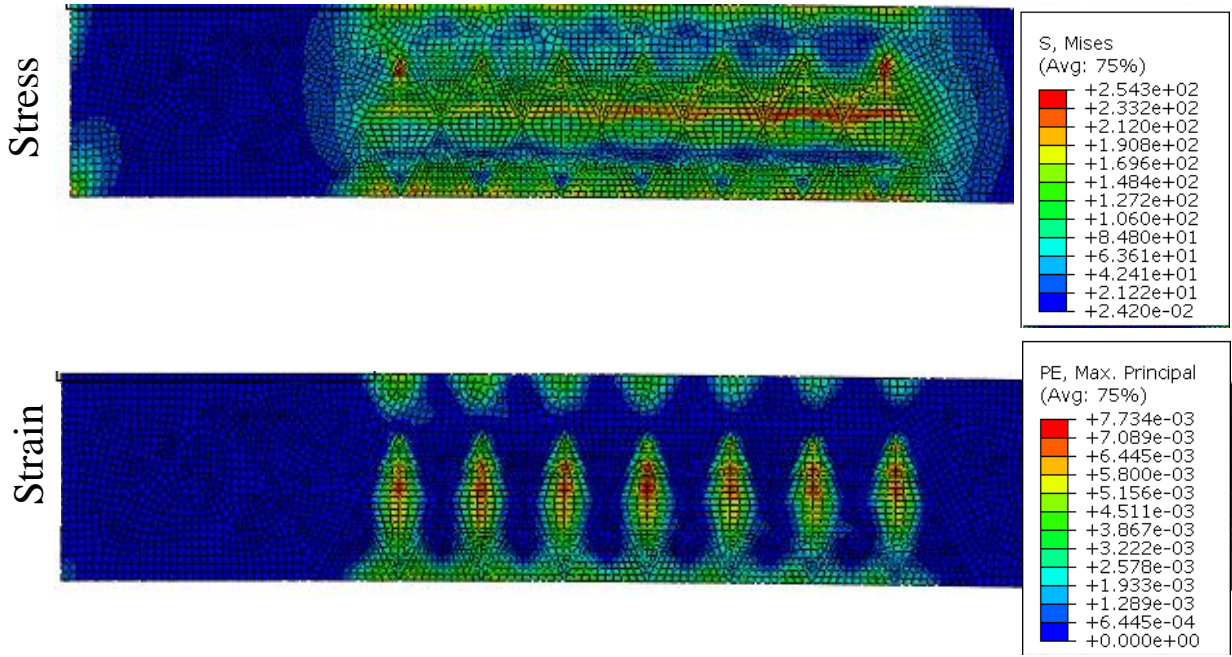


**Figure 4-12: Von Mises residual stress (MPa) and maximum principal plastic strain after heat cambering of cantilever plate.**

In Figure 4-12, the fixed and free ends of the cantilever are located on the left and right, respectively. The seven overlapping patterns did not interfere with each other as shown in the maximum principal plastic strain from Figure 4-12. This strain distribution shows that overlapping heating patterns may be placed closer together.

#### 4.7 Modelling Heat Straightening Summary

Modelling techniques for heat straightening were discussed and results were compared against existing experimental data for heat cambering of undamaged steel plates. Heat straightening is a thermo-mechanical process and can be modelled using simultaneous or sequential thermal-stress analysis. Changes in geometry due to heat straightening are affected by boundary conditions, jacking forces, and material properties.

The undamaged plates were bent using vee heat straightening. Vee heating requires that the steel is progressively heated in a triangular pattern. The moving heat flux associated with the motion of the torch can be simplified by dividing the pattern into sequentially heated regions. The application of heat is the main source of strains and changes in material properties associated

with the thermo-mechanical process. Dividing the heated pattern into 3 and 9 regions resulted in similar plastic rotations but larger differences occurred in the distribution of stresses and strains.

Heat straightening can be modelled using FEA with either sequential or simultaneous thermal-stress analysis. Simultaneous thermal-stress analysis can be significantly slower compared to sequential thermal-stress analysis. Careful consideration of key time steps is required for sequential thermal-stress analysis to properly model the changes in temperature associated with the heating process. Residual stress results from sequential thermal-stress analysis differ from simultaneous thermal-stress analysis. If the goal of the heat straightening analysis is to assess residual stresses simultaneous thermal-stress analysis is recommended. However, applying sequential thermal-stress analysis is easier and quicker resulting in similar changes in geometry.

Heat transfer analysis required the use of thermal material parameters defined for mild steel and estimated heat transfer coefficients. These general material parameters and estimated heat transfer coefficients may not provide an accurate model for heat transfer. However, the resulting temperature changes were sufficient for modelling the heat straightening of a plate.

Heat straightening is dependent on boundary conditions and material properties. Improperly defined boundary conditions inhibit the changes in geometry due to heat straightening. The primary mechanism for heat straightening is controlled thermal expansion of steel. The most effective vee heat straightening models had boundary conditions where steel was restrained from longitudinal expansion, but free to contract and rotate at the supports. Models of cantilevering plates subjected to multiple cycles of heat straightening had a linear changes in plastic rotation. Simply-supported plates and plates with fixed ends required different magnitudes jacking forces to achieve equivalent jacking ratios and plastic rotations. Plates subjected to multiple cycles of vee heat straightening had diminishing plastic rotations regardless of support conditions. However, heat straightening with multiple heat patterns is more effective.

## **5 Application of Models to a Full-Scale Bridge**

Modelling the heat straightening of impact-damaged bridge girders requires a combination of techniques to simulate the impact and subsequent heat straightening, as discussed in Chapters 3 and 4. The current chapter contains a description of the workflow and parameters required to model a full-scale bridge structure subjected to impact followed by heat straightening. The workflow was applied to model an impact and heat straightening on a hypothetical bridge based on a Canadian Institute of Steel Construction (CISC) design example. The effects of heat straightening were investigated by observing the residual stress, strain, and displacements after impact and heat straightening.

### **5.1 Finite Element Analysis Workflow from Impact to Heat Straightening**

The finite element analysis (FEA) workflow includes a description of the processes and parameters required to model the bridge damage from impact and member restoration from heat straightening. The workflow is divided into impact and heat straightening modules as shown in Figure 5-1. The impact modelling process requires iterations of impact and springback analysis. Heat straightening is modelled with heat transfer analysis followed by quasi-static analysis.

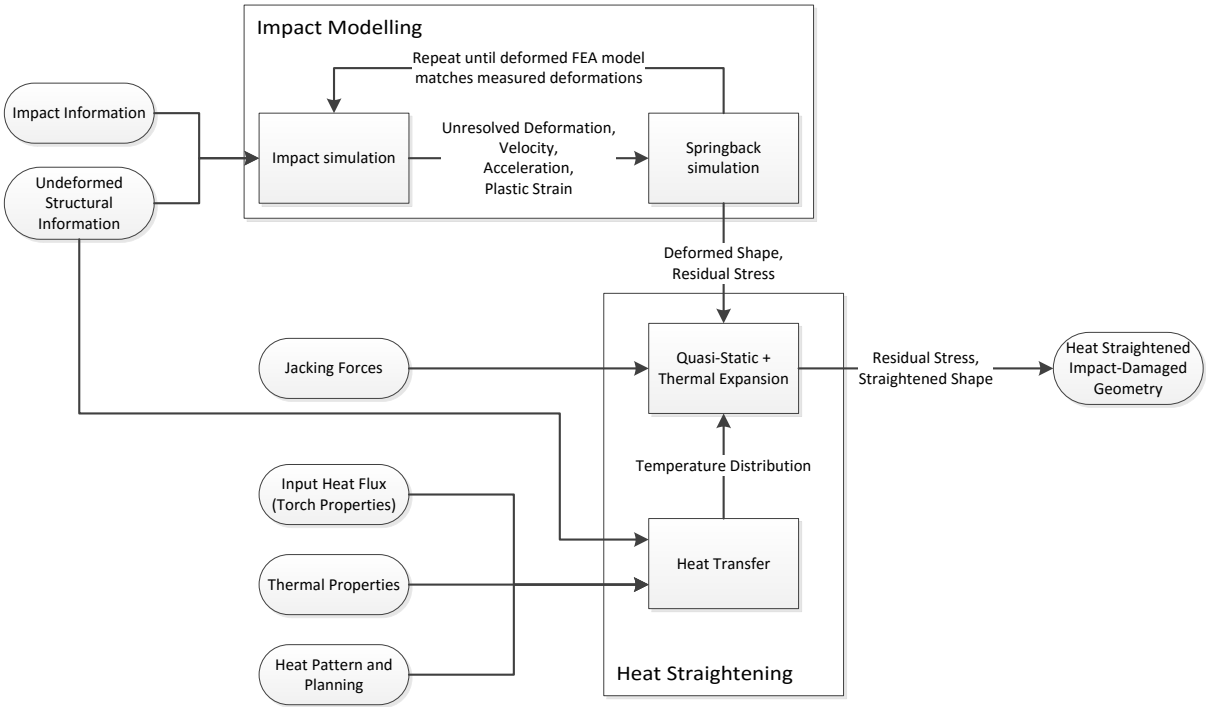


**Figure 5-1: Workflow for finite element modelling of impact and heat straightening for a structure.**

### 5.1.1 Impact Modelling

The impact modelling process requires iterations of implicit or dynamic impact analysis and quasi-static springback analysis as shown in Figure 5-1. This process requires two sets of information: undeformed structural information and impact information. The undeformed structural information describes mechanical material parameters, the undeformed geometry, and the support conditions for the structure. The impact information includes the impactor geometry, mass, velocity, and the deformed structure geometry after impact. Often some impact information such as impactor mass, velocity, or geometry is unknown. Assumptions for these parameters are used for the initial iteration. Additional iterations are performed until the deformations in the model match field measurements of the deformed geometry. Temperature-dependent parameters are ignored for the impact and springback simulations because heat generation due to plastic deformation is negligible. The dynamic impact analysis is limited to modelling deformations, while the structure is in contact with the impactor. The remainder of the impact is modelled with quasi-static springback analysis.

The quasi-static springback process models the elastic rebound of the structure after impact. A quasi-static analysis for springback requires lower computation time compared to dynamic analysis [Dassault Systèmes, 2011]. Velocity and acceleration from vibrations are removed through artificial damping. Contact calculations are excluded to expedite the analysis.

### 5.1.2 Heat Straightening Modelling

Heat straightening is modelled as a quasi-static sequential coupled thermal-stress analysis, requiring heat transfer analysis followed by quasi-static analysis. The separated heat transfer and quasi-static analysis allows for expedited iterations of changes in heating temperatures, jacking forces, support conditions, and heating plans. The heat transfer analysis provides temperature changes from the heating and cooling cycles with one or multiple oxyacetylene torches. The time-dependent temperature distributions from heating are imported into the quasi-static heat straightening analysis. Incremental temperature changes, within the quasi-static heat straightening analysis, cause reductions in yield strength and increases in thermal strains. The combination of reduced yield strength and increased thermal strains in patterns causes controlled plastic deformations.

The heat transfer analysis is used to create time-dependent temperature distributions from cycles of heating and cooling. This analysis calculates the thermal energy balance from the input heat flux (oxyacetylene torch properties), thermal material properties, and a heating plan. The input heat flux distribution is simplified into sequentially heated strips as discussed and validated in Chapter 4. The heat transfer analysis requires the following thermal material properties to be defined: thermal conductivity of steel, specific heat of steel, convective heat transfer coefficient, and emissivity for radiation heat transfer. The heating plan specifies the heating patterns, the heating temperature, and the heat pattern locations.

The quasi-static heat straightening analysis is performed with the imported residual stress and deformed geometry from the impact modelling. Jacking forces are applied at this step to create additional constraints to increase the plastic rotations from heat straightening. The time-dependent temperature distributions, created from the heat transfer analysis, are applied onto the impact-damaged model. Changes in modulus of elasticity and reductions yield strength, and

increasing coefficients of linear thermal expansion from elevated temperatures are added to the material model in this step. The combined heat-transfer and quasi-static analysis models heat straightening on the impact-damaged structure. This process is repeated until the deformed structure is remediated.

## 5.2 Impact and Heat Straightening of bridge

The workflow described in the previous section was implemented for modelling impact damage and heat straightening of a full-scale steel-concrete composite highway bridge. This section includes a description of the bridge modelled and the results including stresses, strains, and displacements.

### 5.2.1 Bridge Model

The bridge model was based on a straight I-girder bridge design example developed previously by the CISC [Canadian Institution of Steel Construction, 2011]. The original bridge design was a continuous three span bridge, with spans of 43 m, 53 m, and 43 m. The bridge end supports were modelled as fixed supports free for longitudinal expansion. Only a single 43 m span was modelled and the impact was applied halfway along the span. The top flanges were restrained from any movement because the concrete slab prevents large lateral deformations due to impact. The plate girders, lateral bracing, and plate stiffeners were modelled as CSA 350W steel. The impactor was modelled as a linear elastic steel so the energy will be dissipated through the plate girder. The bridge cross-section consisted of four plate-girders and a 235 mm thick concrete slab with 600 mm overhangs as shown in Figure 5-2.

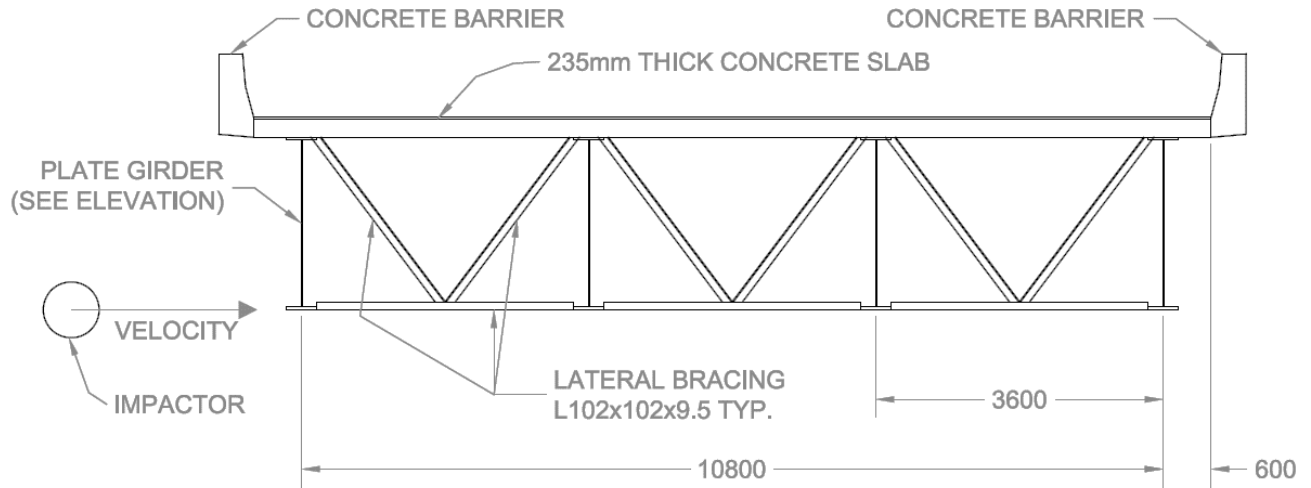


**Figure 5-2: Cross-section of bridge.**

The lateral bracing shown in Figure 5-2 consisted of L102x102x9.5 angles connected to 14 mm thick vertical web stiffeners, which are not shown in the cross-section. The impactor was 762 mm wide and had a 300 mm radius. The impactor dimensions were similar to a backhoe shovel. The impactor movement was limited to the direction shown in Figure 5-2. The modelled bridge was subjected to a 60 km/h impact with a 1000 kg impactor at the midpoint of the first span. The plate dimensions in the top flanges, bottom flanges, and webs along the length are shown in Figure 5-3. The bridge elevation in Figure 5-3 also shows the locations of lateral bracing and support conditions modelled.

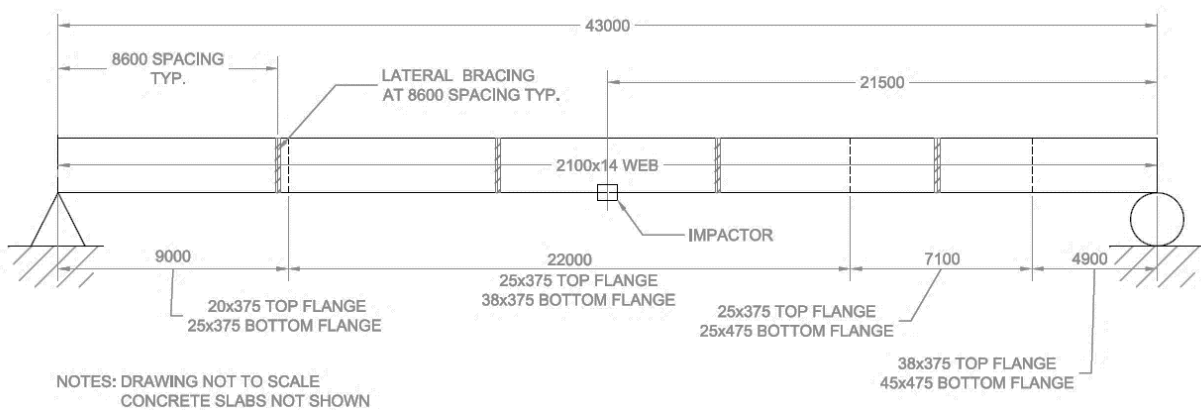


**Figure 5-3: Bridge elevation (dimensions in millimetres).**

Figure 5-3 shows that the web depth and thickness was constant at 2100 mm and 14 mm, respectively, whereas the top and bottom flange dimensions varied along the length. Lateral

bracing connected the girders every 8.6 metres as shown in Figure 5-3. The sections of the plate girders 4.3 m beyond the point of impact were modelled with 4-node reduced integration shell elements (S4R), as shown in Figure 5-4. The web stiffeners and lateral bracing members were also modelled as S4R elements. The elements modelling the plate girders, lateral bracing members, and web stiffeners were connected using surface and edge tie constraints pairing the displacements of nodes. Tie constraints were used to facilitate changes in mesh geometry and transitions between bridge components modelled with solid and shell elements. The steel bridge components were modelled using the material properties discussed in Sections 3.1 and 4.2.

The scope of this model was limited to heat straightening the impact damage on the fascia girder. The extent of the bridge model was reduced to sections with significant deformation, i.e. the fascia girder, web stiffeners, and lateral bracing. Figure 5-4 shows the deformed shape of the bridge, longitudinal plastic strains, and residual stresses on the bottom flange after springback.

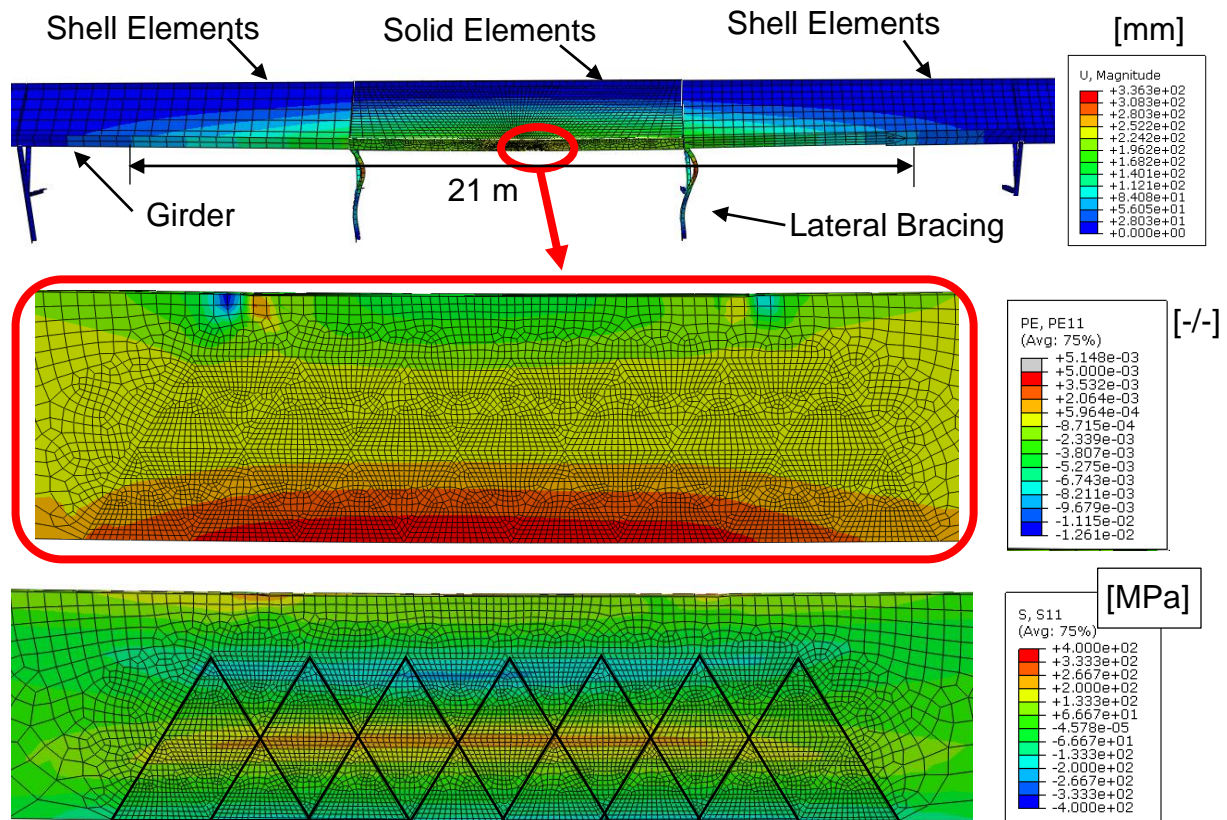
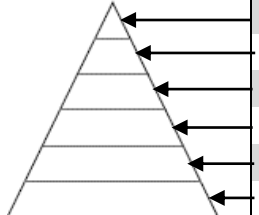


**Figure 5-4: Deformations on plate girder and longitudinal plastic strains and longitudinal stress on the bottom flange after impact.**

The seven overlapping heat patterns, shown in Figure 5-4, were divided into six sequentially heated regions with the forced convection coefficients as shown in Table 5-1.

**Table 5-1: Forced convection coefficients for bottom flange Vee heat pattern.**



Region Number	Convection Coefficient [mW/mm <sup>2</sup> K]
1	0.40
2	0.21
3	0.16
4	0.12
5	0.10
6	0.035

Each region of the bottom flange was heated from both sides where accessible. The heat transfer model assumed that it would require 4 minutes to heat each region. Prior to heating the next vee pattern, the steel was left to cool for 30 minutes using the cooling convection and radiation coefficients discussed in Section 4.2.1

### 5.2.2 Impact and Heat Straightening Results

The majority of the deformation occurred at the bottom flange of the fascia girder, the web stiffeners, and the two lateral bracing members closest to the point of impact as shown in Figure 5-4. The bottom flange laterally deformed 235 mm at the point of impact, the lateral deformation extended approximately 21 m along the beam. The largest longitudinal plastic strains were located in the contact area of the impactor. These large local plastic strains are caused by the impact and may result in cracking. The local damage was not repaired in this heat straightening model. This model focused on straightening deformation over the entire beam. The longitudinal plastic strains from bending at the opposite edge of the bottom flange were closer to 0.005. The largest longitudinal stresses from bending in the bottom flange were approximately -212 MPa and 230 MPa located near the web.

The heat straightening process was simplified by removing smaller plastically deformed bridge components. The plastically deformed web stiffeners and lateral bracing members were identified and removed. The removal of members caused the deformed bottom flange to

rebound. The rebounded bottom flange was now laterally deformed only 53 mm and lateral deformations extended 15 m along the beam, as shown in Figure 5-5.

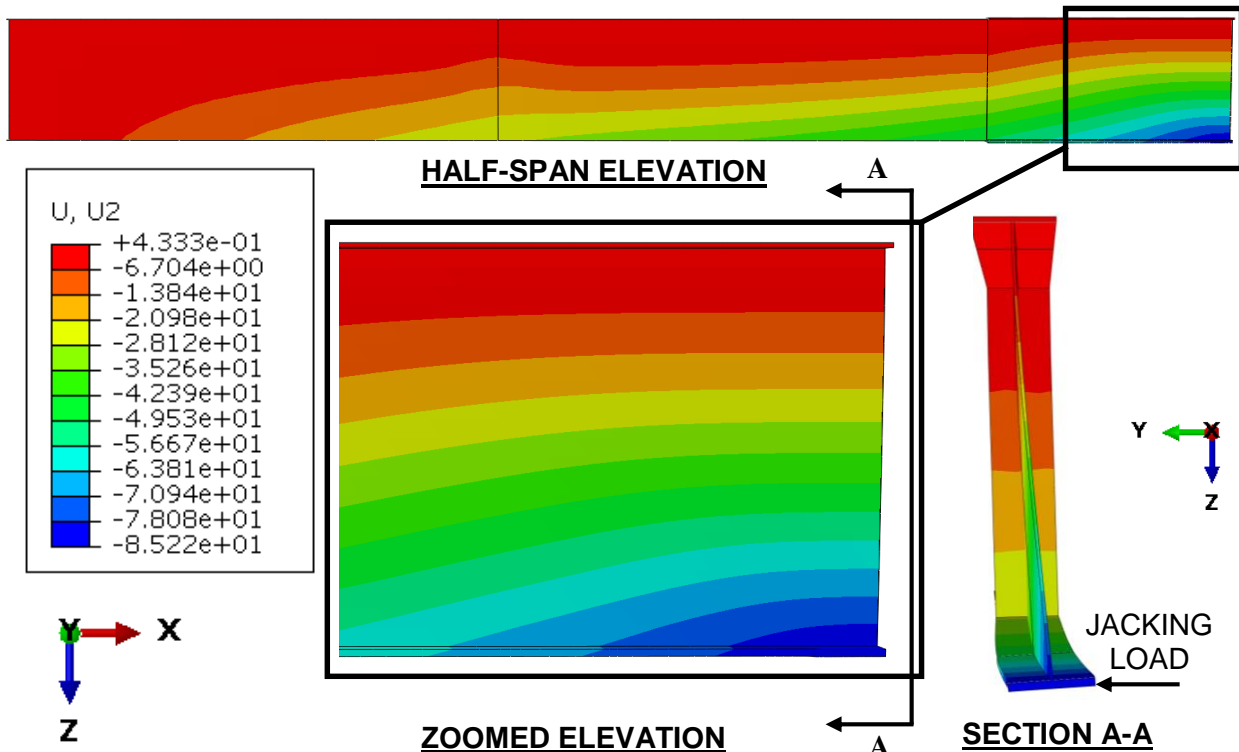


**Figure 5-5: Deformations after removal of selected stiffeners and lateral bracing members.**

The remaining deformations in the bottom flange were remediated by heating seven overlapping heat patterns spread over the extent of the longitudinal plastic strained region as highlighted in Figure 5-4. The heat patterns were heated from both sides to ensure heat penetration through the 38 mm thick bottom flange. The heat patterns were heated sequentially starting with the middle vee and progressed outwards to adjacent patterns. The set of heat patterns shown in Figure 5-4 were heated multiple times with the jacking loads.

Jacking loads were applied on the bottom flange at the midspan (middle vee heating pattern), as shown in Figure 5-5. Often the load caused the bottom flange to curve past its undeformed shape. The jacking loads were also increased every seven heat cycles when the midspan vee patterns were heated. A 24.9 kN jacking load was added at Heat Cycle 8. The jacking load was increased to 49.1 kN, 73.6 kN, and 85.9 kN at Heat Cycles 15, 22, 29, respectively. Progressively increasing jacking loads prevented mechanical straightening;

mechanical straightening could be observed through a loading-unloading cycle. An 85.9 kN jacking load causes 50 % jacking ratio without consideration for residual stresses from impact. The applied jacking loads deformed the bottom flange up to 230 mm past its undeformed shape; the deformation caused by the jacking loads were elastic.

Vee heat straightening without any jacking loads reduced the displacement by 1-2 mm every cycle. The addition of jacking loads increased the change in displacement up to 4 mm. Figure 5-6 shows the lateral displacement of the bottom flange after each heating cycle.

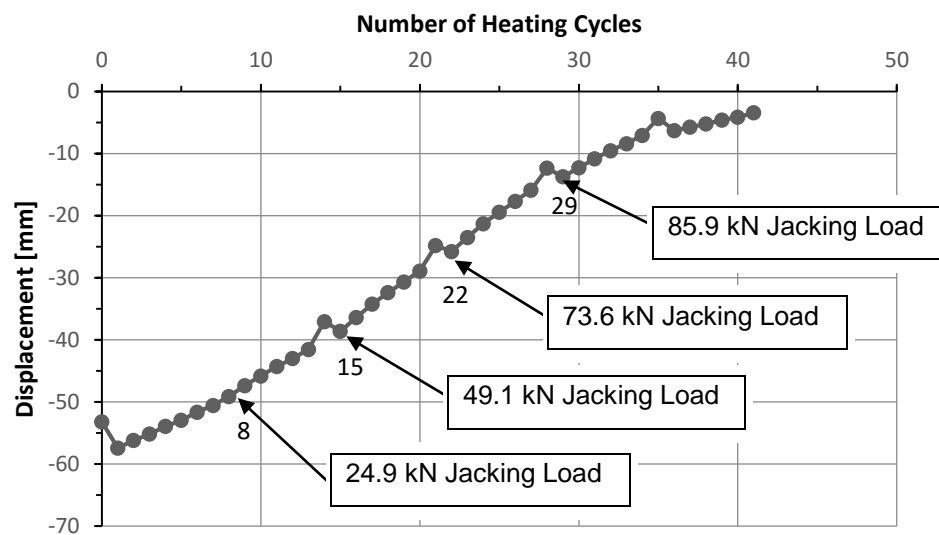


**Figure 5-6: Lateral displacement after each vee heating and cooling cycles.**

The lateral displacement was measured at the midspan of the bottom flange at opposite of the impacted edge. The vee heating cycles located at the midspan increased the lateral displacement and reduced the residual stresses. The bridge girder required 42 heat cycles to complete the heat straightening of the bottom flange, the final lateral displacement of the bottom flange was 3.4 mm.

Figure 5-7 shows the longitudinal plastic strains and residual longitudinal stress distributions after heat straightening the plate girder. The residual stresses were significantly larger after heat straightening; the largest longitudinal stresses were 534 MPa located at the web-flange connection. The residual stresses increased from 200 MPa to 430 MPa. The longitudinal plastic strains created by the impact were reduced from 0.005 to 0.0035 by the heat straightening process. After the bottom flange was straightened, a 6.7 mm bulge in the web remained.

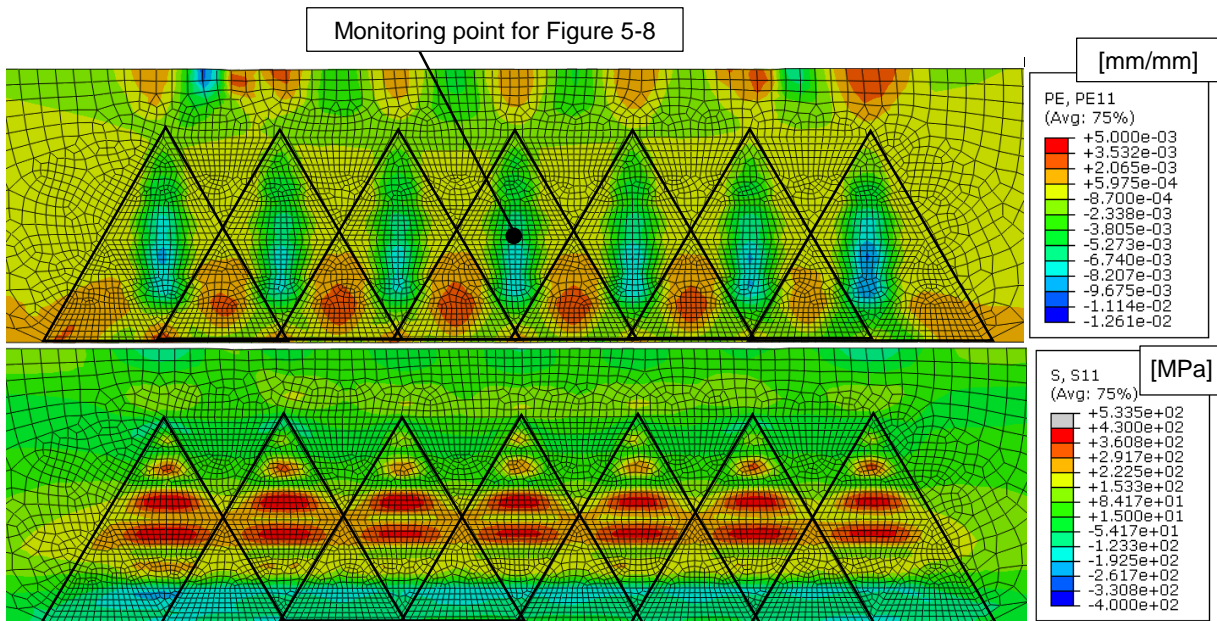


**Figure 5-7: Longitudinal plastic strains and residual longitudinal stress distributions on bottom flange of heat straightened girder.**

Web line heating was applied and the deformation in the web was reduced down to 2 mm. The changes in the web reduced the residual stress on the flange from 534 MPa to 460 MPa.

The longitudinal stresses and strains caused by the vee heat cycles were monitored at the middle vee pattern as shown in Figure 5-7. Figure 5-8 shows the longitudinal plastic strains versus stress during vee heat straightening from the middle vee pattern. Each heat set in Figure 5-8 refers to the set of seven vee patterns heated on the bottom flange of the girder. Longitudinal stress ranged from -400 MPa to 300 MPa during heat straightening. The large variations in stress shown in Figure 5-8 occur during heating and cooling of the vee pattern. Changes in longitudinal strains from heating became less effective as the repairs progressed. The changes in longitudinal strain were caused in two stages: while the latter half of the vee pattern was heated and while the entire vee pattern was cooled. Largest changes in strain occurred while the entire vee pattern cooled. Longitudinal strains were not significantly affected by adjacent overlapping heat patterns.

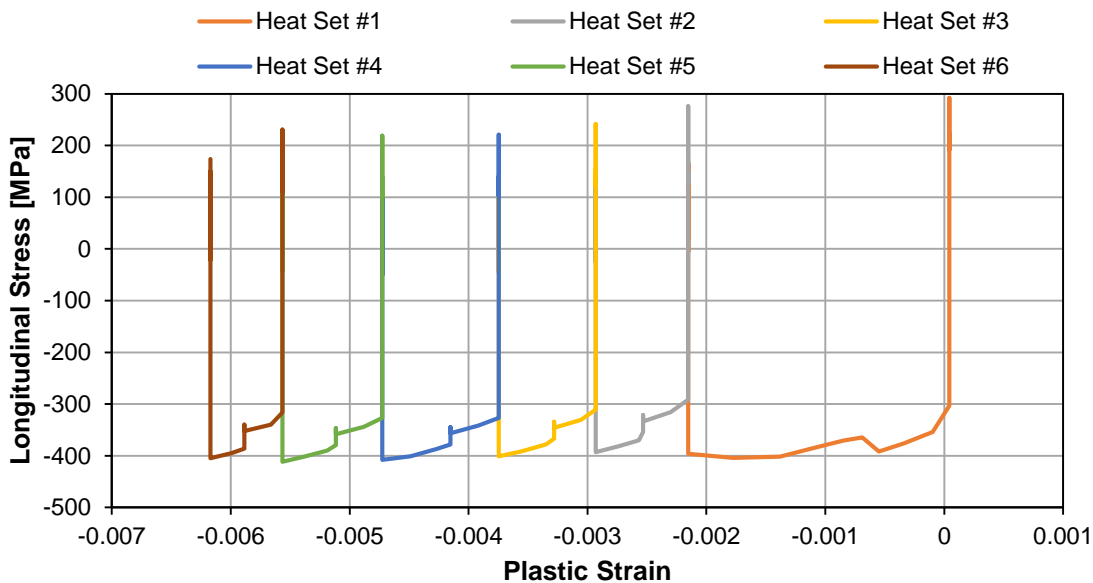


**Figure 5-8: Longitudinal plastic strains and longitudinal stress on bottom flange during heat straightening measured in the middle vee pattern.**

### 5.3 Impact and Heat Straightening Bridge Modelling Discussion

Modelling impact and heat straightening of a steel bridge with FEA is a complex undertaking, requiring thermal and mechanical parameters not defined in the Canadian highway bridge design code [Canadian Standards Association, 2006]. The proposed workflow defines the required information and the process for modelling impact and heat straightening. Implementing this workflow on a full-scale highway bridge structure has provided additional insights concerning the modelling of impact and heat straightening.

The iteration process for impact modelling was expedited by the separation of the impact and the springback analysis. The magnitude of impact damage and the type of deformation can be verified prior to springback. In addition, using a quasi-static springback analysis is significantly faster than a dynamic one.

The heat straightening process was separated into heat transfer and quasi-static analyses. Thus, instead of performing 42 heat transfer analyses, only one heat transfer analysis was required per heat pattern. The 7 temperature-distributions were imported into the quasi-static

analyses to achieve 42 heat cycles. A simultaneous thermal-stress analysis would be subjected to repetitive and redundant temperature calculations.

While it is not a required component of the workflow, selectively removing smaller deformed steel members and gradually increasing jacking forces had a large effect on heat straightening. In the model, the stiffeners did not appear significantly deformed from the impact. The stiffeners were selected for removal based on the plastic strain identified after the impact analysis. Current practice is to remove or disconnect smaller steel members, which may inhibit plastic rotations during heat straightening. Selectively removing the lateral bracing and stiffeners allowed the lateral deformation of the bottom flange to spring back from 235 mm to 53 mm. Gradually increasing jacking loads is used as a precaution to prevent mechanical straightening. The residual stresses in the bottom flange were redistributed towards the web as the beam straightened. The additional jacking loads are used to compensate for the change in residual stresses to maintain constant changes in geometry from heat straightening.

## 6 Conclusions

Heat straightening is an alternative method of bridge impact damage repair that requires an understanding of thermo-mechanical behaviour to model numerically. It is important to model the impact before heat straightening rather than importing the deformed shape into the heat straightening FEA. Heat straightening is dependent on the residual stresses from impact, which must also be modelled. In this thesis, the differences in residual stress and strain were explored between modelling impact with quasi-static and dynamic loading. The developed workflow and methods of modelling heat straightening with FEA were used to estimate displacement and assess the residual stresses from heat straightening.

The process of modelling impact and heat straightening requires numerous parameters describing the thermal and mechanical response of steel. These parameters are not always readily available. The following simplifications were used to facilitate the modelling process:

- Missing steel parameters were substituted with typical properties for mild structural steel.
- The vee heating process was simplified by using sequentially heated regions.

Plastic rotations from heat straightening of plates were similar between FEA models with these simplifications and existing experimental data.

While it is not always necessary to use FEA to assess damage from impact or to model heat straightening to plan repairs, the information from FEA models can be used to provide insight into repairs. Modelling of damaged bridges can be used to assist in the assessment of fatigue life in a bridge. As shown in Section 5.2.2, the removal of plastically deformed steel stiffeners identified in the FEA model significantly reduced deformations from impact.

The conclusions presented in this chapter are divided into three sections, which discuss conclusions related to: (i) impact modelling, (ii) heat straightening or camber modelling, and (iii) workflow and implementation of heat straightening on full-scale bridge models.

### 6.1 Impact Modelling

Impact modelling for bridges is often performed with quasi-static displacement control. Impacts modelled using dynamic loading provide significantly different results. The following conclusions were developed based on the two-dimensional impact models in Chapter 3:

- Modelling impact using quasi-static loading can be used to approximate the correct deformed geometry but does not account for the strain-rate sensitive properties of steel.
- Dynamic impact modelling requires the knowledge of additional parameters describing the strain-rate effects on the material properties of steel. The Cowper-Symonds relationship can be used to describe the yield strength of steel relative to strain-rate. The dynamic yield strength is up to 1.4 times the quasi-static yield strength of steel during impact.
- Introducing the impact load dynamically results in lower residual stresses compared to quasi-static loading. Residual stresses are related to the impact velocity; higher speed impacts result in lower residual stresses.
- Despite differences in residual stresses between methods of modelling impact, the strains are similar and only differ at points of impact or locations having sharp changes in geometry (such as weld toes), where the strain rates are largest.

## 6.2 Heat Straightening Modelling

Modelling heat straightening in FEA is similar to the process used to model flame cambering. The governing mechanism in both models requires thermal expansion and reduced yield strength at elevated temperatures to create local deformations. The following conclusions were developed from investigating models of heat cambered plates:

- Heat straightening is a thermo-mechanical process and finite element models of heat straightening require either a simultaneous coupled thermo-mechanical or a sequential coupled thermo-mechanical analysis.
- The sequential coupled thermal-mechanical analyses are significantly faster to execute than simultaneous coupled thermo-mechanical analysis. However, instead of a single analysis, modelling of heat straightening requires two separate analyses: heat transfer and quasi-static analysis. Time steps must be sufficiently small to cover changes in temperature from the motion of the torch.
- The heat flux distribution of an oxyacetylene torch is often modelled in flame cambering and heat straightening using a Gaussian distribution of a nodal heat flux. The meandering

motion of a torch associated with heating vee patterns can be simplified by modelling the heating pattern in regions using a forced heat convection model.

- Due to the gradual changes in geometry that result from heat straightening, the mechanical part of the FEA of heat straightening can be modelled as a quasi-static process.
- Boundary conditions are important in modelling when multiple cycles of heat straightening are involved. Excessively restrained plates will not effectively deform from heat straightening.

### **6.3 Implementing Impact and Heat Straightening Methods in Full-Scale Models**

Modelling impact and heat straightening on full-scale bridges requires significantly longer computation times. The development of the bridge model itself requires significantly increased complexity. The following conclusions identify valid modelling techniques to facilitate mesh creation and mitigating longer computations:

- Sections of the steel girder subjected to heat straightening should be modelled with solid elements. Steel not subjected to heat straightening can be modelled with shell or beam elements.
- Sections of steel subjected to heat straightening should incorporate the mesh of the heating patterns to facilitate the application of heat in the model.
- Although not a requirement of the modelling process, complex mesh geometry due to abrupt mesh or element changes can be created by using tie constraints for transitions.
- In cases where the deformed geometry from impact is limited to the steel portion (e.g. bottom flange and web) the stresses from impact on the concrete slab can be insignificant. Computation time can be reduced by replacing the elements representing the concrete slab with shell elements or simplified boundary conditions.
- Stiffeners and lateral bracing members adjacent to the point of impact are important for developing the final deformed shape and spreading the loads to neighbouring girders. In cases where impact loads originate from the bottom flange of the girder, vertical web stiffeners and lateral bracing members may be subjected to forces sufficient to cause yielding.

## 7 Recommendations

This chapter presents recommendations for future research and suggestions for industry concerning heat straightening. These recommendations are based on previous research in the literature review and insights from the FEA analyses performed for the current study.

### 7.1 Recommendations for Future Research

The following recommendations for future research are based on gaps in existing research discovered while developing FEA models for heat straightening:

- Canadian steel grades should be tested for changes in material properties at different magnitudes of strain based on quasi-static and dynamic loading. This includes the fracture properties at various temperatures after heat straightening.
- Future investigations on changes in material properties with respect to different magnitudes of strain should incorporate higher strain rate loading.
- Thermal softening and strain rate (Cowper-Symonds) parameters of Canadian steels should be measured to see if they are different from the values typically assumed for mild steel.
- Thermal properties such as emissivity and the convection coefficients for plates with several different finishes and ages commonly presented in bridges should be identified. Convection coefficients should also vary based on wind speed.
- Efforts should be taken to model heat straightening in colder ambient temperatures, to determine if there are temperature restrictions or modified procedures that should be followed.

### 7.2 Recommendations for Industry

The following recommendations for industry are based on insights from results for modelling impact and heat straightening:

- Modelling impact using quasi-static load results in conservative estimation of residual stress. Lower residual stresses can be obtained by modelling impact with dynamic loading.
- Using equivalent jacking ratios for different steel grades, does not result in similar plastic rotations.
- Using multiple adjacent heating patterns is preferable over the use of multiple cycles of heating for a single pattern in terms of the rate of straightening achieved.
- Modelling impact is effective for determining where plastic deformation occurs. Significant reductions in deformation can occur from the removal of damaged stiffeners or lateral bracing members. This may be worth considering, if the effect of member removal on the structural performance of the bridge under service loading is tolerable.
- The removal of smaller yielded bridge steel members such as stiffeners and lateral bracing members may cause significant springback. The resulting deformed shape after springback may require fewer heating cycles to straighten.

## References

- Alberta Transportation, 2004. *Repair of Bridge Structural Steel Elements Manual*, s.l.: Government of the province of Alberta.
- Arasaratnam, P., Sivakumaran, K. S. & Tait, M. J., 2011. True Stress-True Strain Models for Structural Steel Elements. *International Scholarly Research Network*.
- Avent, R. R., Mukai, D. J., Robinson, P. F. & Boudreux, R. J., 2000. Heat Straightening Damaged Steel Plate Elements. *Journal of Structural Engineering*, pp. 747-754.
- Avent, R. R. & Mukai, J. D., 2001. Engineering Heat-Straightening Repairs: A Case Study. *Journal of Bridge Engineering*, Issue April, pp. 95-102.
- Belytschko, T., Liu, W. K. & Moran, B., 2000. *Nonlinear Finite Elements for Continua and Structures*. s.l.:John Wiley & Sons Ltd..
- Brokenbrough, R. L. & Johnson, B. G., 1994. *Structural Alloys Handbook*. s.l.:s.n.
- Canadian Institution of Steel Construction, 2011. Straight Girder Design Example. In: *Steel Bridges: Design - Fabrication - Construction*. s.l.:s.n.
- Canadian Standards Association, 2006. *CAN/CSA-S6-06 Canadian Highway Bridge Design Code*. s.l.:s.n.
- Clubley, S. K., Winter, S. N. & Turner, K. W., 2006. Heat-straightening repairs to a steel road bridge. *Bridge Engineering*, Issue BEI, pp. 35-42.
- Connor, R. J., Urban, M. J. & Kaufmann, E. J., 2008. *Heat-Straightening Repair of Damaged Steel Bridge Girders: Fatigue and Fracture Performance*, Washington DC: Transportation Research Board.
- Dassault Systèmes, 2011. *Abaqus Theory Manual v6.11*. Providence, RI: Dassault Systèmes.
- European Committee for Standardisation, 2005. *EN 1993-1-2: Eurocode 3: Design of steel structures: Part 1-2: General Rules - Structural fire design*. s.l.:CEN.
- Fire and Blast Information Group, 2001. *Design Guide for Steels at Elevated Temperatures and High Strain Rates*. Ascot: The Steel Construction Institute.

- Holman, J., 2002. *Heat Transfer*. 9th ed. s.l.:McGraw-Hill.
- Kobayashi, S., Oh, S.-I. & Altan, T., 1989. *Metal forming and the finite-element method*. s.l.:Oxford University Press.
- Kowalkowski, K. J., 2005. *Effects of Multiple Damage - Heat Straightening Repair Cycles on the Structural Properties and Serviceability of Steel Beam Bridges*, s.l.: Perdue University.
- Lacalle, R. et al., 2013. Flame straightening application on structural steels: Effects on mechanical and fracture properties. *Research and Applications in Structural Engineering, Mechanics and Computation*, pp. 406-410.
- Linde Gas, 2014. *Lindoflamm Special Torches for Acetylene Processes*, s.l.: s.n.
- Liu, K., 2006. *Fracture Properties of Heat-Straightened Steel*, s.l.: University of Wyoming.
- Ministry of Transportation of Ontario, 2012. Heat Straightening of Lees Avenue Underpass Girder. *RoadTalk*, Issue Spring 2012.
- Moshaiov, A. & Latorre, R., 1985. Temperature Distribution During Plate Bending By Torch Flame Heating. *Journal of Ship Research*, 29[1], pp. 1-11.
- Moshalov, A. & Vorus, W. S., 1987. The Mechanics of the Flame Bendin Process: Theory and Applications. *Journal of Ship Research*, pp. 269-281.
- Mukai, D. J. & Avent, R. R., 1998. *Heat Straightening Repairs of Damaged Steel Bridges: A Technical Guide and Manual of Practice*, s.l.: Federal Highway Administration.
- Nicholls, J. I. & Weerth, D. E., 1972. Investigation of Triangular Heats applied to mild steel plates. *AISC Engineering Journal*, pp. 137-141.
- Roeder, C. W., 1986. Experimental Study of Heat Induced Defomation. *Journal of Structural Engineering*, October, 112[10], pp. 2247-2262.
- Sadiq, H. et al., 2013. Determination of Steel Emissivity for the Temperature Prediction of Structural Steel Members in Fire. *Journal of Materials in Civil Engineering*, pp. 167-173.
- Sharma, M., 2005. *Behavior of heat straightened plates bent along the minor axis*, Baton Rouge: s.n.

Transportation Research Board, 1984. *Guidelines for Evaluation and Repair of Damaged Steel Bridge Members*, s.l.: Transportation Research Board.

## **Appendix A: News search from July 2014 to March 2015**

**Table A1: Table of news stories with collisions involving over-height vehicles with bridges.**

Date	#	Location	Headline	URL
15/07/2014	1	US	PERRIS: Sand hauler hits I-215 bridge; falsework collapses	<a href="http://www.pe.com/articles/-747679--.html">http://www.pe.com/articles/-747679--.html</a>
21/07/2014	2	US	Main Street closed after truck collides with Dexter railroad bridge	<a href="http://www.mlive.com/news/ann-arbor/index.ssf/2014/07/dexters_main_street_closed_aft.html">http://www.mlive.com/news/ann-arbor/index.ssf/2014/07/dexters_main_street_closed_aft.html</a>
31/07/2014	3	ZA	South African giraffe dies after 'hitting bridge'	<a href="http://www.bbc.com/news/world-africa-28586702">http://www.bbc.com/news/world-africa-28586702</a>
05/08/2014	4	US	Truck Hits Railroad Bridge on UVa. Corner	<a href="http://www.newsplex.com/home/headlines/Truck-Hits-Railroad-Bridge-on-UVa-Corner-269994451.html">http://www.newsplex.com/home/headlines/Truck-Hits-Railroad-Bridge-on-UVa-Corner-269994451.html</a>
05/08/2014	5	US	Truck hits bridge in Woonsocket	<a href="http://www.wnct.com/story/26198948/truck-hits-bridge-in-woonsocket">http://www.wnct.com/story/26198948/truck-hits-bridge-in-woonsocket</a>
07/08/2014	6	US	Bainbridge Blvd. reopens after tractor-trailer hit overpass	<a href="http://wavy.com/2014/08/06/pd-driver-injured-when-tractor-trailer-hits-overpass/">http://wavy.com/2014/08/06/pd-driver-injured-when-tractor-trailer-hits-overpass/</a>
14/08/2014	7	US	Replacement of bridge hit by truck to impact traffic on I-78	<a href="http://www.wfmz.com/news/news-regional-berks/replacement-of-bridge-hit-by-truck-to-impact-traffic-on-interstate-78-in-bethel">http://www.wfmz.com/news/news-regional-berks/replacement-of-bridge-hit-by-truck-to-impact-traffic-on-interstate-78-in-bethel</a>
17/08/2014	8	US	1 Killed in Tanker Truck Fire on I-65 in Tennessee	<a href="http://abcnews.go.com/US/wireStory/killed-tenn-tanker-truck-fire-65-closed-24993546">http://abcnews.go.com/US/wireStory/killed-tenn-tanker-truck-fire-65-closed-24993546</a>
19/08/2014	9	US	Cambridge St. business seek relief from truck-eating low bridge	<a href="http://www.telegram.com/article/20140822/NEWS/308229698/">http://www.telegram.com/article/20140822/NEWS/308229698/</a>
22/08/2014	10	UK	M180 closed after lorry carrying forklift truck "hits bridge"	<a href="http://www.scunthorpetelegraph.co.uk/M180-closed-lorry-carrying-forklift-truck-hits/story-22783042-detail/story.html">http://www.scunthorpetelegraph.co.uk/M180-closed-lorry-carrying-forklift-truck-hits/story-22783042-detail/story.html</a>
27/08/2014	11	US	Turnpike bridge takes hit	<a href="http://www.thegatewaynews.com/news%2520local/2014/08/27/turnpike-bridge-takes-hit">http://www.thegatewaynews.com/news%2520local/2014/08/27/turnpike-bridge-takes-hit</a>
28/08/2014	12	US	Truck strikes Chewton bridge	<a href="http://www.ellwoodcityledger.com/news/police_fire_courts/truck-strikes-chewton-bridge/article_431d574a-5c75-5d97-a042-0dd557eeefca8.html">http://www.ellwoodcityledger.com/news/police_fire_courts/truck-strikes-chewton-bridge/article_431d574a-5c75-5d97-a042-0dd557eeefca8.html</a>
28/08/2014	13	US	Truck stuck under Washington Street bridge in Norwalk	<a href="http://www.thehour.com/news/norwalk/truck-stuck-under-washington-street-bridge-in-norwalk/article_93b76628-2ed0-11e4-96ac-001a4bcf6878.html">http://www.thehour.com/news/norwalk/truck-stuck-under-washington-street-bridge-in-norwalk/article_93b76628-2ed0-11e4-96ac-001a4bcf6878.html</a>
05/09/2014	14	US	Tractor-trailer carrying cars hits train trestle in Apex	<a href="http://www.wral.com/tractor-trailer-carrying-cars-hits-train-trestle-in-apex/13946217/">http://www.wral.com/tractor-trailer-carrying-cars-hits-train-trestle-in-apex/13946217/</a>
06/09/2014	15	US	Hutchinson Parkway reopened; Army truck hit bridge	<a href="http://www.lohud.com/story/news/local/westchester/2014/09/04/truck-crash-closes-hutchinson-parkway-mount-vernon/15076829/">http://www.lohud.com/story/news/local/westchester/2014/09/04/truck-crash-closes-hutchinson-parkway-mount-vernon/15076829/</a>
06/09/2014	16	US	Scrap metal hauler loses some cargo after hitting I-40 bridge	<a href="http://www.wbir.com/story/news/local/2014/09/04/scrap-metal-hauler-loses-some-cargo-after-hitting-i-40-bridge/15062915/">http://www.wbir.com/story/news/local/2014/09/04/scrap-metal-hauler-loses-some-cargo-after-hitting-i-40-bridge/15062915/</a>
07/09/2014	17	US	Truck gets stuck under overpass on Rock Creek Pkwy	<a href="http://www.wusa9.com/story/traffic/2014/09/05/traffic-accidents-crashes-delays-updates-friday-dc-md-va/15117729/">http://www.wusa9.com/story/traffic/2014/09/05/traffic-accidents-crashes-delays-updates-friday-dc-md-va/15117729/</a>
08/09/2014	18	IS	Latest truck accident leaves one injured	<a href="https://www.todayszaman.com/national_latest-truck-accident-leaves-one-injured_358018.html">https://www.todayszaman.com/national_latest-truck-accident-leaves-one-injured_358018.html</a>
09/09/2014	19	US	SMU walk bridge hit by semi; students will walk across Hwy. 14	<a href="http://www.winonadailynews.com/news/local/smu-walk-bridge-hit-by-semi-students-will-walk-across/article_12458288-8e1d-5008-8b35-8d89d3f803d7.html">http://www.winonadailynews.com/news/local/smu-walk-bridge-hit-by-semi-students-will-walk-across/article_12458288-8e1d-5008-8b35-8d89d3f803d7.html</a>
10/09/2014	20	US	Interstate 35 closed five hours after bridge overpass hit	<a href="http://www.kcci.com/news/interstate-35-southbound-closed-due-to-crash/27953846">http://www.kcci.com/news/interstate-35-southbound-closed-due-to-crash/27953846</a>
15/09/2014	21	US	Driver Ticketed After Truck Hits Overpass	<a href="http://easthamptonstar.com/News/2014915/Driver-Ticketed-After-Truck-Hits-Overpass">http://easthamptonstar.com/News/2014915/Driver-Ticketed-After-Truck-Hits-Overpass</a>
17/09/2014	22	US	Box truck strikes bridge on East Avenue	<a href="http://www.thehour.com/box-truck-strikes-bridge-on-east-avenue/article_0afac99e-3e78-11e4-af17-001a4bcf6878.html">http://www.thehour.com/box-truck-strikes-bridge-on-east-avenue/article_0afac99e-3e78-11e4-af17-001a4bcf6878.html</a>

**Table A2: Table of news stories with collisions involving over-height vehicles with bridges (cont).**

Date	#	Location	Headline	URL
24/09/2014	24	US	Bridgeport man killed in dump truck crash on I-91 in New Haven	<a href="http://www.nhregister.com/general-news/20140923/bridgeport-man-killed-in-dump-truck-crash-on-i-91-in-new-haven">http://www.nhregister.com/general-news/20140923/bridgeport-man-killed-in-dump-truck-crash-on-i-91-in-new-haven</a>
26/09/2014	25	US	Pedestrian bridge falls onto Southfield Freeway after hit by truck; driver killed	<a href="http://www.clickondetroit.com/news/pedestrian-bridge-collapses-on-m39-closes-freeway/28259654">http://www.clickondetroit.com/news/pedestrian-bridge-collapses-on-m39-closes-freeway/28259654</a>
30/09/2014	26	US	Bridge struck by garbage truck collapses	<a href="http://www.purchasingb2b.ca/3-fleet/bridge-struck-garbage-truck-collapses-detroit-freeway-137184/">http://www.purchasingb2b.ca/3-fleet/bridge-struck-garbage-truck-collapses-detroit-freeway-137184/</a>
30/09/2014	27	US	Truck strikes bridge in South Norwalk (again), stalled Transit bus on 95 delays response	<a href="http://www.thehour.com/news/norwalk/truck-strikes-bridge-in-south-norwalk-again-stalled-transit-bus/article_e8fff1a3-ffc1-5cc1-a596-b84aae8469cc.html">http://www.thehour.com/news/norwalk/truck-strikes-bridge-in-south-norwalk-again-stalled-transit-bus/article_e8fff1a3-ffc1-5cc1-a596-b84aae8469cc.html</a>
01/10/2014	28	US	Truck gets stuck under Storrow Drive pedestrian bridge	<a href="http://www.bostonglobe.com/metro/2014/09/30/truck-gets-wedged-under-storrow-drive-pedestrian-bridge/Pw0E9mfG1iVbo0oPxHJEKP/story.html">http://www.bostonglobe.com/metro/2014/09/30/truck-gets-wedged-under-storrow-drive-pedestrian-bridge/Pw0E9mfG1iVbo0oPxHJEKP/story.html</a>
03/10/2014	29	CAN	Update: Boom truck hits rail bridge in downtown Winnipeg	<a href="http://metronews.ca/news/winnipeg/1172433/boom-truck-hits-rail-bridge-in-downtown-winnipeg/">http://metronews.ca/news/winnipeg/1172433/boom-truck-hits-rail-bridge-in-downtown-winnipeg/</a>
04/10/2014	30	US	Everett bridge inspected, to reopen after truck hits it	<a href="http://blogs.seattletimes.com/today/2014/10/truck-strike-forces-closure-of-everett-bridge/">http://blogs.seattletimes.com/today/2014/10/truck-strike-forces-closure-of-everett-bridge/</a>
15/10/2014	31	US	Oil field truck loses load on I-10 near downtown Houston	<a href="http://www.chron.com/news/houston-traffic/article/Oil-field-truck-loses-load-on-I-10-near-downtown-5822284.php">http://www.chron.com/news/houston-traffic/article/Oil-field-truck-loses-load-on-I-10-near-downtown-5822284.php</a>
16/10/2014	32	US	Yet another truck has fallen victim to the Seventh Street bridge	<a href="http://www.southernminn.com/faribault_daily_news/article_6620464f-e408-5d1b-8b60-3cb256f7a77d.html">http://www.southernminn.com/faribault_daily_news/article_6620464f-e408-5d1b-8b60-3cb256f7a77d.html</a>
19/10/2014	33	CAN	Truck hits train overpass on Dalhousie Street	<a href="http://www.trurodaily.com/News/Local/2014-10-18/article-3907697/Truck-hits-train-overpass-on-Dalhousie-Street/1">http://www.trurodaily.com/News/Local/2014-10-18/article-3907697/Truck-hits-train-overpass-on-Dalhousie-Street/1</a>
23/10/2014	34	US	Police: Truck hits overpass on Southern State Parkway	<a href="http://www.newsday.com/long-island/suffolk/police-truck-hits-overpass-on-southern-state-parkway-1.9532430">http://www.newsday.com/long-island/suffolk/police-truck-hits-overpass-on-southern-state-parkway-1.9532430</a>
30/10/2014	35	US	Merritt Closed In Greenwich After Truck Slams Into Bridge, Catches Fire	<a href="http://harrison.dailyvoice.com/news/merritt-closed-greenwich-after-truck-slams-bridge-catches-fire">http://harrison.dailyvoice.com/news/merritt-closed-greenwich-after-truck-slams-bridge-catches-fire</a>
14/11/2014	36	US	Officials: Dump truck strikes bridge above I-35	<a href="http://www.washingtontimes.com/news/2014/nov/13/officials-dump-truck-strikes-bridge-above-i-35/">http://www.washingtontimes.com/news/2014/nov/13/officials-dump-truck-strikes-bridge-above-i-35/</a>
27/11/2014	37	US	Over-height truck strikes I-90 overpass east of Snoqualmie Pass	<a href="http://www.komonews.com/news/local/Over-height-truck-strikes-I-90-overpass-east-of-Snoqualmie-Pass-283907761.html">http://www.komonews.com/news/local/Over-height-truck-strikes-I-90-overpass-east-of-Snoqualmie-Pass-283907761.html</a>
27/11/2014	38	US	Dale Mabry reopens after truck hits I-275 overpass	<a href="http://tbo.com/news/traffic/dale-mabry-traffic-slowed-as-truck-hits-i-275-overpass-20141126/">http://tbo.com/news/traffic/dale-mabry-traffic-slowed-as-truck-hits-i-275-overpass-20141126/</a>
04/12/2014	39	US	LIRR: Oyster Bay service delayed after vehicle strikes bridge	<a href="http://www.newsday.com/long-island/lirr-oyster-bay-service-delayed-after-vehicle-strikes-bridge-1.9676174">http://www.newsday.com/long-island/lirr-oyster-bay-service-delayed-after-vehicle-strikes-bridge-1.9676174</a>
06/12/2014	40	US	Worcester council puts brakes on plan to slap big fine on bridge-hitting truckers	<a href="http://www.telegram.com/article/20141203/NEWS/312039697%26Template%3Dprintart">http://www.telegram.com/article/20141203/NEWS/312039697%26Template%3Dprintart</a>
07/12/2014	41	US	TxDOT Moves To Fast-Track Highway 183 Bridge Repairs	<a href="http://dfw.cbslocal.com/2014/12/05/txdot-moves-to-fast-track-highway-183-bridge-repairs/">http://dfw.cbslocal.com/2014/12/05/txdot-moves-to-fast-track-highway-183-bridge-repairs/</a>
18/12/2014	42	US	Parkway bridge hit by truck to be inspected again Wednesday	<a href="http://www.pressofatlanticcity.com/news/breaking/parkway-bridge-hit-by-truck-to-be-inspected-again-wednesday/article_86a4d678-8551-11e4-9c14-8b9ec1781292.html">http://www.pressofatlanticcity.com/news/breaking/parkway-bridge-hit-by-truck-to-be-inspected-again-wednesday/article_86a4d678-8551-11e4-9c14-8b9ec1781292.html</a>
18/12/2014	43	CAN	Truck hit bridge east of Toronto, spills diesel across highway and into creek	<a href="http://www.kelownadailycourier.ca/news/national_news/article_f3cd024c-7934-5adb-bbf1-2518c4a6c735.html">http://www.kelownadailycourier.ca/news/national_news/article_f3cd024c-7934-5adb-bbf1-2518c4a6c735.html</a>
25/12/2014	44	US	Truck driver charged with driving away after hitting Augusta trestle	<a href="http://www.centralmaine.com/2014/12/23/truck-driver-charged-with-driving-away-after-hitting-augusta-trestle/">http://www.centralmaine.com/2014/12/23/truck-driver-charged-with-driving-away-after-hitting-augusta-trestle/</a>
01/01/2015	45	UK	THE M40 has reopened after a bridge was hit by a truck carrying a JCB.	<a href="http://www.oxfordmail.co.uk/news/11696148.UPDATE_Truck_carrying_JCB_crashes_into_bridge_on_M40_southbound/">http://www.oxfordmail.co.uk/news/11696148.UPDATE_Truck_carrying_JCB_crashes_into_bridge_on_M40_southbound/</a>

**Table A3: Table of news stories with collisions involving over-height vehicles with bridges (cont).**

Date	#	Location	Headline	URL
08/01/2015	46	NZ	Train services halted after truck, bridge collision	<a href="http://www.3news.co.nz/nznews/train-services-halted-after-truck-bridge-collision-2015010720">http://www.3news.co.nz/nznews/train-services-halted-after-truck-bridge-collision-2015010720</a>
21/01/2015	47	NZ	Oversized truck hits rail bridge	<a href="http://www.3news.co.nz/nznews/oversized-truck-hits-rail-bridge-2015012110">http://www.3news.co.nz/nznews/oversized-truck-hits-rail-bridge-2015012110</a>
22/01/2015	48	US	Troopers: Driver in noodle truck crash was fatigued	<a href="http://www.wral.com/troopers-driver-in-noodle-truck-crash-was-fatigued/14378092/">http://www.wral.com/troopers-driver-in-noodle-truck-crash-was-fatigued/14378092/</a>
01/02/2015	49	US	Truck Hits, Damages Bridge In Cherokee Co.	<a href="http://www.wspa.com/story/27991252/truck-hits-damages-bridge-in-cherokee-co">http://www.wspa.com/story/27991252/truck-hits-damages-bridge-in-cherokee-co</a>
04/02/2015	50	US	Springdale artery remains closed indefinitely	<a href="http://triblive.com/neighborhoods/yourallekiskivalley/yourallekiskivalleymore/7691312-74/springdale-road-bridge">http://triblive.com/neighborhoods/yourallekiskivalley/yourallekiskivalleymore/7691312-74/springdale-road-bridge</a>
05/02/2015	51	US	Bridge over I-85 closed after being hit by truck	<a href="http://www.gaffneyledger.com/news/2015-02-04/Local_News/Bridge_over_I85_closed_after_being_hit_by_truck.html">http://www.gaffneyledger.com/news/2015-02-04/Local_News/Bridge_over_I85_closed_after_being_hit_by_truck.html</a>
12/02/2015	52	CAN	Highway 132 reopened after footbridge collapse in Longueuil	<a href="http://montrealgazette.com/news/local-news/footbridge-over-highway-132-collapses-in-longueuil">http://montrealgazette.com/news/local-news/footbridge-over-highway-132-collapses-in-longueuil</a>
12/02/2015	53	CAN	Driver charged after big rig hits pedestrian bridge	<a href="http://www.newstalk770.com/2015/02/11/driver-charged-after-big-rig-hits-pedestrian-bridge/">http://www.newstalk770.com/2015/02/11/driver-charged-after-big-rig-hits-pedestrian-bridge/</a>
12/02/2015	54	UK	Truck stuck under railway bridge for THREE HOURS after dozy driver misjudged height of 12 ...	<a href="http://www.mirror.co.uk/news/uk-news/truck-stuck-under-railway-bridge-5144405">http://www.mirror.co.uk/news/uk-news/truck-stuck-under-railway-bridge-5144405</a>
16/02/2015	55	AU	Truck hits pedestrian bridge at Kangaroo Point	<a href="http://www.brisbanetimes.com.au/queensland/truck-hits-pedestrian-bridge-at-kangaroo-point-20150215-13flfq.html">http://www.brisbanetimes.com.au/queensland/truck-hits-pedestrian-bridge-at-kangaroo-point-20150215-13flfq.html</a>
20/02/2015	56	AU	Stuck trucks: Are Melbourne truckies height challenged?	<a href="http://www.theage.com.au/victoria/stuck-trucks-are-melbourne-truckies-height-challenged-20150219-13it9w.html">http://www.theage.com.au/victoria/stuck-trucks-are-melbourne-truckies-height-challenged-20150219-13it9w.html</a>
21/02/2015	57	US	Report: Prop helicopter hits bridge, blocks highway	<a href="http://www.palmbeachpost.com/news/news/report-prop-helicopter-hits-bridge-blocks-highway/nkF43/">http://www.palmbeachpost.com/news/news/report-prop-helicopter-hits-bridge-blocks-highway/nkF43/</a>
21/02/2015	58	US	Truck stuck under bridge in downtown Wichita	<a href="http://www.kwch.com/news/local-news/Truck-stuck-under-bridge-in-downtown-Wichita/31384094">http://www.kwch.com/news/local-news/Truck-stuck-under-bridge-in-downtown-Wichita/31384094</a>